INFORMATION TO USERS

This manuscript has been reproduced from the microfilm master. UMI films the text directly from the original or copy submitted. Thus, some thesis and dissertation copies are in typewriter face, while others may be from any type of computer printer.

The quality of this reproduction is dependent upon the quality of the copy submitted. Broken or indistinct print, colored or poor quality illustrations and photographs, print bleedthrough, substandard margins, and improper alignment can adversely affect reproduction.

In the unlikely event that the author did not send UMI a complete manuscript and there are missing pages, these will be noted. Also, if unauthorized copyright material had to be removed, a note will indicate the deletion.

Oversize materials (e.g., maps, drawings, charts) are reproduced by sectioning the original, beginning at the upper left-hand corner and continuing from left to right in equal sections with small overlaps. Each original is also photographed in one exposure and is included in reduced form at the back of the book.

Photographs included in the original manuscript have been reproduced xerographically in this copy. Higher quality 6" x 9" black and white photographic prints are available for any photographs or illustrations appearing in this copy for an additional charge. Contact UMI directly to order.

UMI

A Bell & Howell Information Company
300 North Zeeb Road, Ann Arbor MI 48106-1346 USA
313/761-4700 800/521-0600

Control and Design of Flexible–Link Manipulators

Mehrdad Moallem

A Thesis

in

The Department

of

Electrical and Computer Engineering

Presented in Partial Fulfillment of the Requirements

for the Degree of Doctor of Philosophy at

Concordia University

Montréal, Québec, Canada

December 1996

CONCORDIA UNIVERSITY

Division of Graduate Studies

This is to certify that the thesis prepared

By: **Mehrdad Moallem**

Entitled: **Control and Design of Flexible–link Manipulators**

and submitted in partial fulfilment of the requirements for the degree of

Doctor of Philosophy

complies with the regulations of this University and meets the accepted standards with respect to originality and quality.

Signed by the final examining committee:

_____ Prof. O. Schwelb

_____ Prof. D. Wang

_____ Prof. A. Al–Khalili

_____ Prof. G. Vatistas

_____ Prof. K. Khorasani

_____ Prof. R.V. Patel

Approved by _____

_____ 19 ____ _____

Dean of Faculty

ABSTRACT

Control and Design of Flexible–Link Manipulators

Mehrdad Moallem, Ph.D.

Concordia University, 1996

The control of non–minimum phase systems remains an important open problem in nonlinear control, finding relevance in the control of underactuated and flexible systems. One wishes to cause the output of a dynamical system to track a desired trajectory while maintaining internal stability of a nominally unstable system. In this regard, motion control of structurally flexible robotic manipulators has drawn the attention of robotics researchers in the past few years. These robots find applications in space, underwater, and high speed energy efficient manipulation.

This dissertation aims to address two important issues regarding flexible link manipulators: Control design, and structural shape design. In this regard, two control strategies are considered. The first one is based on the concept of integral manifolds in singular perturbation theory, and the second is based on input–output decoupling in nonlinear systems theory. The practical implementation issues for the former require the inconvenient measurement of flexural rates. An observation strategy is proposed to circumvent this problem. Experimental evaluation of the control strategies are carried out on a setup constructed in the laboratory.

Furthermore, structural shape optimization is considered as a means to improve the dynamic behavior. In this regard, an optimization index is introduced to achieve some desired features such as higher flexible mode natural frequencies and easier accessibility of flexible modes by the control inputs.

ACKNOWLEDGEMENTS

Many people have given me help, guidance, and inspiration in my years in graduate school. To all of them I am very grateful. First of all, I wish to thank my supervisors, Professors R.V. Patel and K. Khorasani, who introduced me to this challenging research area. Their comments and suggestions on most of the theoretical developments made in this thesis, and also on computational and practical aspects of real–time control have been instrumental in the completion of this research. I appreciate their invaluable guidance, encouragement, and support which greatly changed my way of thinking in dealing with control engineering problems.

I thank members of my qualifying exam committee, who through their questions, suggestions, and interest gave me the confidence and sense of validation for going further.

I am grateful to my friends Keyvan, Farshid, Javad, and Ali with whom I have had several discussions on the project. Thanks too to Danny Juras of the Mechanical Engineering Concave Center for helping me install the strain gauges, Paul Scheiwiller of the Faculty of Engineering Workshop for building the experimental robot, and Guy Gosselin of the Electrical and Computer Engineering department, for his assistance in the experimental phase of the project.

Finally, I would like to thank my wife and daughter for their support and understanding. I wish to thank my parents and parents–in–law for their encouragement, support, and endurance during the past few years that we have been far away from them.

CONTENTS

LIST OF FIGURES

Chapter 1

Introduction

In this chapter several issues are discussed regarding the modeling, control, and design of flexible–link robotic manipulators. The philosophy and technical difficulties associated with these robots are illustrated in section 1.1. Section 1.2 covers a literature review on the modeling of flexible–link manipulators. By modeling, we mean the plant dynamics that are used for the purpose of control. The control strategies are outlined in section 1.3 and the design problem is discussed in section 1.4. In section 1.5, we consider some topics related to the control problem of these robots. Some examples are also given from other fields which have similar difficulties from the control point of view. Finally, the contributions of this dissertation are stated briefly in section 1.6.

1.1 Motivation

The modeling, design, and motion control of structurally flexible robotic manipulators has been the focus of attention of researchers in the past few years. This field of research has been attractive because of several reasons. For instance, space applications require low–mass designs, to achieve escape velocity, and in order to accomplish a mission with better fuel economy. This restriction puts a limitation

on the degree of rigidity of space robots. On the other hand, increased structural flexibility may be desirable in tasks such as cleaning delicate surfaces, or avoiding damages to the manipulator system due to accidental collisions. Still the problem may be viewed from other angles such as high–speed manipulation and increased productivity. The conventional manipulators are limited to a load–carrying capacity of 5-10 percent of their own weight. This restriction is mainly due to the requirement of having a stable closed–loop system. This has encouraged the design of heavy (rigid) robots so as to have less stringent control problems. Thus, the designers of earth-bound robots have solved the control problem by making the manipulators more rigid using bulkier structures. Likewise, for light–weight space based systems, one simple solution is to move the manipulators slowly.

Achieving exact, high–speed manipulation with lightweight structures, is definitely a desirable objective. Such an achievement is also attractive from energy consumption considerations since smaller actuators are needed due to lighter loads. Regardless of the reason that flexibilities become significant, precise and stable control of the manipulator tip is desirable. This requires the inclusion of deformation effects due to the flexibility of the arms in the dynamic equations, and generally tends to complicate the analysis and design of the control laws. In flexible link manipulators, a major difficulty arises when one tries to track a specific tip position trajectory by applying the torques at the actuation ends. Due to the non-colocated nature of sensors and actuators, the zero-dynamics of the system become unstable. The zero-dynamics are defined as the internal system dynamics when the outputs are driven to zero by specific inputs. The system is called non-minimum phase when these dynamics are unstable. This intrinsic non-minimum phase property hinders exact asymptotic tracking of a desired tip trajectory if causal controllers are employed. Thus in practice one may be satisfied with small (rather than zero) tracking errors. More details on this are given in section 1.5.

This dissertation aims to address two major issues regarding flexible–link manipulators: Plant design and control design. The plant to be controlled is the robotic manipulator and we are interested in devising control strategies that take into account the flexural effects as well. The first aim is to alter the plant characteristics such that the final plant has some desirable features from the control point of view. This should be achieved without any sacrifice to some specifications such as the total mass or the moments of inertia experienced by the actuators. There is certainly a limit to which improvement may be achieved, and the rest of the effort is the job of the controller. Thus we are concerned with the mechanical design of the manipulator on the one hand and controller design on the other hand. By mechanical design, we mean improved structural shapes. The type of material used in design is a key issue and plays an important role. A material with a high modulus of elasticity, a low mass density, and high structural damping is the solution to most problems of flexibility. Here it is assumed that the type of material is specified. This specification may be considered as the ultimate restrictions put forth either by materials technology or economic considerations. The other side of the coin is the control problem. In this respect, a dynamic model that describes the system behavior in a concise and accurate way is desirable. Improved dynamic modeling allows for reliable design and control. Theoretically the dynamic equations are infinite dimensional and may be described by partial differential equations. This is simply due to the fact that an infinite number of coordinates are required to kinematically describe each link. However, an infinite dimensional model may not be suitable for control system design. This is due to factors such as the dynamic model complexity and the band–limited nature of sensors and actuators. In the modeling phase, one usually truncates the number of flexible coordinates. In any case, the dynamics turn out to be a highly nonlinear and coupled set of differential equations which enjoy a two–time–scale nature. Another major question in controller design are the number and type of sensing points. Since tip positions and their rates of change

with time are to be controlled, the least information to be provided to the controller is accurate information on tip positions. In particular, tip position information can be provided by using camera vision or strain gauge measurements, however tip rate measurements are not directly obtainable.

1.2 Dynamic Modeling

Like rigid manipulators, knowledge of the dynamic model of a structurally flexible manipulator is needed for the purpose of simulation (forward dynamics), inverse dynamics and more importantly, for the design of the controller. For rigid–link manipulators it is known that once the kinematics of the chain of rigid bodies are properly defined, the set of dynamic equations can be obtained by conventional methods such as Newton–Euler or Lagrangians [32]. In principle, all sets of dynamic equations derived based on different kinematic descriptions are equivalent. However, this is not usually true for flexible–link manipulators. The main reason is that the actual system dynamics are infinite dimensional because of the distributed link flexibility. To simplify the problem a conventional method is to approximate the flexible–link system by a system with a finite number of degrees of freedom. The method of approximation is the source of difference in the dynamic equations. In what follows we review some of these methods.

A great deal of research in modeling and control of flexible link robots has focussed on a single link flexible beam free to rotate and flex in a horizontal plane (see Figure 1.1). Neglecting second order effects such as rotary inertia, shear deformation and actuator dynamics, the dynamics of position $y(x,t)$ of any point on the beam is given (e.g.[15]) by the Euler-Bernouli beam equation

$$EI\frac{\partial^4 y(x,t)}{\partial x^4} + m\frac{\partial^2 y(x,t)}{\partial t^2} = 0 \qquad 0 < x < l \tag{1.1}$$

where E is Young's modulus of elasticity of the material, I is the area moment of inertia of the cross section about the z–axis, m is the mass per unit length of the

arm, and l is the length of the arm. Note that $y(x,t) = \theta x + w(x,t)$, and the hub angle $\psi = \frac{\partial y(0,t)}{\partial x} = \theta + \frac{\partial w}{\partial x}|_{x=0}$. The boundary conditions of (1.1) at $x = 0$ are as follows

$$y(0,t) = 0 \tag{1.2}$$

$$EI\frac{\partial^2 y}{\partial x^2} + u = J_h \frac{d^2}{dt^2}(\frac{\partial y}{\partial x}) \tag{1.3}$$

where J_h is the hub inertia and u is the actuating torque, and at $x = l$

$$Bending\ Moment: EI\frac{\partial^2 y}{\partial x^2} = -Jp\frac{d^2}{dt^2}(\frac{\partial y}{\partial x}) \tag{1.4}$$

$$Shear\ Force: EI\frac{\partial^3 y}{\partial x^3} = M_p \frac{d^2}{dt^2} y \tag{1.5}$$

where J_p, M_p are the payload inertia and mass respectively.

The flexible–link described in (1.1) has been the subject of many research projects. Cannon and Schmitz [2] used the assumed modes method to model the flexible link. They have assumed zero payload and pinned–free eigenfunctions for mode shapes. With this approximation, the mode shapes form a complete set of orthogonal functions with the rigid body mode shape given by $\phi_0(x) = x$. Using the Lagrangian formulation and taking into account the structural damping of the beam, a set of decoupled differential equations are obtained which can be put in the form of a linear state–space model. Hastings and Book [1] followed a similar approach in modeling. They have experimentally verified that clamped–mass admissible functions (mode shapes) yield better results than other mode shapes such as pinned–free used by Cannon and Schmitz. Two mode shapes have been used for modeling and acceptable agreement with theory has been reported. Wang and Vidyasagar [36] have used clamped–free mode shapes and have theoretically shown that if the number of modes is increased to obtain a more accurate model of the flexible link, the transfer function from torque input to tip position output does not have a well defined relative degree. To alleviate this problem they propose a re–definition of the output as the *reflected tip position* that can be easily measured.

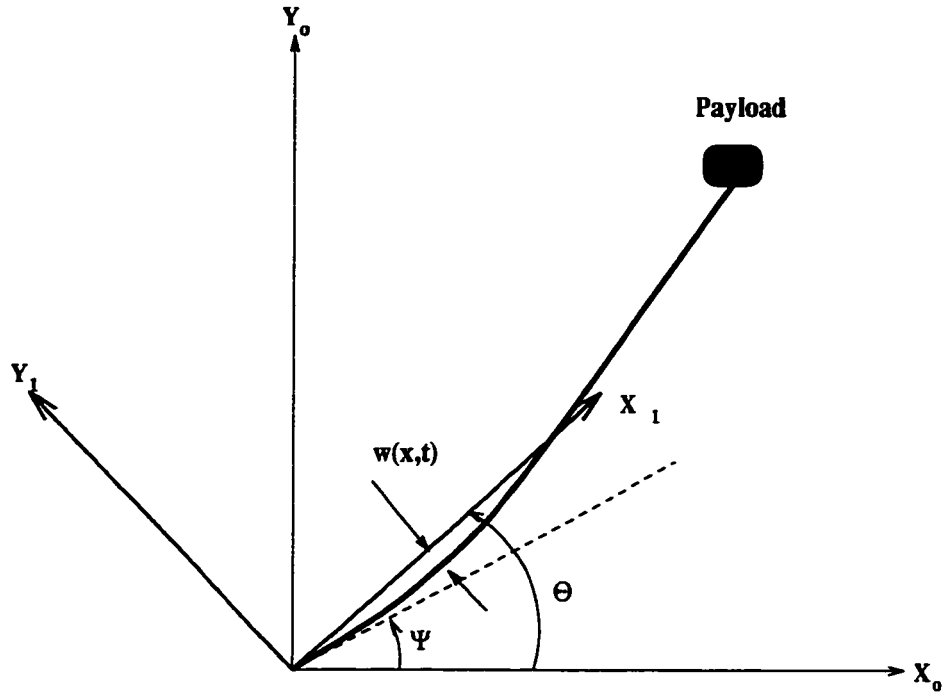

Figure 1.1: The one link flexible arm.

Pota and Vidyasagar [11], and Wang and Vidyasagar [12] further discuss the passivity of the resulting transfer function and conclude that any strictly passive cascade controller will stabilize the system and the controllers become simpler. Bellezza *et.al* [4] have shown that the open loop models obtained by using clamped–free and pinned–free eigenfunctions are identical and only differ in the reference frame in which the elastic deflections are measured. It should be noted that the actual boundary conditions given by (1.2)–(1.5) are neither pinned–free nor clamped–free. In fact, the boundary conditions are time varying and depend on the input torque profile. Cetinkunt and Yu [5] have compared the first three modes of the closed–loop system for pinned-free and clamped–free mode shapes with the modes obtained from the exact solution of the Bernouli–Euler beam equation. For both tip position proportional–derivative (PD) controller and hub angle PD controller, they have shown that the predictions of clamped–free mode shapes are much more accurate than the predictions of pinned–free mode shape models. Bayo [6] uses Hamilton's

principle and a finite element approach to model a single flexible–link arm. One advantage of this method is that different material properties and boundary conditions like hubs, tip loads and changes in cross section can be handled in a simple manner. Usoro *et.al* [7] use a finite-element Lagrange method to model multi–link flexible robots, but no comparison is made with other schemes and the model is not validated with experimental evidence. There have been a few other approaches to modeling multi–link flexible robots. Book [29] introduced a recursive Lagrangian assumed modes method to model a flexible–link manipulator in three dimensional space. The method is applicable to revolute–joint robots and gives rise to dynamic equations of the form

$$M(z)\ddot{z} + h(z,\dot{z}) + Kz = Bu \tag{1.6}$$

where $M(z)$, K are the positive definite inertia and stiffness matrices, $h(z,\dot{z})$ is the vector of Coriolis and centrifugal terms, z is the vector of generalized coordinates (joint positions and deflection coordinates), B is a constant matrix which depends on the shape functions used, and u is the vector of input torques. A complete model for a two-link manipulator is given in [9]. Benati and Morro [10] consider the modeling of a chain of flexible links by describing the deflection $w(x_i,t)$ of each point on link i as

$$w(x_i,t) = a_1(t)\phi_1(x_i) + a_2(t)\phi_2(x_i) \tag{1.7}$$

where ϕ_1, ϕ_2 are the first two eigenfunctions of the clamped–mass beam with a mass equal to the total mass of the links and payload after link i. The deflection equation (1.7) can then be related to ψ_i and δ_i quantities by (see Figure 1.2)

$$w(x_i,\psi_i,\delta_i) = \alpha(x_i,l) + \beta(x_i,l)\delta_i \tag{1.8}$$

where l is the link length and α, β are known functions. The kinetic and potential energies are then found based on this kinematic description and the Lagrangian method is used to derive the dynamic equations.

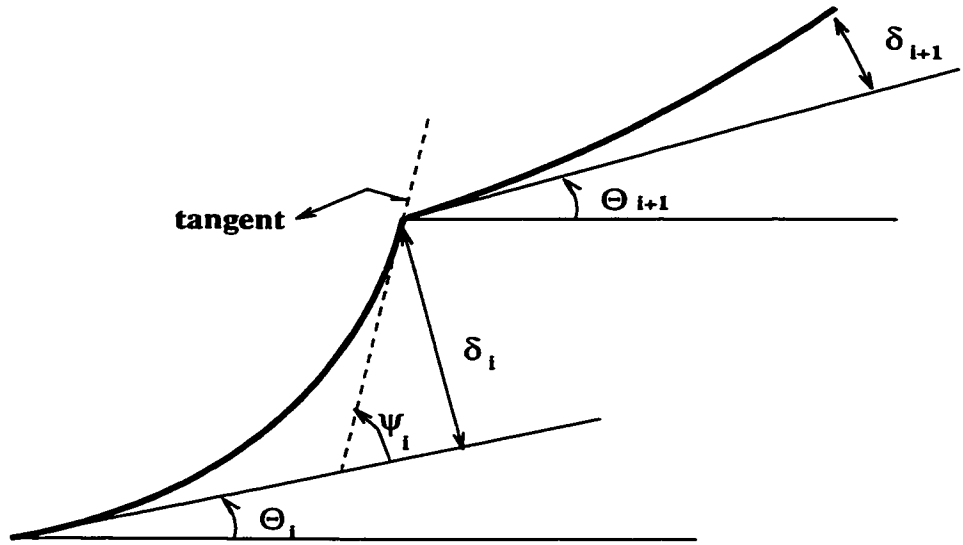

Figure 1.2: Chain of flexible links.

Yoshikawa *et.al* [13] have modeled each link of a three degree of freedom flexible robot with two flexible links using a lumped parameter approximation. The mass of each link is assumed to be negligible and a lumped mass is considered at the tip of each link. The flexibility effects are approximated by lumped torsional and longitudinal springs attached at the end point of each link. These quantities are in terms of the links geometry and material properties such as mass density and modulus of elasticity. The modeling is again carried out using the Lagrangian formulation. De Luca *et.al* [14] have conducted experiments on a two–link robot with a flexible forearm. The modeling is similar to that in [9]. They have reported the accuracy of the flexible part of their model based on experimental observations. For a rather severe trajectory, it is concluded that the first vibrational mode is significantly excited and the model with two vibration modes has been reported to yield satisfactory results.

1.3 Control Strategies

Most of the research in the area of flexible–link manipulator control has been applied to the case of a single flexible arm. However there is one major critique in this regard. In the multi–link case, the mass matrix contains joint position variables, which introduce considerable nonlinearities in the dynamic equations. For a single flexible link the mass matrix is only a function of deflection variables- which are quadratic type nonlinearities. Thus a single–link may well approximate a linear system, while this is not true in the multi–link case. In spite of this fact, the experiments conducted with a single link case provide a basis for multi–link investigations, since both cases suffer from the undesirable non–minimum phase property [66]. This property shows up when the controlled output is the end–effector position. In such a case a critical situation is encountered when one tries to apply standard inversion techniques for exact trajectory tracking. Any attempt to achieve exact tracking via inversion results in unbounded state trajectories and unstable closed–loop system. The less difficult problem of end–point stabilization may also become troublesome, although not impossible, because of the non–minimum phase nature. On the other hand, the tracking of joint trajectories can always be obtained in a stable fashion in the presence of link flexibilities. This may of course yield unacceptable tip position errors. We will discuss the problem in more detail in section 1.5.

Of the early experimental work in this area, the work of Cannon and Scmitz [2], Hastings and Book [1], among others, aim at the end–point regulation problem. Output re–definition may be a key to achieving smaller tracking errors. To this end, Wang and Vidyasagar [36] introduced the reflected–tip position as a new output for a single flexible link. De Luca and Lanari [37] studied the regions of sensor and actuator locations for achieving minimum phase property for a single flexible link. Wang and Vidyasagar [56] have shown that the nonlinear flexible–link system is not in general input–state feedback linearizable, however the system is locally input–output linearizable.

Nemir *et.al* [64] introduced the pseudo–link concept but have not addressed the non–minimum phase issue associated with the tip output. Other approaches have been proposed to deal with the exact tracking problem. Bayo [6], and Kwon and Book [24] introduced noncausal controllers for the purpose of exact trajectory tracking. However their approaches typically require heavy computation and have been restricted to the linearized single–link case. Based on the concept of pole assignment in linear systems, transmission zero assignment was introduced by Patel and Misra [41] and applied by Geniele *et.al* [54] to a single–link flexible manipulator. Here the basic idea is to add a feedforward block to the plant so that the zeros of the new system are at prescribed locations in the left half–plane. It is then possible to use output feedback and ensure that the closed–loop system poles are at good locations in the left half–plane. The work of Hashtrudi–Zaad and Khorasani [42] which is based on an integral manifold approach may also be interpreted as a form of output re–definition. In this work, new *fast* and *slow* outputs are defined and the original tracking problem is reduced to tracking the *slow* output and stabilizing the *fast* dynamics.

Input–shaping control was implemented, among others, by Hillsley and Yurkovich [25], Tzes and Yurkovich [26], and Khorrami [27]. This approach essentially involves the convolution of a sequence of impulses with the reference inputs to suppress the tip–position vibrations. This can be accomplished by coloring the input such that no energy is injected around the flexible modes, or by filtering out the frequencies around the flexible modes using notch filters. The validity of such methods depends on the exact knowledge of the flexible structure dynamics. Also such methods are open loop in essence.

The nonlinear approach to the design of controllers has also been addressed, although to a lesser extent by some authors, e.g., [8], [16], [48], [49],[56]. In this regard, the approach based on the singular perturbation theory [81], [44] has been attractive due to the two–time–scale nature of the system dynamics. To this end,

Siciliano and Book [8] furnished a singular perturbation model for the case of multi–link manipulators which follows a similar approach in terms of modeling to that introduced by Khorasani and Spong [46] for the case of flexible–joint manipulators. Their control strategy is then based on stabilizing the fast dynamics and tracking the joint trajectories. The same strategy is also addressed by [16], [48], [49]. Mostly these researchers have taken joint positions as outputs to avoid the problems due to the non–minimum phase nature of the plant. A comparison is made experimentally between some of these methods by Aoustin *et.al* [50]. However, taking joint positions as the outputs has the drawback of large tip position errors, especially when the singular perturbation parameter is not small enough.

Wang and Vidyasagar [56] studied the input–state feedback linearization problem and showed that the system is not in general linearizable, however it is input–output linearizable. The input–output linearization in the nonlinear systems theory is essentially based on the works of Hirschorn [18] and Byrnes and Isidori [19]. To this end, the tip positions cannot be selected as the outputs due to the instability of the unobservable dynamics associated with such choice of outputs. Thus the definition of another output may seem unavoidable. Such outputs should naturally be selected such that small enough tracking errors are achieved [37], [38].

Recently, intelligent control methods have been applied to flexible–link manipulators [39]. Intelligent control is the discipline in which control algorithms are developed by emulating certain characteristics of intelligent biological systems. Moudgal *et. al* [39] have implemented a *fuzzy* supervisory control law for vibration damping of a flexible two–link manipulator. However, an unbiased and accurate comparison of intelligent and classical control strategies is not yet available in the literature. Therefore, more benchmark comparisons should be made before one can come to any conclusion regarding the employment of intelligent, classical, or a combination of both methods.

1.4 Mechanical Design

As was mentioned previously, by mechanical design we mean constructing the optimum shape of the links of a manipulator such that some desirable features are achieved. Parallel to this line of research the use of advanced materials in arm construction should not be overlooked. One example is using distributed actuators and sensors as described in [28]. As pointed out by Asada, *et.al* [21], the majority of flexible manipulators that have been addressed in the literature have a simple structure consisting of beams with uniform mass and stiffness distribution. While the simplified beams allow for analytic modeling and theoretical treatment, the arm construction is unrealistically primitive and its dynamic performance is severely limited. Compensating for the poor dynamics merely by control may require a lot of control energy and heavy computation. Therefore, alteration of plant dynamics to achieve less stringent control strategies can be pursued in this regard.

The design process regarding arm shape design to achieve properties such as low mass and moments of inertia and high natural frequencies generally boils down to the solution of an optimization problem. Asada *et.al* [21] have obtained the optimum torque application point and structural shape for a single flexible arm. The torque application point affects system zeros and the structural shape mostly affects the modal frequencies. The experimental results obtained show a twenty five percent increase in the lowest natural frequency and the plant requires less stringent control strategy due to a robust allocation of the torque transmission mechanism. A few other published works have recently appeared in this area (e.g. [22], [82]).

1.5 Some Related Topics

In this section, we review some basic concepts and definitions that are related to the control of flexible–link manipulators. The challenge of control in these manipulators stems from several sources. First, the dynamic equations are highly coupled and

nonlinear. Second, these equations are *stiff* due to the time–scale separation of the *slow* rigid modes and the *fast* flexible modes. Third, the presence of right half–plane transmission zeros in a non–colocated sensor–actuator configuration imposes limitations on the control problem, both in trajectory tracking and set–point regulation. These factors will create problems in control design, analysis and simulation as we will briefly discuss in this chapter.

The study of control for these manipulators is also stimulating if one considers similarities with other control problems. We will give a few examples from other applications where the controller has to cope with plant nonlinearities and unstable zero–dynamics with essentially similar characteristics.

1.5.1 Regulation and Tracking

The task of every control problem can generally be divided into two categories: Regulation (or stabilization) and tracking (or servoing). In the regulation problem, one is concerned with devising the control law such that the system states are driven to a desired final equilibrium point and stabilized around that point. In the tracking problem, one is faced with devising a controller (tracker) such that the system output tracks a given time–varying trajectory. Some examples of regulation problems are: Temperature control of refrigerators, AC and DC voltage regulators, and joint position control robots. Examples of tracking problems can be found in tracking antennas, trajectory control of robots for performing specific tasks, and control of mobile robots.

The formal definitions of the above control problems can be stated as follows [66]

Regulation Problem: *Given a nonlinear dynamic system described by*

$$\dot{x} = f(x, u, t) \tag{1.9}$$

where x is the $n \times 1$ state vector, u is the $m \times 1$ input vector, and t is the time variable, find a control law u such that, starting from anywhere in a region in $\Omega \subset R^n$, the

state tends to zero as $t \rightarrow \infty$.

Similarly

Tracking Problem: *Given a nonlinear dynamic system and its output vector described by*

$$\begin{aligned} \dot{x} &= f(x,u,t) \\ y &= h(x) \end{aligned} \tag{1.10}$$

and a desired output trajectory $y_d(t)$*, find a control law for the input* u *such that, starting from an initial state in a region* $\Omega \subset R^n$*, the tracking error* $y(t) - y_d(t)$ *approaches to zero while the whole state* x *remains bounded.*

The control input u in the above definitions may be either called *static* if it depends on the measurements of the signals directly, or *dynamic* if it depends on the measurements through a set of differential equations. Tracking problems are generally more difficult to solve than regulation problems. One reason is that, in the tracking problem, the controller has to drive the outputs close to the desired trajectories while maintaining stability of the whole state of the system. On the other hand, regulation problems can be regarded as special cases of tracking problems when the desired trajectory is constant with time.

In this thesis we are concerned with the tip–position tracking problem of flexible–link manipulators. To get more insight into the nature of this problem we will first review some concepts such as internal dynamics, zero–dynamics, and non–minimum phase characteristic in the nonlinear framework. Towards this end let us consider a class of square nonlinear systems given by (1.10) that are linear in the input u (affine systems), i.e.,

$$\begin{aligned} \dot{x} &= f(x) + g(x)u \\ y &= h(x) \end{aligned} \tag{1.11}$$

Let $x \in R^n$, $u \in R^p$, $y \in R^p$. Further, assume that the column vector fields $f(x)$, $g_i(x)$ $(i = 1,...,m)$, and the functions $h_i(x)$ $(i = 1,...,p)$ are smooth on an open

set of R^n. We are interested in tracking the output vector y while keeping all other states reasonably bounded. In this regard, a representation of (1.11) in terms of the output vector and its time derivatives would prove helpful. Towards this end, assume that the system (1.11) has well defined vector relative degree ([31])

$$r = [r_1,\ r_2,\ ...,\ r_p] \tag{1.12}$$

in a neighberhood of origin $x = 0$. Also assume that $f(0) = 0$ and $h(0) = 0$. The assumption of a well defined relative degree implies that if we successively differentiate $y_i(t)$ with respect to t, then some component $u_j(t)$ of the input $u(t)$ appears for the first time at the r_ith derivative of y_i.

Through state–dependent coordinate and input transformations, ([31]), we may input–output linearize the plant (1.11) so that it takes the equivalent representation

$$\begin{aligned}
\dot{\xi}_i^j &= \xi_{i+1}^j, \quad i \in \{1,\ ...,\ p\},\ j \in \{1,\ ...,\ r_i - 1\} \\
\dot{\xi} &= u_i, \quad i \in \{1,\ ...,\ p\} \qquad (1.13) \\
\dot{\eta} &= \alpha(\xi, \eta) + \beta(\xi, \eta)u \\
y_i &= \xi_1^i, \quad i \in \{1,\ ...,\ p\} \qquad (1.14)
\end{aligned}$$

where

$$\xi := \Psi(x) = \begin{bmatrix} \xi_1^1 \\ \xi_2^1 \\ \vdots \\ \xi_{r_1}^1 \\ \xi_1^2 \\ \vdots \\ \xi_{r_2}^2 \\ \xi_1^p \\ \vdots \\ \xi_{r_p}^p \end{bmatrix} = \begin{bmatrix} y_1 \\ \dot{y}_1 \\ \vdots \\ y_1^{(r_1-1)} \\ y_2 \\ \vdots \\ y_2^{(r_2-1)} \\ y_p \\ \vdots \\ y_p^{(r_p-1)} \end{bmatrix} \tag{1.15}$$

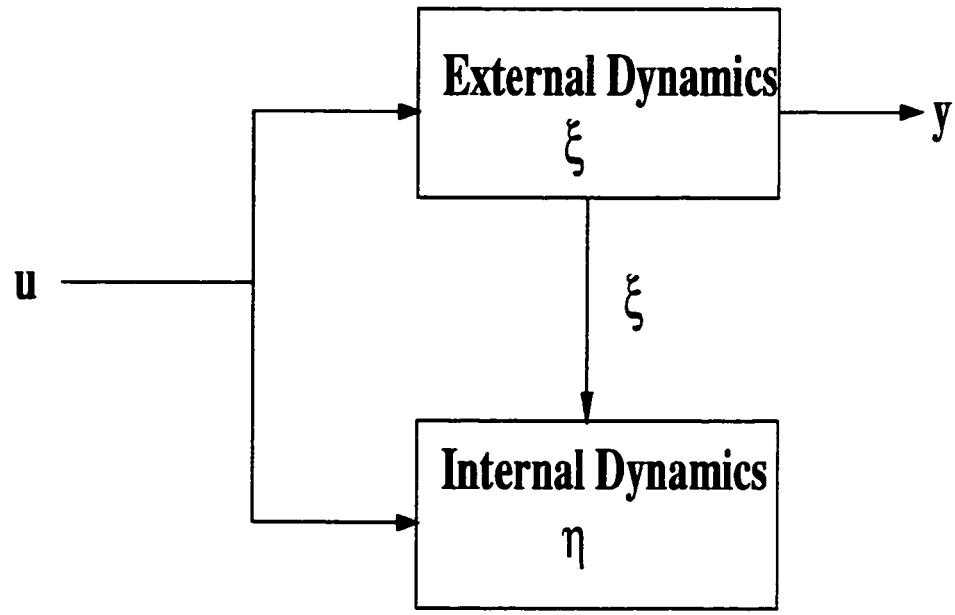

Figure 1.3: Representation of the system in internal and external dynamics.

The ξ vector represents part of the dynamics in the form of p integrator chains, each of length r_i, $i \in \{1, ..., p\}$, and $\eta^T = [\eta_1, \cdots, \eta_{n-p}]$ ($\eta_i = \phi_i(x)$, $i = 1, \cdots, n-p$), are smooth functions of x such that the state transformation $(\xi, \eta) = \Psi(x) := (\psi(x), \phi(x))$ is a (local) diffeomorphism at the origin.

The structure of (1.13)–(1.14) is illustrated in Figure 1.3. The dynamics of η are referred to as *internal* dynamics. These dynamics are obtained from (1.14) with ξ regarded as an exogenous time–dependent function. Now the *zero–dynamics* of the system in Figure 1.3 are defined as the internal dynamics of the system when the inputs act such that the output is identically zero ($u \equiv 0$, $\xi \equiv 0$). In the representation thus obtained the zero–dynamics are given by

$$\dot{\eta} = \alpha(0, \eta) \tag{1.16}$$

If the zero–dynamics of (1.16) are asymptotically stable then the original system is a minimum–phase system. Otherwise the system is nonmimimum–phase. These terms are adapted from linear system theory. If a transfer function $H(s)$ of a linear system has a zero in the right half of the complex plane, the transfer function, when

evaluated for s going along the imaginary axis from $-j\infty$ to $+j\infty$, undergoes a change in phase which is greater, for the same magnitude, than if that zero were replaced by its left–half plane mirror image; hence the name non–minimum phase. In linear systems the minimum–phase characteristic can be checked in different ways. To this end the transmission zeros of an nth–order m input, m output linear system of the form

$$\begin{aligned} \dot{x} &= Ax + Bu \\ y &= Cx \end{aligned} \tag{1.17}$$

are defined as those values of λ for which

$$rank \begin{bmatrix} A - \lambda I_n & B \\ C & 0 \end{bmatrix} < n + m \tag{1.18}$$

Similarly, if CB is invertible the transmission zeros are the finite eigenvalues of $A + gBC$ as $g \to \infty$. The latter definition has an interesting interpretation: When static output feedback ($gI_{m\times m}$) is used the poles of the closed–loop system are attracted towards the transmission zeros as the feedback gain g is increased. Thus if the system has right–half plane transmission zeros (non–minimum phase) the closed–loop system can become unstable under static output feedback.

1.5.2 Some Examples of Non–Minimum Phase Systems

In the rest of this section we will consider some examples in other areas with non–minimum phase behavior. Most of these examples are from underactuated mechanical systems which are somehow similar to the underactuated flexible–link system.

The Acrobat

The acrobatic–robot [87] or *acrobot* (see Figure 1.5) is a highly simplified model of a human gymnast performing on a single parallel bar. By swinging his/her legs (a

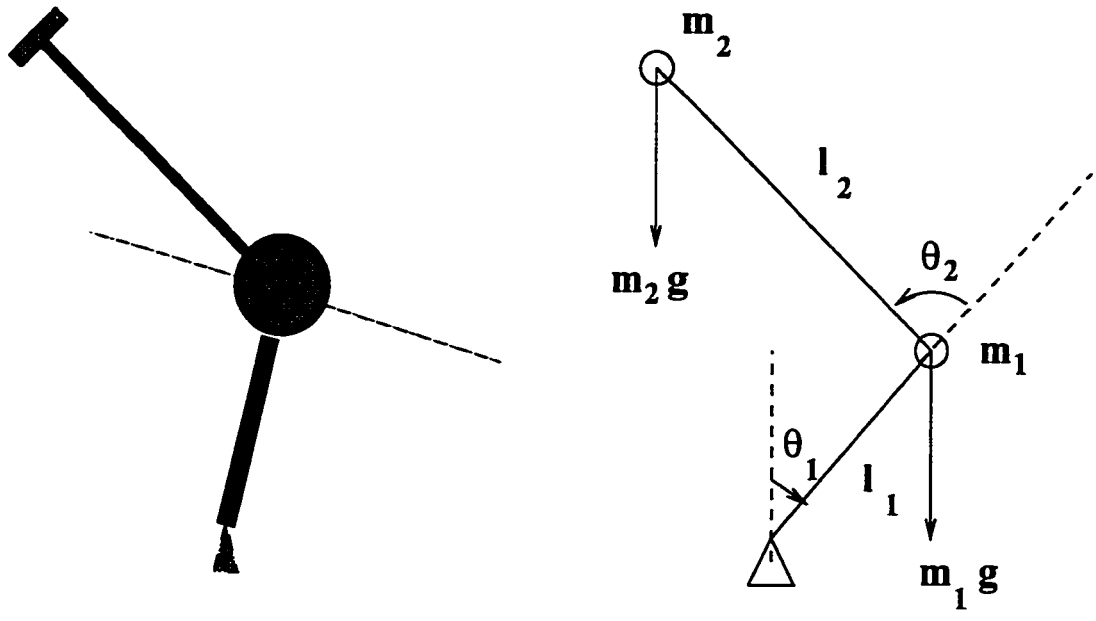

Figure 1.4: Acrobot: An acrobatic robot.

rotation at the hip) the gymnast is able to bring himself/herself into a completely inverted position with the feet pointing upwards and the center of mass above the bar. The acrobot consists of a simple two–link manipulator operating in a vertical plane. The first joint (corresponding to the gymnast's hand sliding freely on the bar) is free to rotate. A motor is mounted at the second joint, between the links, to provide torque input to the system. This corresponds to the gymnast's ability to generate torques at the hip. The acrobot is also a good model for under–actuated mechanical systems such as unicycles and walking machines, where *balance* must be maintained while trying to accomplish the assigned task. The dynamics of the acrobot can be obtained using the Lagrangian formulation, and have the general form

$$M(\theta)\ddot{\theta} + C(\theta, \dot{\theta}) + G(\theta) = \begin{pmatrix} 0 \\ \tau \end{pmatrix} \tag{1.19}$$

where $\theta = (\theta_1, \theta_2)$ are the joint angles, M is the positive–definite inertia matrix, C contains the Coriolis and centrifugal forces, G contains the effects of gravity, and τ

is the torque applied between the first and second links.

Now modeling the acrobot shown in Figure 1.5 with $m_1 = m_2 = 8kg$, $l_1 = 0.5m$, $l_2 = 1m$, and $g = 10m/s^2$ results in

$$\begin{aligned} M(\theta) &= \begin{bmatrix} 12 + 8cos\theta_2 & 8 + 4cos\theta_2 \\ 8 + 4cos\theta_2 & 8 \end{bmatrix} \\ C(\theta, \dot{\theta}) &= \begin{bmatrix} -4\dot{\theta}_2(2\dot{\theta}_1 + \dot{\theta}_2)sin\theta_2 \\ 4\dot{\theta}_1^2 sin\theta_2 \end{bmatrix} \\ G(\theta) &= \begin{bmatrix} -80(sin\theta_1 + sin(\theta_1 + \theta_2)) \\ -80sin(\theta_1 + \theta_2) \end{bmatrix} \end{aligned} \tag{1.20}$$

Consider the equilibrium point corresponding to $\theta_1 = \theta_2 = 0$, and choose the desired output to correspond to θ_1, i.e., $y = \theta_1$. Then the zero–dynamics of this system can be obtained by finding an input that restricts the system output identically to zero and considering the resulting internal dynamics. To this end setting y, $\dot{y}$, $\ddot{y}$ to zero yields from the first equation in (1.19) the zero–dynamics

$$(8 + 4cos\theta_2)\ddot{\theta}_2 - 4\dot{\theta}_2^2 sin\theta_2 - 80sin\theta_2 = 0 \tag{1.21}$$

and the corresponding input is obtained from the second equation in (1.19), i.e.,

$$8\ddot{\theta}_2 - 80sin\theta_2 = u \tag{1.22}$$

Around the equilibrium point $\theta_2 = 0$, $\dot{\theta}_2 = 0$, the dynamics given by (1.21) can be linearized to yield

$$12\ddot{\theta}_2 - 80\theta_2 = 0 \tag{1.23}$$

Thus the zero–dynamics are *unstable* at this equilibrium point. Physically these dynamics correspond to the dynamics of the second link (an inverted pendulum) when θ_1 (output) is restricted to zero. Moreover, equation (1.22) illustrates how the control input is affected by the *unstable* zero–dynamics in order to maintain balance at $\theta_1 = \theta_2 = 0$. It can be shown that taking θ_2 as the output will result in unstable zero–dynamics again.

PVTOL Aircraft

We consider the planar vertical takeoff and landing (PVTOL) aircraft given in [88]. Referring to Figure 1.5 the aim is to control the position of the aircraft. Thus the outputs to be controlled are x and y. Simplified equations of motion for this system are

$$\begin{aligned} \ddot{x} &= -u_1 sin\theta + \epsilon u_2 cos\theta \\ \ddot{y} &= u_1 cos\theta + \epsilon u_2 sin\theta - 1 \\ \ddot{\theta} &= u_2 \end{aligned} \tag{1.24}$$

where "-1" is the gravitational acceleration and ϵ is the (small) coefficient giving the coupling between rolling moment and the lateral acceleration of the aircraft. The control inputs u_1, u_2, are the thrust (directed out from the bottom of the aircraft) and the rolling moment. The non–minimum phase character of aircraft is a result of small body forces that are produced in the process of generating body moments. Here since the roll moment reaction jets create a force that is not perpendicular to the lateral axis of the aircraft, the production of a positive rolling moment (to the pilot's right) will also produce a slight acceleration of the aircraft to the left. This phenomenon makes the aircraft non–minimum phase. Thus taking x and y as the outputs, the zero dynamics are obtained by first differentiating each output until at least one input appears and then setting each output identical to zero. This will lead to the following equivalent representation

$$\begin{aligned} \ddot{x} &= v_1 \\ \ddot{y} &= v_2 \\ \ddot{\theta} &= \frac{1}{\epsilon}(sin\theta + cos\theta v_1 + sin\theta v_2) \end{aligned} \tag{1.25}$$

Thus the zero–dynamics are given by

$$\ddot{\theta} = \frac{1}{\epsilon} sin\theta \tag{1.26}$$

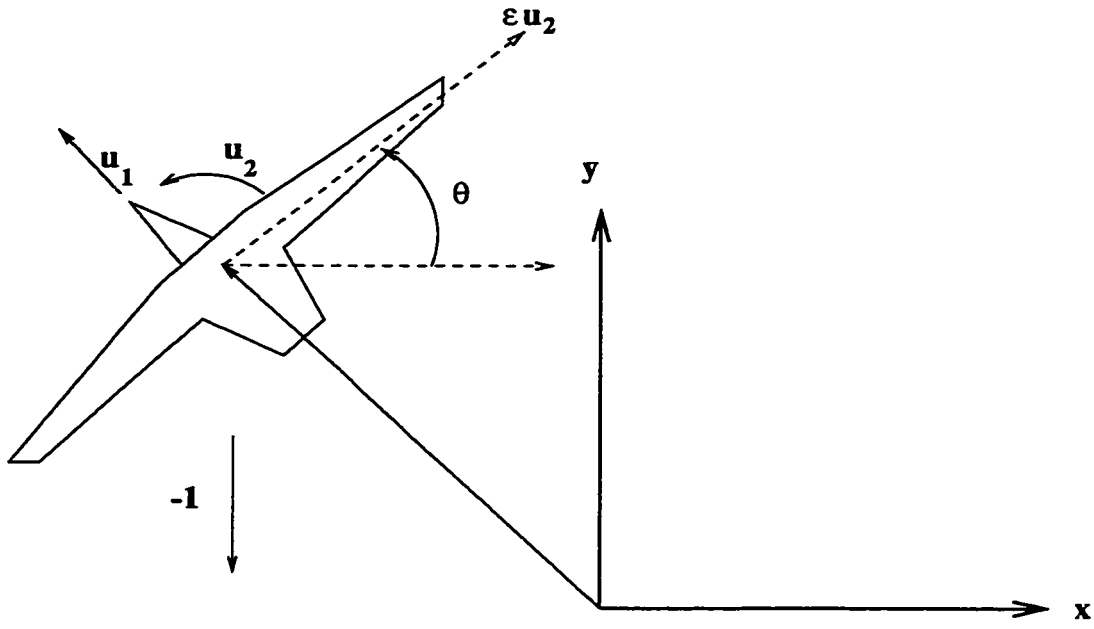

Figure 1.5: The planar vertical takeoff and landing (PVTOL) aircraft.

The above equation is reminiscent of the dynamics of an undamped pendulum which is not asymptotically stable. This undamped behavior may produce undesirable aircraft response. For example if y is to be kept at zero by v_2 and x is forced to track a smooth trajectory by v_1, the aircraft will acquire a pendulum–like motion which may not be desirable.

Another non–minimum phase characteristic in aircraft dynamics is the response of aircraft altitude to the deflection of the elevator angle [66]. This will show itself in an initial downward motion when an attempt is made to move upward. Of course, such non–minimum phase behavior is important for the pilot to know, especially when flying at low altitudes.

Flexible–Link Manipulators

To illustrate the non–minimum phase characteristic in flexible–link systems we consider a single–link flexible arm as shown in Figure 1.1. A linearized dynamic model of this arm can be found by using the method of assumed modes and Lagrangian

formulation. When a single flexural mode is used the following dynamics result

$$\begin{aligned} m_{11}\ddot{\theta} + m_{12}\ddot{\delta} &= u \\ m_{12}\ddot{\theta} + m_{22}\ddot{\delta} + k\delta + d\dot{\delta} &= 0 \end{aligned} \tag{1.27}$$

where m_{ij}, $i,\ j \in \{1,2\}$, are components of the mass matrix given, for zero payload, by

$$m_{11} = \rho A l^3/3 + J_h, \quad m_{12} = \int_0^l \phi(x) x \rho A dx, \quad m_{22} = \rho A \tag{1.28}$$

where A is the link's cross sectional area, ρ is its mass density, $\phi(x)$ is the modal shape function, and k is the stiffness coefficient of the beam given by

$$k = EI \int_0^l (\frac{d^2\phi}{dx^2})^2 dx \tag{1.29}$$

In (1.29), E is the link modulus of elasticity and I is the cross sectional area moment of inertia. Also in (1.30), d is the damping coefficient of the flexural mode, and u is the input torque. Defining the output y as the tip position and $\phi_e = \phi(l)$, we have

$$y = \theta + \phi_e \delta \tag{1.30}$$

where $\phi_e = \phi(l)$. As before the zero–dynamics can be found by setting y identically zero, which yields

$$u = (m_{12} - m_{11}\phi_e)\ddot{\delta} \tag{1.31}$$

$$0 = (m_{22} - m_{12}\phi_e)\ddot{\delta} + d\dot{\delta} + k\delta \tag{1.32}$$

The zero dynamics represented by (1.32) are generally unstable since $m_{12} - m_{11}\phi_e < 0$. Note that by using (1.28) the latter term is given by $\rho A(1 - \phi_e \int_0^l x\phi(x)dx)$. Now, assuming a clamped–free mode shape it can be concluded from $\phi(x) < \phi_e$ that $\phi_e \int_0^l x\phi(x)dx < \phi_e^2 l^2/2$. Therefore, if l is large enough the first coefficient in (1.32) is negative, i.e., unstable zero–dynamics. The nonminimum–phase condition in this case is a result of the non–colocated sensor and actuator positions. The

system is under–actuated as in previous examples and the input torque affects the tip position through flexural variable δ and rigid body mode θ. From the control point of view, the zero–dynamics addresses an important question: Is there any control input that can identically regulate y to zero? The unstable zero–dynamics given by (1.32) implies that the internal states δ, $\dot{\delta}$ will be unbounded if the initial states are different from zero. This will require an unbounded input from (1.31) which is not desirable. However, relaxing the control goal of identically zeroing the output, it is possible to have sufficiently small bounded output while the internal states are bounded, even when the system is nonminimum–phase.

1.6 Contributions and Accomplishments of this Dissertation

This thesis focuses on three main steps in engineering practice: Theoretical development, software simulation, and practical implementation. Here we are specifically dealing with the trajectory tracking control of flexible multi–link manipulators and are interested in achieving sufficiently small tip–position tracking errors while maintaining closed–loop system stability.

The control problem is considered to be a difficult one for several reasons: The non–minimum phase characteristic of the plant, the nonlinear dynamics of the manipulator, and the ill–conditioned dynamics that results from the time–scale separation of rigid and flexible modes. It is now more than a decade that several researchers have worked on different aspects of the control and design of such manipulators. In this respect, the contributions of this research can be summarized as follows:

1. Tracking Control Using Integral Manifolds

Development of a nonlinear control strategy is considered for approximate tip–position tracking of a class of flexible multi–link manipulators based on the concept of integral manifolds and singular perturbation theory. The development is along the lines stated in [42], [43] which is applicable to the linear dynamics of a single–link flexible arm. Our development is based on the more appropriate *nonlinear* framework, and is applicable to a class of multi–link flexible manipulators. The results are stated in Theorem 2.1 which furnishes the conditions under which small tracking errors and closed–loop system stability are guaranteed. From a practical point of view, a major advantage of the proposed strategy is that the only measurements required are the tip positions, joint positions, and joint velocities. This topic is addressed in Chapter 2 and has appeared in [70].

2. Tracking Control by Output Redefinition and Input–Output Decoupling

Decoupling control is essentially based on the developments described in [18] and [19]. Its application to flexible–link manipulators has appeared in [79] and [38]. To ensure that the internal dynamics remain bounded, we have modified both the controlled outputs and the control inputs such that boundedness of the internal dynamics is guaranteed. The results are summarized in Theorem 3.1 which indicates the conditions for achieving closed–loop system stability with this control strategy. Again, the control strategy is developed in a general context for a class of multi–link flexible manipulators. This topic is addressed in Chapter 3 and has appeared in [69]. The same strategy is further expanded in Chapter 5, using the concept of sliding surfaces in variable structure control. It is shown that a more robust performance is achieved in the face of considerable parametric uncertainties. The results are summarized in Theorem 5.1.

3. Observation Strategy for Flexural Rates

Many advanced control strategies require knowledge of flexible modes as well as their time derivatives (flexural rates). The flexible modes can be measured by economic sensors such as strain gauges, but the measurement of flexural rates is rather inconvenient and prone to errors. Therefore, an observer is proposed to estimate these variables. The observation scheme is proposed in a general framework and can be applied to find the flexural rates if joint positions, joint velocities, and flexible modes are available. The observation scheme is also incorporated in the control strategy outlined in item 2 above and the conditions for achieving closed–loop system stability are obtained. The results are summarized in Theorem 4.1. This topic is addressed in Chapter 4 and has appeared in [78].

4. Structure Design

Improving the plant characteristics to achieve a more well behaved system for the

purpose of control has been a usual trend in systems and control engineering practice. As an example, for the aircraft to be open–loop stable, the center of mass has to be ahead of the center of pressure. Thus, one aspect of aircraft design is to achieve such a condition. The same philosophy can be applied to flexible structure robots. The design process then boils down to the solution of an optimization problem to achieve low inertia arms with high structural natural frequencies [21], [22], [82]. Although increasing the structural natural frequencies will help to improve structural properties, it is not necessarily enough to achieve a more robust control. To this end an optimization index was introduced in [71] that incorporates a measure called modal accessibility [34]. This measure indicates the ease with which the flexible modes can be accessed and can therefore improve the system performance. This topic is addressed in Chapter 6 and has appeared in [71].

5. Experimental Evaluation

To evaluate the performance of the controllers outlined in parts 1–3 above a two–link flexible manipulator was built with the first link rigid and the second link flexible. This setup has two significant features that highlight two main characteristics of flexible manipulators: Nonlinear dynamics and the non–minimum phase behavior. The instrumentation, wiring, layout design, analog signal conditioning, and interfacing with the computational engine were carried out in the first step. In the second step, the control algorithms were coded in *C*–language and tailored for execution in a real–time environment. More details on the experimental results are given in Chapters 2 and 4.

Chapter 2

Tracking Control by Integral Manifolds

In this chapter a nonlinear control strategy for tip position trajectory tracking of a class of structurally flexible multi–link manipulators is developed. Using the concept of integral manifolds and singular perturbation theory, the full–order flexible system is decomposed into *corrected slow* and *fast* subsystems. The tip position vector is similarly partitioned into corrected *slow* and *fast* outputs. To ensure an asymptotic tracking capability, the corrected *slow* subsystem is augmented by a dynamical controller in such a way that the resulting closed–loop zero dynamics are linear and asymptotically stable. The tracking problem is then *re–defined* as tracking the *slow* output and stabilizing the corrected *fast* subsystem by using *dynamic output* feedback. Consequently, it is possible to show that the tip position tracking errors converge to a residual set of $O(\varepsilon^2)$, where ε is the singular perturbation parameter. A major advantage of the proposed strategy is that the only measurements required are the tip positions, joint positions, and joint velocities. Experimental results for a single–link arm are also presented and compared with the case when the slow control is designed based on the rigid–body model of the manipulator.

2.1 Introduction

As it was discussed in Chapter 1 the control of structurally flexible manipulators is hampered by their non–minimum phase characteristic. For a causal controller, this characteristic hinders perfect asymptotic tracking of the desired tip position trajectories with bounded control inputs. In this regard, the approach based on singular perturbation theory [81], [44], is attractive due to the two–time–scale nature of the system dynamics.

In this chapter, we address the problem of tip position tracking of flexible multi–link manipulators with the same design philosophy as in [42], [43],[90] but by taking into account the nonlinear characteristics of the plant. Most of the standard singular perturbation results that are applied to flexible–link manipulators in the literature exclude high performance light–weight manipulators, since a reduced–order *rigid body* equivalence of the flexible manipulator has limited use and application. However, the integral manifold approach in [42], [43] and [45], [46] facilitates the inclusion of the effects of higher frequency flexible modes into the corrected models. The methodology proposed in this chapter is tested by simulations on a two–link flexible manipulator, and experimentally on a single–link flexible arm. The new strategy allows for smaller tip position tracking errors, and its implementation does not require any measurement of rates of change of deflection variables with time, as these variables are not generally conveniently measurable.

The organization of this chapter is as follows. In section 2.2, the concept of integral manifolds is used to decompose the dynamics of the full–order flexible system into reduced–order corrected *slow* and *fast* subsystems up to $O(\varepsilon^3)$, where ε is the singular perturbation parameter representing the elasticity of the arm. In section 2.3, the control laws for the reduced order subsystems are designed. The main objective of the control problem is to achieve asymptotic stability of the fast subsystem and guarantee the tracking of the slow subsystem outputs by using only tip positions, joint positions and velocities. Towards this end, *dynamical* output

feedback controllers are constructed for the corrected *slow* and *fast* subsystems. It is shown that in the resulting closed–loop system, the tip positions track desired reference trajectories to $O(\varepsilon^2)$. In section 2.3, simulation results are also presented for a two–link flexible manipulator. Experimental results for a single–link arm are presented in section 2.4 and compared with the case when the *slow* control is based on the rigid–body model of the manipulator. It is shown that improved tip position tracking performance is achievable by using the proposed scheme. Finally, conclusions are given in section 2.5.

2.2 Model Reduction Using Integral Manifolds

In this section, an order reduction of the dynamic equations of flexible–link manipulators is given by using the concept of integral manifolds. A composite control strategy [44] is assumed in which the controller is comprised of *slow* and *fast* terms. The integral manifolds method, in the context of composite control, has been applied to flexible–joint manipulators in [45] and [46] and to flexible–link manipulators in [42] and [43]. Such control laws are referred to as corrective control laws because the slow control component contains corrective terms added to the term designed for the rigid model. In the following, we briefly establish the singularly perturbed model of the flexible–link manipulator that is considered in the sequel.

Consider the dynamic equations of a flexible–link robotic manipulator given by ([8])

$$M(q,\delta)\begin{bmatrix}\ddot{q}\\ \ddot{\delta}\end{bmatrix}+\begin{bmatrix}f_1(q,\dot{q})\\ f_2(q,\dot{q})\end{bmatrix}+\begin{bmatrix}g_1(q,\dot{q},\delta,\dot{\delta})\\ g_2(q,\dot{q},\delta,\dot{\delta})\end{bmatrix}+\begin{bmatrix}O & O\\ O & K\end{bmatrix}\begin{bmatrix}q\\ \delta\end{bmatrix}=\begin{bmatrix}u\\ 0\end{bmatrix} \quad (2.1)$$

or equivalently

$$\ddot{q} = -H_{11}(q,\delta)(f_1(q,\dot{q})+g_1(q,\dot{q},\delta,\dot{\delta}))$$

$$
\begin{aligned}
&- H_{12}(q,\delta)(f_2(q,\dot{q}) + g_2(q,\dot{q},\delta,\dot{\delta})) - H_{12}(q,\delta)K\delta + H_{11}(q,\delta)u \\
\ddot{\delta} &= -H_{21}(q,\delta)(f_1(q,\dot{q}) + g_1(q,\dot{q},\delta,\dot{\delta})) \\
&- H_{22}(q,\delta)(f_2(q,\dot{q}) + g_2(q,\dot{q},\delta,\dot{\delta})) - H_{22}(q,\delta)K\delta + H_{21}(q,\delta)u \qquad (2.2)
\end{aligned}
$$

where $q \in \mathbf{R}^n$ is the vector of joint position variables, $\delta \in \mathbf{R}^m$ is the vector of flexible modes, f_1, f_2, g_1, and g_2 are the terms due to gravity, Coriolis, and centripetal forces, H is the inverse of the positive–definite mass matrix M such that $M_{i,j}, H_{i,j},\ i,j = 1,2$ are the submatrices corresponding to the q and δ vectors, and K is the positive definite stiffness matrix. Let us define the new state variables

$$
x_1 = q, \qquad x_2 = \dot{q}, \qquad z_1 = \frac{\delta}{\varepsilon^2}, \qquad z_2 = \frac{\dot{\delta}}{\varepsilon} \qquad (2.3)
$$

where ε is the singular perturbation parameter defined [42], [43] as

$$
\varepsilon^2 = \frac{1}{\underline{\lambda}_{min}(H_{220}K)} \qquad (2.4)
$$

In (6.4), $\underline{\lambda}_{min}(H_{220}K)$ is the lower bound of the minimum eigenvalue of the H_{22} submatrix evaluated at $\delta = 0$ (i.e. $H_{220} = H_{22}(q,0)$) over the range in which q varies. The system described by (6.2) may then be written as

$$
\begin{aligned}
\dot{x}_1 &= x_2 \\
\dot{x}_2 &= a(x_1, x_2, \varepsilon^2 z_1, \varepsilon z_2) - A(x_1, \varepsilon^2 z_1)z_1 + H_{11}(x_1, \varepsilon^2 z_1)u \qquad (2.5) \\
\varepsilon\dot{z}_1 &= z_2 \\
\varepsilon\dot{z}_2 &= b(x_1, x_2, \varepsilon^2 z_1, \varepsilon z_2) - B(x_1, \varepsilon^2 z_1)z_1 + H_{21}(x_1, \varepsilon^2 z_1)u \qquad (2.6)
\end{aligned}
$$

where $x_1, x_2 \in \mathbf{R}^n$, $z_1, z_2 \in \mathbf{R}^m$ and

$$
\begin{aligned}
a(x_1, x_2, \varepsilon^2 z_1, \varepsilon z_2) &= -H_{11}f_1 - H_{12}f_2 - H_{11}g_1 - H_{12}g_2 \\
b(x_1, x_2, \varepsilon^2 z_1, \varepsilon z_2) &= -H_{21}f_1 - H_{22}f_2 - H_{21}g_1 - H_{22}g_2 \\
A(x_1, \varepsilon^2 z_1) &= \frac{H_{12}(x_1, \varepsilon^2 z_1)K}{\underline{\lambda}_{min}(H_{220}K)} \\
B(x_1, \varepsilon^2 z_1) &= \frac{H_{22}(x_1, \varepsilon^2 z_1)K}{\underline{\lambda}_{min}(H_{220}K)} \qquad (2.7)
\end{aligned}
$$

Defining the tip positions as outputs, the output vector y is written as [79]

$$y = x_1 + \Psi\varepsilon^2 z_1 \tag{2.8}$$

where Ψ is an $n \times n$ matrix depending on the shape function used in the original model given by (6.2) (see Appendix B for further details). In this analysis it is assumed that the vibrations are in the lateral plane of each joint axis. Let $x(t,\varepsilon)$ and $z(t,\varepsilon)$ denote the solutions of (2.5)–(2.6). In the $(2n+2m)$–dimensional state space of (2.5)–(2.6), a $2n$–dimensional manifold $\mathcal{M}_\varepsilon$, depending on the scalar ε, defined by

$$\mathcal{M}_\varepsilon : \quad z = h(x,u,\varepsilon) \tag{2.9}$$

is said to be an integral manifold of (2.5)–(2.6) if given $z(t_0,\varepsilon) = h(x(t_0,\varepsilon),u,\varepsilon)$, it then follows that $z(t,\varepsilon) = h(x(t,\varepsilon),u,\varepsilon)$ for all $t \geq t_0$, where $z^T = [z_1^T \quad z_2^T]$. Substituting h from (2.9) in (2.6) leads to a partial differential equation for h that is referred to in the literature as the *manifold condition* [45], [81], [53]. However, an approximate solution may be found by a series expansion of u and h in terms of ε. The ε^2 term in (2.8) suggests that the expansions of $h(x,u,\varepsilon)$ and u are required at least up to ε^3 terms if output feedback is to be used for control. This will become obvious shortly from equation (2.23). Let us now express the control input u according to

$$u = u_s(x,\varepsilon,t) + u_f(x,z) \tag{2.10}$$

where

$$u_s = u_0 + \varepsilon u_1 + \varepsilon^2 u_2 + O(\varepsilon^3) \tag{2.11}$$

with u_0, u_1, and u_2 to be designed subsequently. It is further assumed that u_f is zero on the second order corrected slow manifold, that is, up to $O(\varepsilon^3)$. Expanding z_1 and z_2 in (2.9) as

$$\begin{aligned} z_1 &:= h_1(x,u,\varepsilon) = h_{10} + \varepsilon h_{11} + \varepsilon^2 h_{12} + O(\varepsilon^3) \\ z_2 &:= h_2(x,u,\varepsilon) = h_{20} + \varepsilon h_{21} + \varepsilon^2 h_{22} + O(\varepsilon^3) \end{aligned} \tag{2.12}$$

and substituting (2.12) in (2.6) gives

$$\varepsilon(\dot{h}_{10} + \varepsilon\dot{h}_{11} + \varepsilon^2\dot{h}_{12} + O(\varepsilon^3)) = h_{20} + \varepsilon h_{21} + \varepsilon^2 h_{22} + O(\varepsilon^3)$$

$$\varepsilon(\dot{h}_{20} + \varepsilon\dot{h}_{21} + \varepsilon^2\dot{h}_{22} + O(\varepsilon^3)) = b(x_1, x_2, \varepsilon^2(h_{10} + O(\varepsilon)), \varepsilon(h_{20} + \varepsilon h_{21} + O(\varepsilon^2)))$$

$$-B(x_1, \varepsilon^2(h_{10} + O(\varepsilon))(h_{10} + \varepsilon h_{21} + O(\varepsilon^2)) + H_{21}(x_1, \varepsilon^2(h_{10} + O(\varepsilon)) \quad (2.13)$$

Equating the terms with the same powers in ε on both sides of the above equations up to ε^3 and using (2.11) gives

$$\begin{aligned}
h_{20} &= 0 \\
h_{21} &= \dot{h}_{10} \\
h_{22} &= \dot{h}_{11} \\
h_{10} &= B^{-1}(x_1, 0)(b(x_1, 0, 0) + H_{21}(x_1, 0)u_0) \\
h_{11} &= B^{-1}(x_1, 0)H_{21}(x_1, 0)u_1 \\
h_{12} &= B^{-1}(x_1, 0)(-\dot{h}_{21} + \frac{\partial b}{\partial \delta} \mid_{\delta,\dot{\delta}=0} h_{10} + \frac{\partial b}{\partial \dot{\delta}} \mid_{\delta,\dot{\delta}=0} h_{21} \\
&- (\sum_{i=1}^{m} \frac{\partial B}{\partial \delta_i} \mid_{\delta=0} h_{10i})h_{10} + H_{21}(x_1, 0)u_2 \\
&+ (\sum_{i=1}^{m} \frac{\partial H_{21}}{\partial \delta_i} \mid_{\delta=0} h_{10i})u_0)
\end{aligned} \quad (2.14)$$

where h_{10i} is the i-th element of h_{10}. By now substituting z_1 and z_2 from (2.12) into (2.5) yields the dynamics of the *exact* slow subsystem restricted to the $\mathcal{M}_\varepsilon$ manifold [42], [43], [90], [45], [46], [53]. Keeping $O(\varepsilon^2)$ terms and assuming that the fast control u_f is inactive on the $O(\varepsilon^2)$ approximate manifold, or more precisely, the second order manifold represented by $\mathcal{M}_2 : \ z = h^0(x, u_0, 0) + \varepsilon h^1(x, u_0, u_1, \varepsilon) + O(\varepsilon^2)$, the *second order corrected slow* subsystem is obtained as

$$\begin{aligned}
\dot{x}_1 &= x_2 \\
\dot{x}_2 &= M_{110}^{-1}(u_0 + \varepsilon u_1 + \varepsilon^2 u_2 - f_1(x_1, x_2)) - \varepsilon^2 d(x_1, x_2, \dot{x}_2 \mid_{\varepsilon=0}, u_0, \dot{u}_0)
\end{aligned} \quad (2.15)$$

where $M_{110} = M_{11}(q,0)$ [1], and $d(.)$ is given by

$$d(x_1, x_2, \dot{x}_2 \mid_{\varepsilon=0}, u_0, \dot{u}_0) = H_{110}(G_{12}h_{10} + G_{11}h_{21}) + (\sum_{i=1}^{m} \frac{\partial H_{11}}{\partial \delta_i} \mid_{\delta=0} h_{10i})f_1$$
$$+(\sum_{i=1}^{m} \frac{\partial H_{12}}{\partial \delta_i} \mid_{\delta=0} h_{10i})f_2 + H_{120}(G_{22}h_{10} + G_{21}h_{21}) + (\sum_{i=1}^{m} \frac{\partial A}{\partial \delta_i} \mid_{\delta=0} h_{10i})h_{10}$$
$$-(\sum_{i=1}^{m} \frac{\partial H_{11}}{\partial \delta_i} \mid_{\delta=0} h_{10i})u_0 + H_{120}H_{220}\{-\dot{h}_{21} + \frac{\partial b}{\partial \delta} \mid_{\delta,\dot{\delta}=0} h_{10} + \frac{\partial b}{\partial \dot{\delta}} \mid_{\delta,\dot{\delta}=0} h_{21}$$
$$-(\sum_{i=1}^{m} \frac{\partial B}{\partial \delta_i} \mid_{\delta=0} h_{10i})h_{10} + ((\sum_{i=1}^{m} \frac{\partial H_{21}}{\partial \delta_i} \mid_{\delta=0} h_{10i})u_0\} \quad (2.16)$$

with the G_{ij}, $i,j = 1,2$ matrices in (2.16) defined as

$$G_{11}(x_1,x_2) = \frac{\partial g_1}{\partial \dot{\delta}} \mid_{\delta,\dot{\delta}=0} \qquad G_{21}(x_1,x_2) = \frac{\partial g_2}{\partial \dot{\delta}} \mid_{\delta,\dot{\delta}=0}$$
$$G_{12}(x_1,x_2) = \frac{\partial g_1}{\partial \dot{\delta}} \mid_{\delta,\dot{\delta}=0} \qquad G_{22}(x_1,x_2) = \frac{\partial g_2}{\partial \dot{\delta}} \mid_{\delta,\dot{\delta}=0} \quad (2.17)$$

It should be pointed out that in the calculation of $\dot{h}_{10}$ and $\ddot{h}_{10}$ whenever $\dot{x}_1$ and $\dot{x}_2$ are required they are obtained from the controlled *rigid* model (i.e. at $\varepsilon \equiv 0$) given by

$$\begin{aligned} \dot{x}_1 &= x_2 \\ \dot{x}_2 &= a(x_1,x_2,0,0) - A(x_1,0)h_{10} + H_{11}(x_1,0)u_0 \end{aligned} \quad (2.18)$$

The exact fast variable z will deviate from the second order manifold $\mathcal{M}_2$. Representing this deviation by $\tilde{z}_1$, $\tilde{z}_2$ according to

$$\begin{aligned} \tilde{z}_1 &= z_1 - (h_{10} + \varepsilon h_{11} + \varepsilon^2 h_{12}) \\ \tilde{z}_2 &= z_2 - (h_{20} + \varepsilon h_{21} + \varepsilon^2 h_{22}) \end{aligned} \quad (2.19)$$

and substituting (2.19) in (2.6) results in the *exact fast* subsystem described by

$$\varepsilon \dot{\tilde{z}}_1 = \tilde{z}_2 - \varepsilon^3 \dot{h}_{12}$$

[1] In general $M_{ij0} = M_{ij}(q,0)$ and $H_{ij0} = H_{ij}(q,0)$ for $i = 1,2$, $j = 1,2$.

$$\begin{aligned}\varepsilon\dot{\tilde{z}}_2 &= -(B(x_1,0)+\varepsilon^2\sum_{i=1}^{m}\frac{\partial B}{\partial\delta_i}\,|_{\delta=0}\,h_{10i})\tilde{z}_1 \\ &+ (H_{210}+\varepsilon^2\sum_{i=1}^{m}\frac{\partial H_{21}}{\partial\delta_i}\,|_{\delta=0}\,h_{10i})u_f+O(\varepsilon^3) \qquad (2.20)\end{aligned}$$

By neglecting the $O(\varepsilon^3)$ terms, the *corrected fast* subsystem is now governed by

$$\begin{aligned}\varepsilon\dot{\tilde{z}}_1 &= \tilde{z}_2 \\ \varepsilon\dot{\tilde{z}}_2 &= -(B(x_1,0)+\varepsilon^2\sum_{i=1}^{m}\frac{\partial B}{\partial\delta_i}\,|_{\delta=0}\,h_{10i})\tilde{z}_1 \\ &+ (H_{210}+\varepsilon^2\sum_{i=1}^{m}\frac{\partial H_{21}}{\partial\delta_i}\,|_{\delta=0}\,h_{10i})u_f \qquad (2.21)\end{aligned}$$

Our aim is to use output feedback to stabilize the fast subsystem (2.21) so that the second order manifold is an attractive set. To this end, let us consider y from (2.8) when z_1 is defined from (2.19). This defines the actual output *restricted* to $O(\varepsilon^3)$ manifold by

$$y_{res} = x_1 + \varepsilon^2\Psi(\tilde{z}_1 + h_{10}) \qquad (2.22)$$

Thus, we may now define the *slow* and *fast* outputs y_s and y_f, respectively according to

$$\begin{aligned}y_s : &= x_1 + \varepsilon^2\Psi h_{10} \\ y_f : &= \varepsilon^2\Psi\tilde{z}_1 \qquad (2.23)\end{aligned}$$

so that $y_{res} = y_s + y_f$. Note that y_s can be obtained from measurements of the joint variables (positions and velocities). If the total tip deflection y is measured, then y_f can be constructed formally from $y_f = y - y_s$. Thus, if $y - y_s$ is used to obtain y_f, there will always be an $O(\varepsilon^3)$ error term due to the neglected unmodeled terms.

2.3 Slow and Fast Subsystem Control Strategies

In this section, we will develop control strategies based on output feedback for the corrected slow and fast subsystems described by (2.15) and (2.21), respectively. The outputs of the subsystems are given by (2.23).

Slow Subsystem Control Strategy

Consider the input–output representation of the second order corrected slow subsystem described by (2.15) with output given by y_s in (2.23), i.e.,

$$\begin{aligned} \ddot{y}_s &= M_{110}^{-1}(u_0 + \varepsilon u_1 + \varepsilon^2 u_2 - f_1(x_1, x_2)) \\ &- \varepsilon^2 d(x_1, x_2, \dot{x}_2 \mid_{\varepsilon=0}, u_0, \dot{u}_0) + \varepsilon^2 \Psi \ddot{h}_{10} \end{aligned} \tag{2.24}$$

The objective, as proposed in [42], [30], [90] is to design the control terms u_0, u_1 and u_2 such that the resulting closed–loop system has asymptotically stable zero dynamics. Towards this end, taking

$$\begin{aligned} u_0 &= M_{110} v_0 + f_1(x_1, x_2) \\ u_1 &= M_{110} v_1 \\ u_2 &= M_{110}(v_2 + d(x_1, x_2, \dot{x}_2 \mid_{\varepsilon=0}, u_0, \dot{u}_0) - \Psi \ddot{h}_{10}) \end{aligned} \tag{2.25}$$

will render (2.24) into

$$\ddot{y}_s = v_0 + \varepsilon v_1 + \varepsilon^2 v_2 \tag{2.26}$$

where v_0, v_1, and v_2 are new inputs to be defined subsequently. Note that with the above choice of control laws, h_{10}, h_{11}, and h_{12} are now expressed in terms of v_0, v_1, and v_2, respectively. Now let us choose

$$\begin{aligned} v_1 &= A_1 \dot{v}_0 \\ v_2 &= A_2 \ddot{v}_0 \end{aligned} \tag{2.27}$$

which when substituted in (2.26) yield

$$\ddot{y}_s = v_0 + \varepsilon A_1 \dot{v}_0 + \varepsilon^2 A_2 \ddot{v}_0 := v_s \tag{2.28}$$

This is the new representation of the corrected slow subsystem with its zero dynamics given by

$$\dot{v} = A_v v \tag{2.29}$$

where $v^T = [v_0^T \;\; v_1^T]$, and

$$A_v = \begin{bmatrix} 0 & A_1^{-1} \\ -\frac{A_1 A_2^{-1}}{\epsilon^2} & -\frac{A_1 A_2^{-1}}{\epsilon} \end{bmatrix} \tag{2.30}$$

The matrices A_1 and A_2 are chosen such that the zero–dynamics are asymptotically stable. This can always be guaranteed, for instance by taking $A_1 = I$ and A_2 any positive definite matrix. The tracking objective for system (2.28) is now stated as follows: Design the control law v_s such that the resulting closed–loop output y_s and its higher order derivatives follow prescribed desired trajectories.

Let v_s in (2.28) be defined as

$$v_s = \ddot{y}_r - K_d(\dot{y}_s - \dot{y}_r) - K_p(y_s - y_r) \tag{2.31}$$

where y_r, $\dot{y}_r$, and $\ddot{y}_r$ define the reference trajectory to be tracked, and further define the tracking error signals by

$$e_1 = y_s - y_r, \quad e_2 = \dot{y}_s - \dot{y}_r, \quad e^T = [e_1^T \;\; e_2^T] \tag{2.32}$$

The error dynamics are now given by

$$\dot{e} = A_e e \tag{2.33}$$

where

$$A_e = \begin{bmatrix} 0 & I \\ -K_p & -K_d \end{bmatrix} \tag{2.34}$$

Substituting (2.31) into (2.28) and using (2.30) and (2.32) yields

$$\dot{v} = A_v v + b_v(\ddot{y}_r, e, \varepsilon) \tag{2.35}$$

where

$$b_v(\ddot{y}_r, e, \varepsilon) = \begin{bmatrix} 0 \\ \frac{A_1 A_2^{-1}}{\epsilon^2}(\ddot{y}_r - K_d e_2 - K_p e_1) \end{bmatrix} \tag{2.36}$$

A block diagram of the *corrected slow* subsystem control strategy is shown in Figure 2.1.

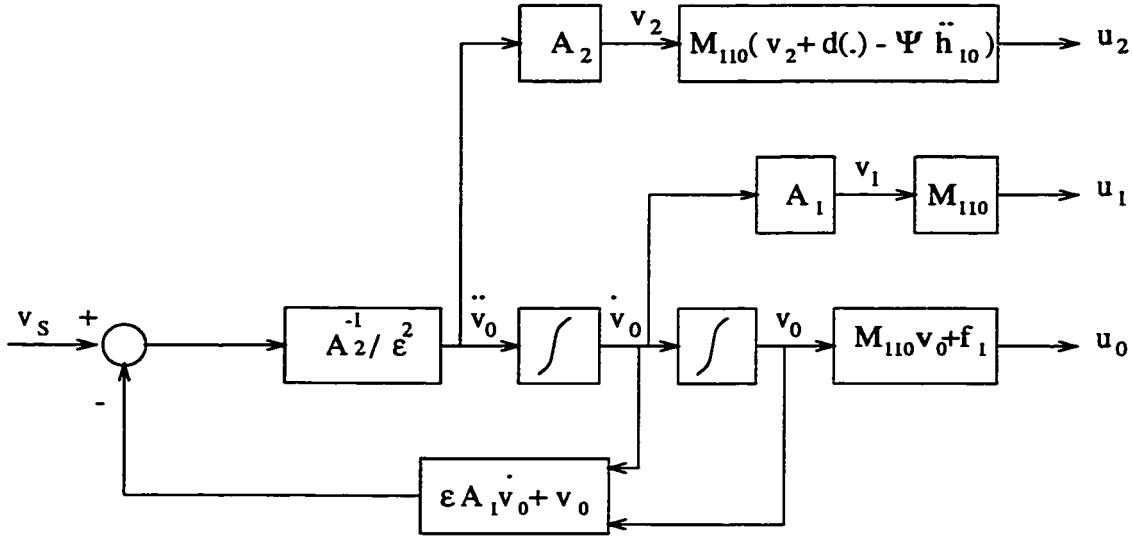

Figure 2.1: Block diagram of the *corrected slow* subsystem control strategy.

Fast Subsystem Control Strategy

Consider the corrected fast dynamics (2.21) with the fast output y_f defined by (2.23). We are interested in using dynamic output feedback to stabilize the fast dynamics. To this end, (2.21) is written in the form

$$\varepsilon\dot{\tilde{z}} = A_f(x_1, x_2, \varepsilon^2, v_0)\tilde{z} + B_f(x_1, x_2, \varepsilon^2, v_0)u_f \tag{2.37}$$

where $\tilde{z}^T = [\tilde{z}_1^T \quad \tilde{z}_2^T]$ and

$$\begin{aligned} A_f(\cdot) &= A_{f0} + \varepsilon^2 A_{f1}(x_1, x_2, v_0) \\ &:= \begin{bmatrix} 0 & I \\ -B(x_1, 0) & 0 \end{bmatrix} + \varepsilon^2 \begin{bmatrix} 0 & 0 \\ -\sum_{i=1}^{m} \frac{\partial B}{\partial \delta_i} |_{\delta=0}\, h_{10i} & 0 \end{bmatrix} \\ B_f(.) &= B_{f0} + \varepsilon^2 B_{f1}(x_1, x_2, v_0) \\ &:= \begin{bmatrix} 0 \\ -H_{210} \end{bmatrix} + \varepsilon^2 \begin{bmatrix} 0 \\ \sum_{i=1}^{m} \frac{\partial H_{21}}{\partial \delta_i} |_{\delta=0}\, h_{10i} \end{bmatrix} \end{aligned} \tag{2.38}$$

The output y_f may also be written as

$$y_f = C_f\tilde{z} \tag{2.39}$$

where the $n \times 2m$ output matrix C_f is given by

$$C_f = [\varepsilon^2 \Psi \;\; 0] \tag{2.40}$$

Since the slow variables are treated as *frozen parameters* [81] in (2.37), the above system is *linear* in terms of $\tilde{z}$. Considering the $O(1)$ terms in $A_f(\cdot)$ and $B_f(\cdot)$ in (2.38), the general configuration for the dynamic output feedback controller is proposed as

$$\varepsilon \dot{w} = F(x_1)w + G(x_1)y_f \tag{2.41}$$

$$u_f = M(x_1)w + N(x_1)y_f \tag{2.42}$$

where $w \in \mathbf{R}^l$, and matrices $F(x_1)$ $(l \times l)$, $G(x_1)$ $(l \times n)$, $M(x_1)$ $(n \times l)$, and $N(x_1)$ $(n \times n)$ are to be selected so that the resulting closed–loop corrected fast subsystem is asymptotically stable. In order to have a controller which is robust to higher order unmodeled dynamics and measurement noise, there should be no feed–through of the output in the control law (i.e., $N(x_1) \equiv 0$) [47]. Thus, augmenting the fast dynamics (2.37) with (2.41) and using the control law (2.42) yields the closed–loop corrected fast subsystem

$$\varepsilon \dot{\eta} = (A_\eta(x_1) + \varepsilon^2 A_{\eta\varepsilon^2}(x_1, x_2, v_0))\eta \tag{2.43}$$

where

$$\begin{aligned} \eta^T &= [\tilde{z}^T \;\; w^T] \\ A_\eta(x_1) &= \begin{bmatrix} A_{f0}(x_1) & B_{f0}(x_1)M(x_1) \\ G(x_1) & F(x_1) \end{bmatrix} \\ A_{\eta\varepsilon^2}(x_1, x_2, v_0) &= \begin{bmatrix} A_{f1}(x_1, x_2, v_0) & B_{f1}(x_1, x_2, v_0)M(x_1) \\ 0 & 0 \end{bmatrix} \end{aligned} \tag{2.44}$$

and which by design is guaranteed to be asymptotically stable.

A stability analysis for the full–order system is performed by considering the open–loop system (2.5)–(2.6) and the control laws (2.10), (2.11), (2.25), (2.35),

(2.41), and (2.42), and by relaxing the *frozen parameter* assumption in treating the corrected fast subsystem. This analysis is now summarized in the following theorem:

Theorem 2.1 *Let the control laws (2.10), (2.11), (2.25), (2.35), (2.41), and (2.42) be applied to the open–loop nonlinear system (2.5)-(2.6). Assuming that the desired reference trajectories and their time derivatives (at least up to order 2) are continuous and bounded, it then follows that the trajectories of* e, η, *and* $\varepsilon^2 v$ *converge to a residual set of order* $O(\varepsilon^2)$ *if the perturbation parameter* ε *belongs to the interval* $(0, \varepsilon_{max})$ *with* ε_{max} *obtained from matrix* Λ *in (A.11), and further, provided that certain norm conditions on the vectors* b_e, b_v, b_η, *the matrices* A_e, A_v, A_η, $F(x_1)$, $G(x_1)$, *and* $M(x_1)$ *defined by (A.7)–(A.9) are satisfied.*

Proof: The above result is proved in Appendix A.1 by utilizing a Lyapunov stability analysis.

Remark 1

Using the above theorem, it can also be shown that the tip position and velocity tracking errors are $O(\varepsilon^2)$. To show this, consider for example $y - y_r$. From (2.8) and (2.12), it follows that $y = x_1 + \Psi\varepsilon^2 h_{10} + O(\varepsilon^3)$, which from (2.23) may be written as $y = y_s + O(\varepsilon^3)$. Consequently, as shown in the theorem, since $y_s \to y_r + O(\varepsilon^2)$, it then follows that $y \to y_r + O(\varepsilon^2)$. A similar result also holds for $\dot{y}$, that is, $\dot{y} \to \dot{y}_r + O(\varepsilon^2)$.

Remark 2 (Robustness considerations)

The significance of the stability analysis presented in Appendix A.1 is that it can provide the designer with guidelines for selecting controller gain matrices for a more robust design. Towards this end, consider the elements of the matrix Λ that are affected by the control gain matrices K_p, K_d, A_1, A_2, $M(x_1)$, $F(x_1)$, and $G(x_1)$. In

general, to ensure better robustness, the off–diagonal terms in Λ should be decreased and the diagonal terms should be increased. A closer inspection of Λ reveals that decreasing $\gamma_{pd}\|P_v\|$, $\gamma_E\|P_e\|$, and $2\gamma_\eta\|P_\eta\| + l_3$ fulfills the aforementioned goal. It can also be concluded from these terms that choosing the gain matrices to reduce the norms $\|P_\eta\|$, $\|\partial P_\eta(x_1)/\partial x_1\|$, $\|A_1 A_2^{-1}[K_p \;\; K_d]\|$, $\|P_v\|$, $\|M(x_1)\|$, and $\|P_e\|$ will generally result in a more robust closed–loop system. Of these terms, the matrix $M(x_1)$ was found experimentally to have a significant effect on robustness. This may be attributed to the fact that it affects the γ_E term (see (A.8)) which in turn appears as an $O(1)$ off–diagonal term in Λ.

Numerical Simulations: A Two–Link Flexible Manipulator

A two–link planar manipulator is considered in which the first link is rigid and the second link is flexible. The main reasons for investigating this system are that it contains strong nonlinear coupling terms in addition to being non–minimum phase. The two–link data are as follows

$$l_1 = 0.2,\ l_2 = 0.6m,\ a_1 = 1.3cm \times 3.0,\ a_2 = 0.88mm \times 5.0cm$$
$$\rho = 7980kg/m^3\ (Steel),\ M_1 = 1kg,\ M_2 = 0.25kg,\ \varepsilon = 0.03$$
$$E = 190 \times 10^9 N/m^2, J_1 = J_2 = 0.002, J_h = 3 \times 10^{-5} kgm^2$$

where l_1 (l_2), a_1 (a_2), M_1 (M_2), J_h (J_1, J_2), ρ and E denote link lengths, cross sectional areas, masses at the end points of each link, mass moments of inertia (hub, second joint, load), mass density, and Young's modulus of elasticity, respectively.

The first two flexible modes of this system when linearized around zero joint angles are 5.6 and 27.6 Hz. The roots corresponding to the linearized zero dynamics (when the tip position is taken as the output) are at $\pm j76.9$ and ± 16.0. The slow control components of u_2 (e.g. $d(\cdot)$) were obtained by $MAPLE$. The matrices $F(x_1)$, $G(x_1)$, and $M(x_1)$ are obtained to place the poles of $A_\eta(x_1)$ in the left–half of the complex plane. This is achieved by obtaining the two gain matrices $K(x_1)$ and $L(x_1)$ as follows: The matrix $K(x_1)$ is obtained by solving a pole placement

problem for the pair $(A_{f0}(x_1), B_{f0}(x_1))$ with a prescribed set of pole locations P_{K_d} selected to be in the left–half of the complex plane. Similarly, the matrix $L(x_1)$ is obtained by placing the poles of the pair $(A_{f0}^T(x_1), C_f^T)$ to be at a prescribed set of pole locations P_{L_d} selected to be in the left–half of the complex plane. This is equivalent to solving the stabilization problem of the triple $(A_{f0}(x_1), B_{f0}(x_1), C_f)$ using a Luenberger observer.

The stabilization of $A_\eta(x_1)$ is achieved by dividing the workspace trajectory into ten segments and solving a dynamic pole placement problem for each segment such that the eigenvalues of $A_\eta(x_1)$ are at prescribed locations in the left–half of the complex plane. The gain matrices $F(x_1)$, $G(x_1)$, and $M(x_1)$ were then obtained by linear interpolation. In this way, the maximum real part of the eigenvalues of $A_\eta(x_1)$ is ensured to be negative when x_1 (second joint position variable) lies in the region of interest. It should pointed out that the use of state dependent gain matrices $F(x_1)$, $G(x_1)$, and $M(x_1)$ does not, in general, guarantee stability of the closed–loop system and further interconnection conditions (see (A.7)–(A.9) in Appendix A.1) should be satisfied.

A qualitative measure that is observed from the Lyapunov stability analysis (cf. Remark 2 in section 3) is utilized to improve the robustness of the closed–loop system. Specifically, lowering the norm of the matrix $M(x_1)$ was found to have a significant effect on the stability condition. Thus, to decrease this norm, the first row of this matrix was set to zero (which is equivalent to de–activating the fast control term for the first–link actuator). This is justified by noting that the first actuator has a lower accessibility to the vibrational modes of the second link and is likely to destabilize the closed–loop system because of higher gain requirements. The roots of the linearized zero–dynamics are located at ± 22.51 and ± 64.70, and the other gain matrices are: $A_1 = A_2 = 5I_{2\times 2}$, $K_p = I_{2\times 2}$, $K_d = 2I_{2\times 2}$.

The simulation results for quintic reference trajectories are shown in Figure 2.2. It is observed that the tracking errors $y_{1r} - y_1$ and $y_{2r} - y_2$ are both of order

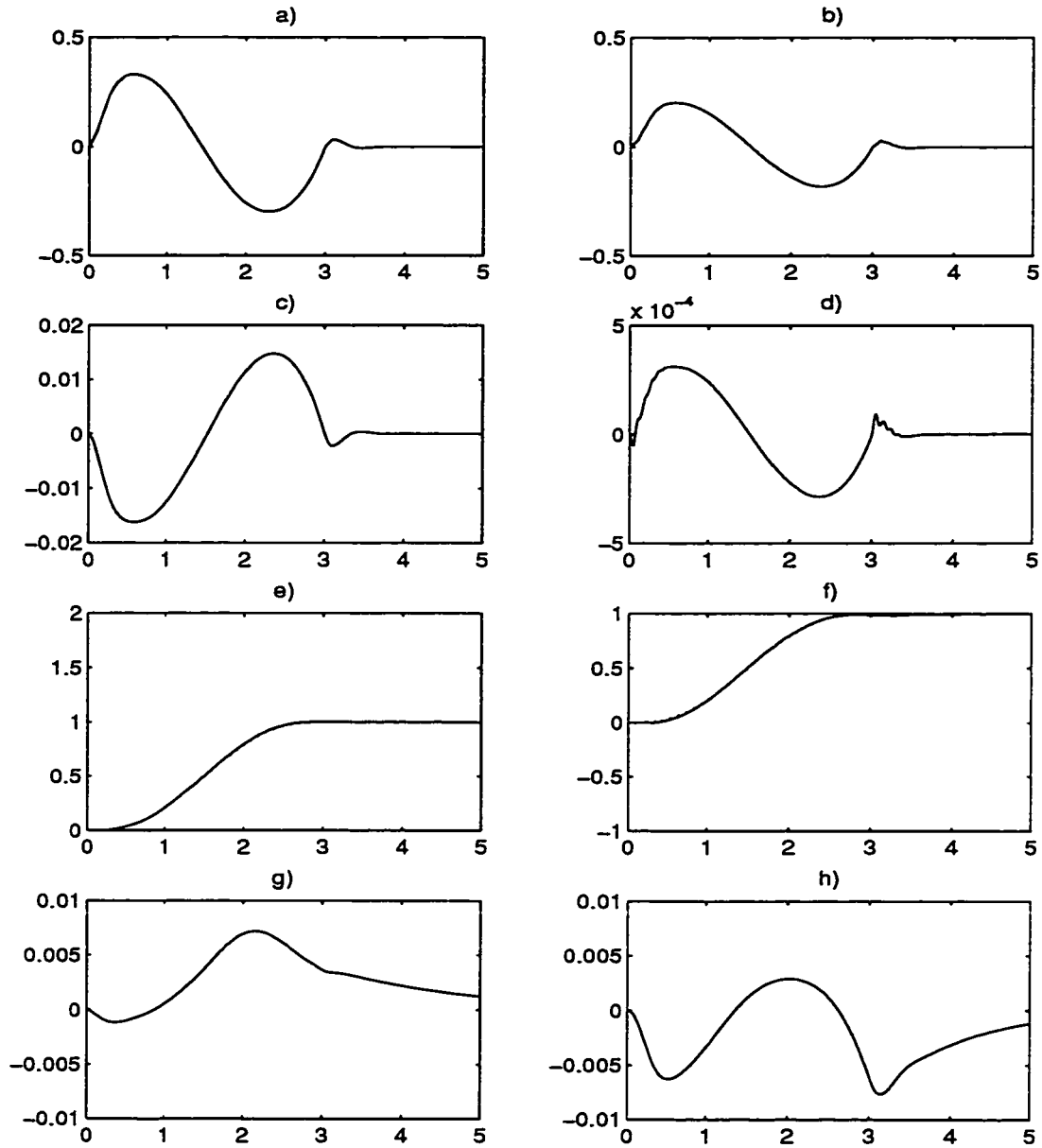

Figure 2.2: Simulation results for a flexible two–link manipulator using the proposed corrected controller (Horizontal axis: time (s)): a) First joint torque input (Nm) b) Second joint torque input (Nm) c) First flexible mode (m) d) Second flexible mode (m) e) First joint angle (—) and reference trajectory (···) (rad) f) Tip position of second link (—) and reference trajectory (···) (rad) g) Tracking error of the first link joint position, $y_{1r} - y_1$ (rad) h) Tip position tracking error of the second link, $y_{2r} - y_2$ (rad).

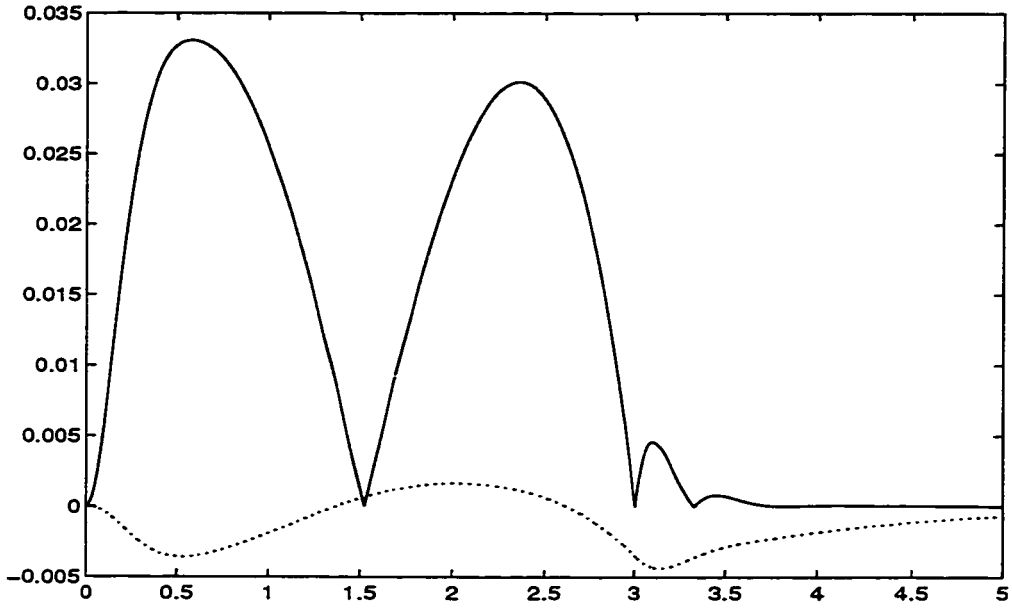

Figure 2.3: Simulation results for the proposed corrected control scheme: Maximum a bsolute value of the arm deflection (—) at each instant computed among twenty equidistant points on the second link, and tip deflection tracking error, $l_2(y_{2r} - y_2)$ $(\cdots)$ (m).

$O(\varepsilon^2)$ as expected (recall that $\varepsilon = 0.03$). The magnitude of the fast control u_f is relatively small compared to the slow control u_s, that is of the same order of magnitude as the control required for rigid–body motion. The maximum deflection of the arm is plotted in Figure 2.3 together with the tip deflection error at each instant of time.

A comparison of the performance of the proposed controller with other methods in the literature can be made by choosing the composite controller to consist of a *slow* control law that is designed based on the *rigid body* model (e.g. [8], [49]) and a fast control law that is identical to the one used in the proposed controller. Specifically, the slow controller u_0 in (2.25) is obtained by setting $\varepsilon = 0$ in (2.10), (2.11), and in y_s given by (2.23), and in $\ddot{y}_s$ given by (2.28) to yield

$$u_0 = M_{110}(\ddot{y}_r - K_d(x_2 - \dot{y}_r) - K_p(x_1 - y_r)) + f_1(x_1, x_2)$$

Simulation results for the same K_p and K_d as before are shown in Figure 2.4. As

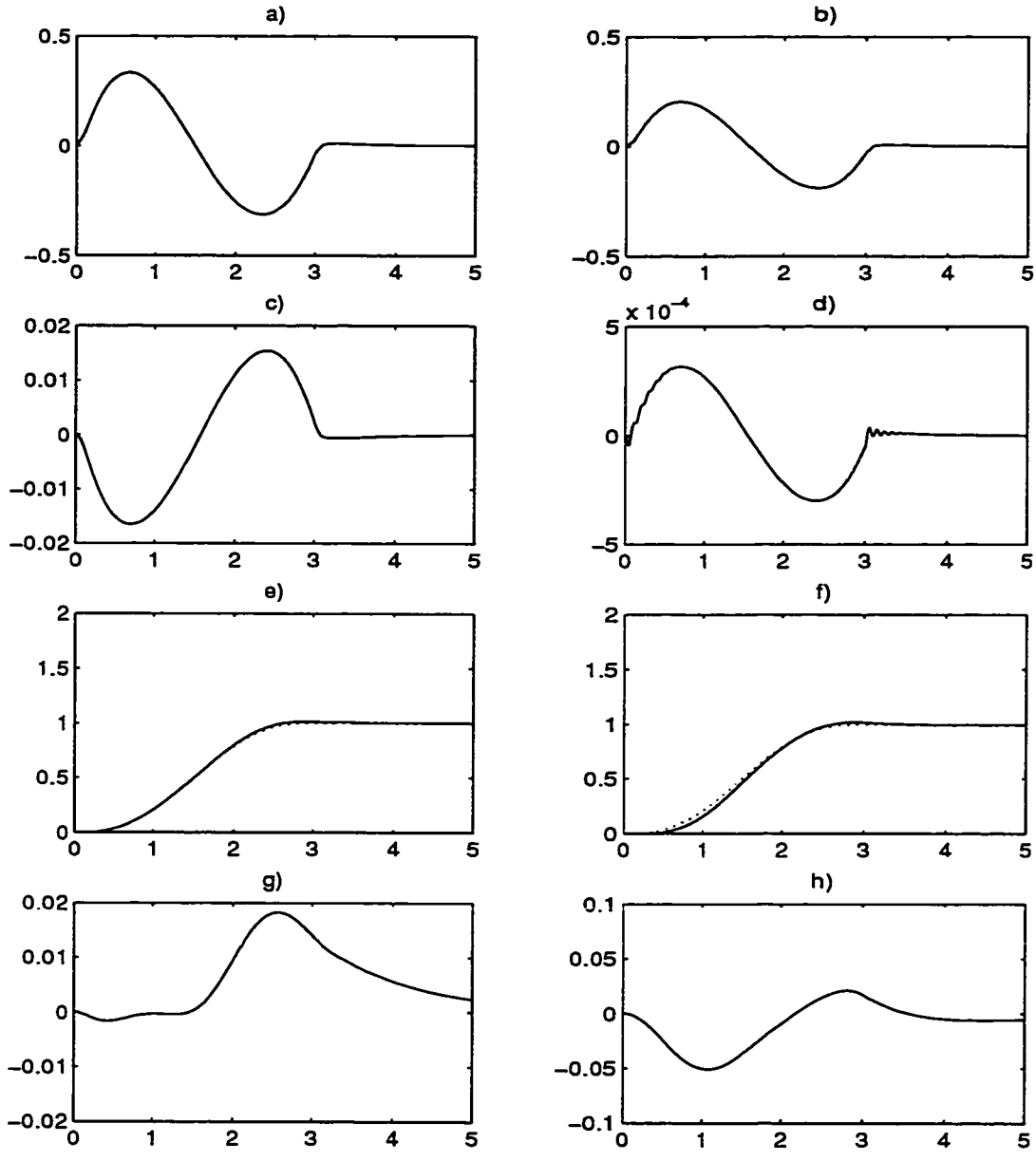

Figure 2.4: Simulation results for a *slow* control that is based on rigid–body model plus a fast control (uncorrected scheme)(Horizontal axis: time (s)): a) First joint torque input (Nm) b) Second joint torque input (Nm) c) First flexible mode (m) d) Second flexible mode (m) e) First joint angle (—) and reference trajectory $(\cdots)$ (rad) f) Tip position of second link (—) and reference trajectory $(\cdots)$ (rad) g) Tracking error of the first link joint position, $y_{1r} - y_1$ (rad) h) Tip position tracking error of the second link, $y_{2r} - y_2$ (rad).

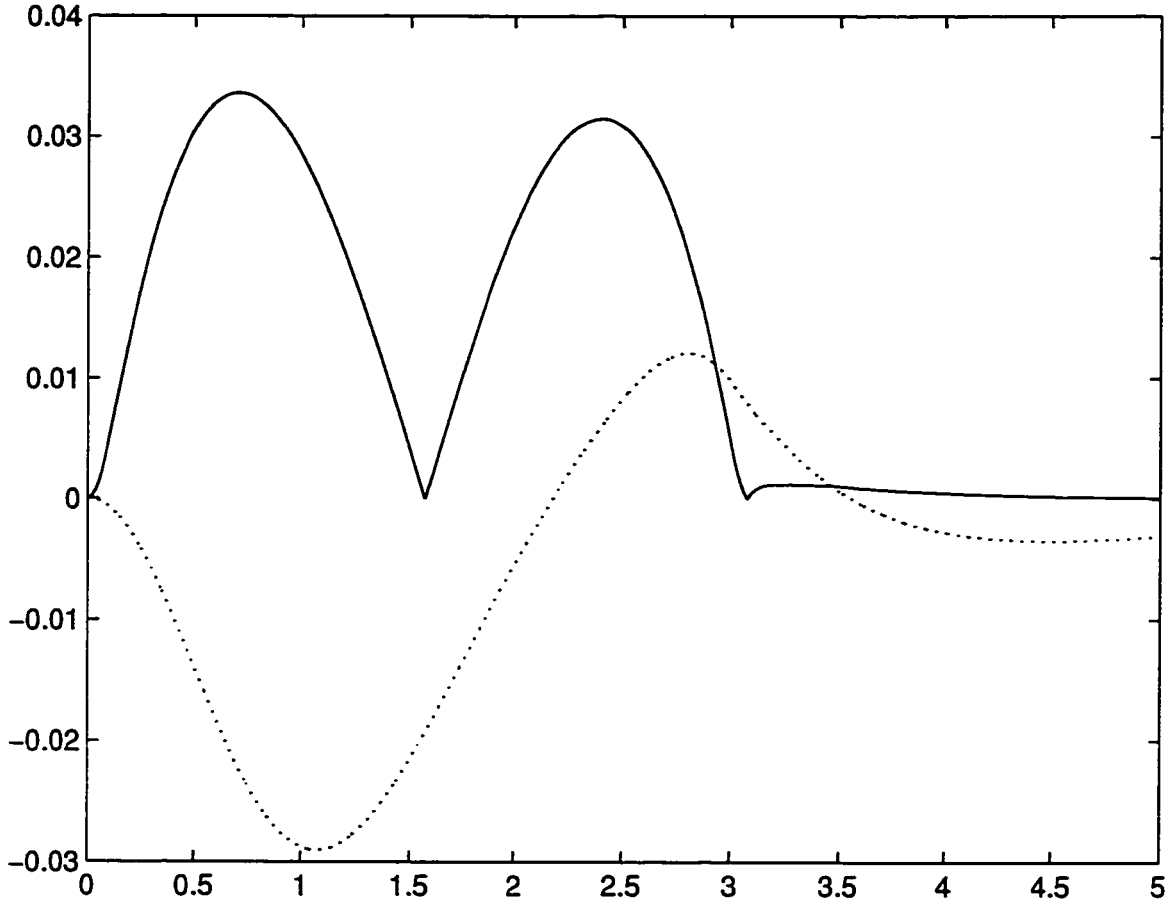

Figure 2.5: Simulation results for the scheme based on rigid–body slow control plus the fast control (uncorrected scheme): Maximum absolute value of the arm deflection (—) at each instant computed among twenty equidistant points on the second link, and tip deflection tracking error, $l_2(y_{2r} - y_2)$ $(\cdots)$ (m).

can be seen, this composite controller results in worse tracking error performance as compared to the proposed controller. The maximum deflection of the arm is plotted in Figure 2.5 together with the tip deflection error at each instant of time. The two case studies show that the proposed controller has been successful in providing a stable control action in addition to smaller tracking errors (the maximum absolute error is 7.3 times smaller as seen from Figures 2.2h and 2.4h). A quantitative measure to evaluate the tracking performance of the controllers can be defined as the ratio of maximum tip deflection error to the maximum arm deflection during the whole trajectory. For the proposed control scheme, this ratio is 0.13 (Figure 2.3) while for the rigid–body based *slow* control a ratio of 0.86 is obtained (Figure 2.5). In other words, the proposed control scheme results in an improvement of 6.6 times (0.86/0.13) in the above ratio.

2.4 Experimental Results

In this section, the practical implementation of the control strategy discussed in this chapter is investigated. Figure 2.6 shows the schematic diagram of our experimental setup. The flexible link is a stainless–steel $60cm \times 5cm \times 0.9mm$ rectangular bar with a $0.251kg$ payload attached to its end point. The mass of the bar is $0.216kg$ that is comparable to its payload. The first three measured natural frequencies are at 5.5, 20, and 45 Hz. The sensory equipment consists of three strain gauge bridges, a tachometer, and a shaft–encoder that are used to measure the flexible modes of the link, joint rate, and joint position, respectively. The signals from the strain gauge bridges and the tachometer are then amplified using low–drift amplifier stages and further passed through anti–aliasing filters. These signals are then fed into the *XVME-500/3* analog input module from *Xycom*. The actuator is a *5113 Pittman* DC brushless servomotor which is driven by a *503 Copley* PWM servo–drive amplifier.

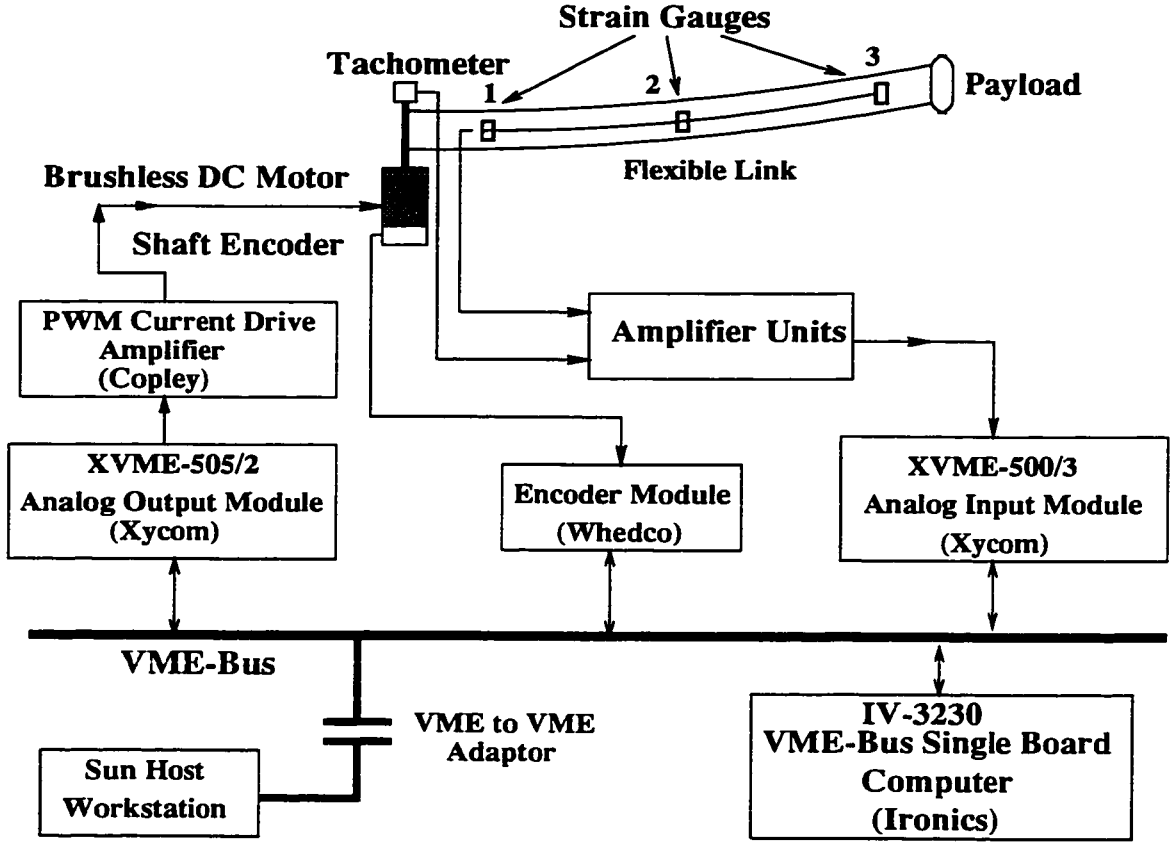

Figure 2.6: Experimental setup for the flexible arm.

The digital hardware has been selected based on the idea of a *reconfigurable* sensor–based control application. The *Chimera 3.1 Real Time Operating System* [73] is used as a local operating system in conjunction with a global *UNIX* environment. It can execute on one or more single board computers in a VMEbus–based system. In Figure 2.6, the *Chimera 3.1* kernel is running on the Ironics MC68030 processor with $33MHz$ clock frequency and a floating–point co–processor. This processor, along with the analog and digital output modules, are used for data acquisition as well as computation of the control algorithm. The code to run under *Chimera 3.1* is written in *C*.

The tip deflection is constructed based on the measurements obtained from the strain gauges. Considering a point x along the link, its deflection as a function of time can be written as

$$w(x,t) = \sum_{i=1}^{m} \phi_i(x)\delta_i(t) \tag{2.45}$$

where m is the number of flexible modes, $\phi_i(x)$ is the i-th mode shape function, and $\delta_i(t)$ is the i-th flexible mode. The longitudinal strain at point x is then obtained from

$$\epsilon(x,t) = \frac{D}{2} \frac{\frac{\partial^2 w}{\partial x^2}}{\sqrt{1 + (\frac{\partial w}{\partial x})^2}} \tag{2.46}$$

where D is the thickness of the beam at point x and the remaining term Is the reciprocal of the radius of curvature at x. An approximation to the above formula can be obtained by noting that for typical motions of the link $\partial w/\partial x$, is small. Thus

$$\epsilon(x,t) \approx \frac{D}{2} \sum_{i=1}^{m} \frac{\partial^2 \phi(x)}{\partial x^2} \delta_i(t) \tag{2.47}$$

In order to ensure a better approximation, three points on the link were selected to yield a small norm for the denominator in (2.46). By measuring the strains at the three points on the link, two deflection modes can be obtained using the Moore pseudo–inverse formula as shown in [64].

2.4.1 Model Validation

In order to evaluate the accuracy of the open–loop dynamic model of the flexible–link system, frequency responses of the link were obtained from the strain gauge outputs to the command torque input for a sufficiently small input as long as the output signals remain undistorted. The nonlinear dynamic model was derived by using the method of assumed modes as shown in Appendix C. Defining $X^T = [q\ \delta_1 \cdots \delta_m]$, where m is the number of flexible modes, and y as the vector of strain outputs, a linearized model is obtained in the following form

$$\begin{aligned} \dot{X} &= AX + bu \\ y &= CX \end{aligned} \tag{2.48}$$

where u is the command torque input and

$$A = \begin{bmatrix} O_{n\times n} & I_{n\times n} \\ -M_0^{-1}K_0 & O_{n\times n} \end{bmatrix}, \quad b = M_0^{-1}[1\ 0\ \cdots\ 0]^T$$

$$C = \begin{bmatrix} 0_{m\times 1} & C_{\delta_{m\times m}} & O_{m\times n} \end{bmatrix}, \quad K_0 = \begin{bmatrix} 0_{1\times 1} & 0_{1\times m} \\ 0_{m\times 1} & K \end{bmatrix} \tag{2.49}$$

where $n = m + 1$, $M_0 = M(q, \delta = 0)$, and $C_{\delta_{m\times m}}$ is obtained from (2.47). A sketch of the magnitudes of frequency responses obtained from this model for $m = 2$ and $m = 3$ along with the experimental results are given in Figure 2.7. It is observed that the experimental results do closely match the predicted results obtained from the model based on the assumed modes method. As the number of modes is increased from two to three, the higher frequency portions of the curve gets closer to the experimental data. Moreover, it was found that the clamped–mass shape functions resulted in a closer match than the clamped–free shape functions.

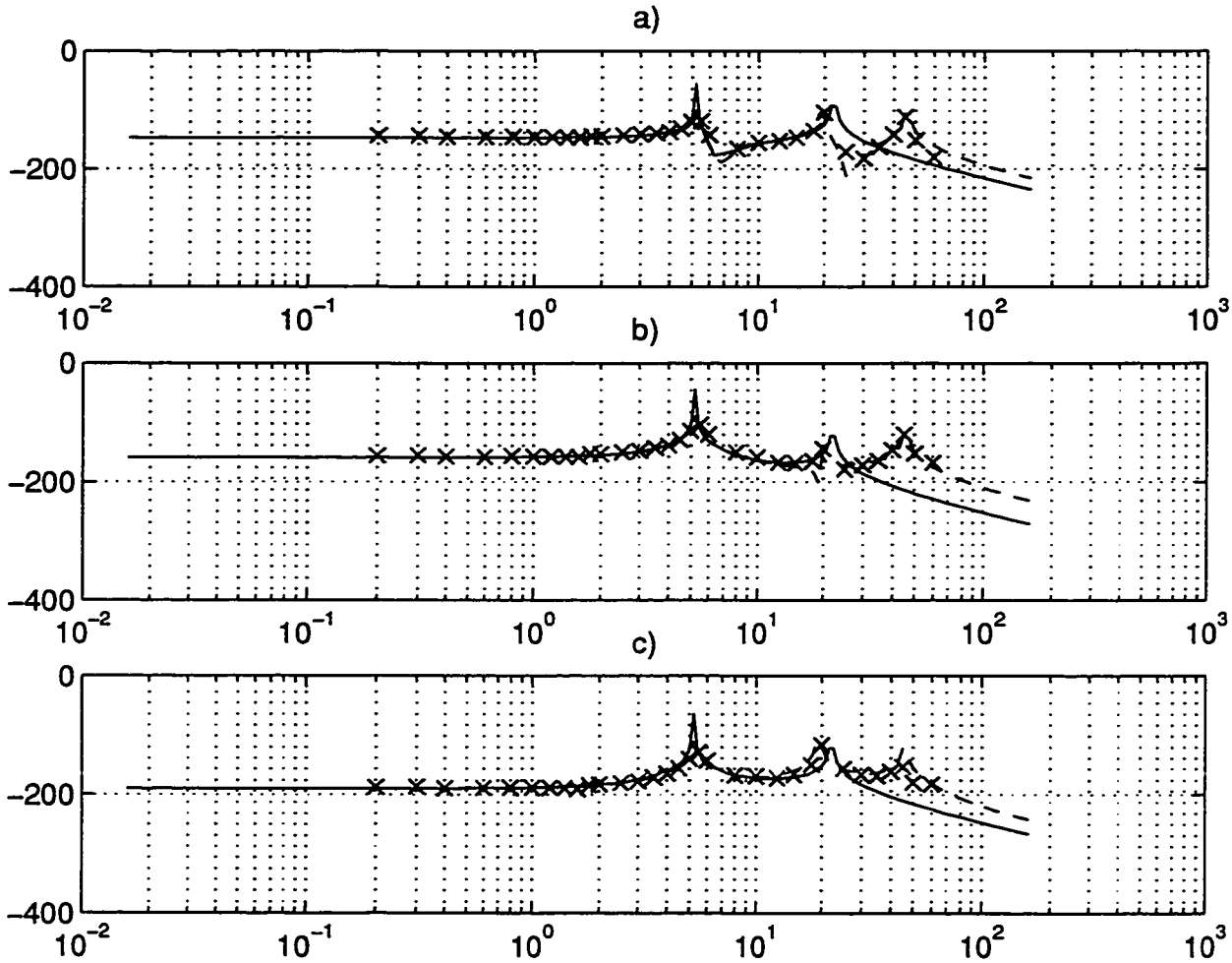

Figure 2.7: Comparison between the experimental ($\times$) and the analytical fr equency responses for two (—) and three (– –) flexible modes when the strain gauge output is taken at a) Point 1, b) Point 2, and c) Point 3. Horizontal axis: Frequency (Hz), Vertical axis: $(strain/u)$ dB .

2.4.2 Implementation of the Control Law

The terms required by the controller are based on the model given in the Appendix C and are as follows

$$d(x_1, x_2, \dot{x}_2 \mid_{\epsilon=0}, u_0, \dot{u}_0) = 3 \times 10^{-6}\dot{q}^2 v_0 - 37.23\ddot{v}_0$$

$$\bar{h}_{10} = \begin{bmatrix} -26.6512 v_0 \\ 0.0296 v_0 \end{bmatrix}, \quad h_{11} = \begin{bmatrix} -26.6482 v_1 \\ -0.2964 v_1 \end{bmatrix}$$

$$h_{12} = \begin{bmatrix} 19.9221\ddot{v}_0 - 1011.8217\dot{q}^2 v_0 - 199.7986 u_2 \\ -1.0965\ddot{v}_0 + 0.0177\dot{q}^2 v_0 - 0.2222 u_2 \end{bmatrix}$$

For the open–loop flexible–link system the roots of the linearized zero dynamics are located at ± 15.4, $\pm j72.2$. The design matrices F, G, and M are selected so that the poles of A_η, given by (2.44), are in the left–half of the complex plane. Thus, choosing $P_{K_d} = \{-0.1 \pm j4.2, -0.1 \pm j1.0\}$ and $P_{L_d} = \{-0.2 \pm j8.4, -0.2 \pm 2.0\}$, results in

$$F = \begin{bmatrix} -0.3773 & 0.3773 & 1.0000 & 0 \\ 0.4227 & -0.4227 & 0 & 1.0000 \\ -101.6687 & 20.3974 & -1.6594 & 7.3035 \\ -16.0989 & -0.7886 & -0.2861 & 1.2594 \end{bmatrix}$$

$$G = 10^4 \times [0.0133 \quad -0.0149 \quad 3.2128 \quad 0.5014]$$

and

$$M = [0.0004 \quad -0.0006 \quad 0.0019 \quad -0.0083].$$

The other data parameters for this system are given as $\epsilon = 0.03$, $K_p = 1$, $K_d = 2$, $A_1 = 2.5$, and $A_2 = 37$.

The differential equations corresponding to the dynamic control laws (2.35) and (2.41) have to be numerically solved for a digital implementation. The numerical solution has to be fast enough so that the results are computed and made available well before the end of each sampling period. The procedure adopted here is the

modified midpoint method [74]. On average, this method requires 1.5 derivative evaluations per step as compared to the Runge–Kutta's 4 evaluations. Three steps were used during each sampling period. The implemented algorithm took 2.2 msec on the MC68030 Ironics processor board. Thus, a sampling frequency of 350 Hz was used. This rate was sufficient to allow computation of the control law as well as the data acquisition and trajectory generation tasks, while maintaining closed–loop system stability.

Due to mechanical imprecisions in the physical construction of the manipulator, the arm is not completely level in the horizontal plane. This can lead to considerable errors due to the fact that the magnitude of the required torque for control is small. The problem is resolved by noting that the gravity field produces a torque about the joint axis that may be expressed by $\tau_g = a + bcos(q) + csin(q)$, where q is the joint angle and a, b and c are terms due to small offset angles. These terms are estimated by measuring the balancing torques at several joint angles and by using the least–squares algorithm. Thus, τ_g is added to the control torque to counterbalance the gravitational effects. The experimental results are shown in Figure 2.8, for the case when the proposed control strategy is applied, and in Figure 2.9, for the case when the fast control remains the same but a rigid body slow control is employed. The experimental results show improved tracking performance for the proposed method. The ratio of maximum tip position error to maximum arm deflection during the whole trajectory is found to be 0.67 for the proposed scheme and 1.39 for the slow rigid–based control method. The steady–state errors in both figures are a result of the small arm deflection that exists due to gravity effects. The maximum tip angular error of the simulated 2–link nonlinear system is about $0.005rad$ while it is $0.05rad$ for the experimental arm. It should be noted that a faster trajectory is used in the experimental case. On the other hand, it is worth emphasizing that the theoretical tracking error bound in Theorem 2.1 is derived subject to the absence of modeling imperfections, friction terms, actuator dynamics, discretization effects,

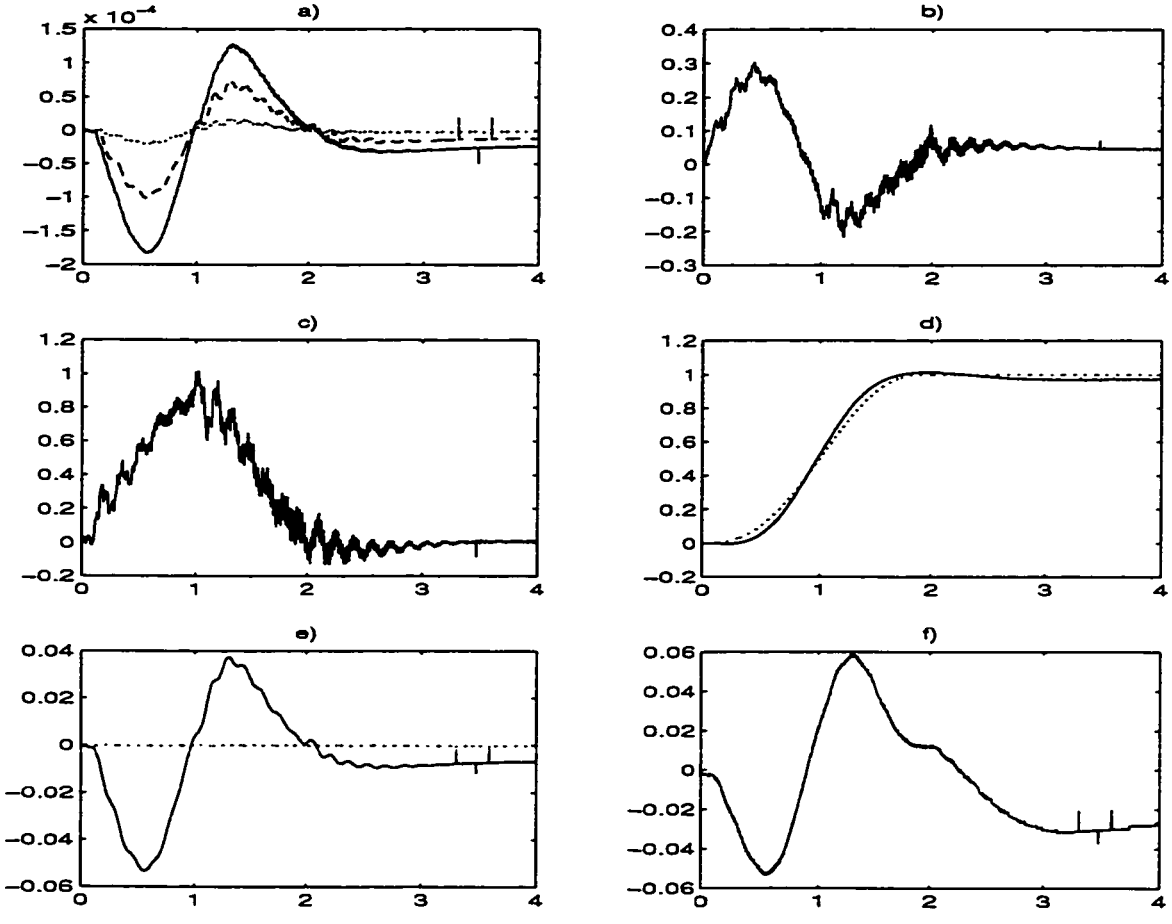

Figure 2.8: Experimental results for the proposed method: a) Strains at points 1 (—), 2 (– –), and 3 (· · ·) (m/m) b) Torque input (Nm) c) Joint velocity (rad/s) d) Tip trajectory (—) and desired tip trajectory (· · ·) (rad) e) Deflection modes δ_1 (—) and δ_2 (· · ·) (m) f) Tip position trajectory error, $y_r - y$ (rad).

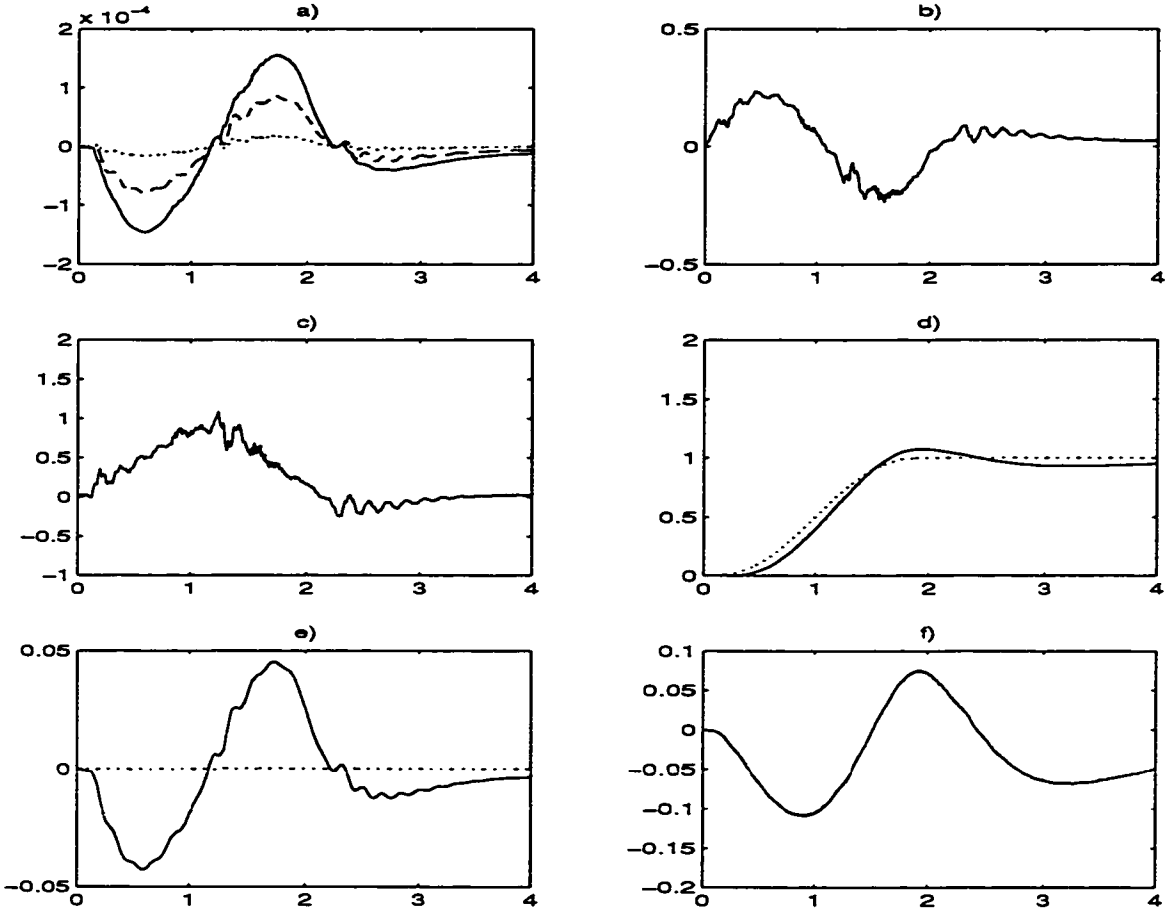

Figure 2.9: Experimental results for the slow control designed based on the rigid model plus the fast control: a) Strains at points 1 (—), 2 (– –), and 3 (· · ·) (m/m) b) Torque input (Nm) c) Joint velocity (rad/s) d) Tip trajectory (—) and desired tip trajectory (· · ·) (rad) e) Deflection modes δ_1 (—) and δ_2 (· · ·) (m) f) Tip position trajectory error, $y_r - y$ (rad).

sensor noise, higher frequency unmodeled dynamics, and computational delay of the control law. These factors are among the possible sources that contribute to the difference between the theoretical tracking error estimates and the actual tracking errors.

2.5 Conclusion

In this chapter, a control scheme was proposed for achieving greater accuracy for tip position tracking in structurally flexible robotic manipulators. Theoretical estimates show that the tracking errors converge to a residual set of $O(\varepsilon^2)$, and experimental results show that smaller tip position tracking errors are achieved compared to conventional algorithms in the literature. The only measurements required by the control law are joint positions, velocities and tip positions. This is an attractive feature from a practical implementation point of view as tip deflection rates are not directly measured, but tip positions can be readily measured by camera vision systems or strain gauge sensors. The control law is more complicated than its rigid counterpart; however the use of symbolic manipulation software and fast real–time control technology make the implementation of such a control law feasible.

Chapter 3

Decoupling Control

In this chapter we present an inverse dynamics control strategy to achieve sufficiently small tracking errors for a class of multi–link structurally flexible manipulators. This is done by defining new outputs near the end points of the arms as well as by augmenting the control inputs by terms which ensure stable operation of the closed–loop system under specific conditions. The controller is designed in a two–step process. First, a new output is defined such that the zero dynamics of the corresponding system are stable. Next, to ensure stable asymptotic tracking the control input is modified such that stable asymptotic tracking of the new output or approximate tracking of the actual output may be achieved. This is illustrated for the case of single– and two–link flexible manipulators.

3.1 Introduction

As discussed in Chapter 1, it is well known that the transfer function from the torque input to the tip position output of a single–link manipulator is, in general, non–minimum phase [36]. For a causal controller, the non–minimum phase property hinders perfect asymptotic tracking of a desired tip trajectory with a bounded

control input. Thus, for a causal controller and perfect tracking, the flexible system should be minimum phase. The minimum phase property may be achieved by output re–definition, as done in [36], [37], [38], or by a redefinition of the output into *slow* and *fast* outputs as done in the previous chapter. In [36], the reflected tip position was proposed as the output for a single–link manipulator. In [37], the region of sensor and actuator locations for achieving the minimum–phase property for a single–link manipulator was investigated using a linear transfer function of the link. In [38], a region of outputs having the minimum phase property was given for a two–link manipulator. However, the approach is restricted since it consists of numerical calculations for a specific manipulator with two flexible modes.

In this chapter, after deriving the zero dynamics of a certain class of multi–link flexible manipulators, we will develop a control strategy based on input–output linearization of the flexible–link system. Modeling uncertainties have been taken into account, and it is further assumed that the vibrations are mainly lateral vibrations about the axis of rotation. In other words, for each link it is assumed that a considerable amount of potential energy is stored in the direction of bending corresponding to the axis of rotation of that link, and that the potential energies due to deflections in other directions are negligible. This may be achieved by proper mechanical structure design. A planar manipulator with rectangular cross sections in which the height to thickness ratio of each cross section is large is an example of such a system.

The results are applied to a two–link manipulator. In particular, regions corresponding to the minimum–phase property are obtained and compared under different load and damping conditions. The control strategy is also tested on flexible single– and two–link manipulators.

3.2 Input–Output Linearization

The input–state map of flexible–link manipulators is not in general feedback linearizable [56]. However, the system is locally input–output linearizable. Input–output linearization in nonlinear systems theory is essentially based on the developments described in [18] and [19]. In order to apply this technique to flexible–link manipulators, let us first consider the dynamics of a multi–link flexible manipulator [29] with structural damping added, i.e.,

$$M \begin{bmatrix} \ddot{q} \\ \ddot{\delta} \end{bmatrix} + \begin{bmatrix} f_1(q,\dot{q}) + g_1(q,\dot{q},\delta,\dot{\delta}) + E_1\dot{q} \\ f_2(q,\dot{q}) + g_2(q,\dot{q},\delta,\dot{\delta}) + E_2\dot{\delta} + K\delta \end{bmatrix} = \begin{bmatrix} u \\ 0 \end{bmatrix} \tag{3.1}$$

where q is the $n \times 1$ vector of joint variables, δ is the $m \times 1$ vector of deflection variables, f_1, f_2, g_1, and g_2 are the terms due to gravity, Coriolis, and centripetal forces, M is the positive–definite mass matrix, E_1 and E_2 are positive–definite damping matrices, K is the positive–definite stiffness matrix, and u is the $n \times 1$ vector of input torques (clamped mode shapes have been assumed). Let us define $H(q,\delta) = M^{-1}(q,\delta) = \begin{bmatrix} H_{11} & H_{12} \\ H_{21} & H_{22} \end{bmatrix}$. Then (1) can be written in the state–space form

$$\dot{x} = f(x) + g(x)u \tag{3.2}$$

where $x^T = \begin{bmatrix} q^T & \delta^T & \dot{q}^T & \dot{\delta}^T \end{bmatrix}$,

$$f(x) = \begin{bmatrix} \dot{q} \\ \dot{\delta} \\ -H_{11}(f_1 + g_1 + E_1\dot{q}) - H_{12}(f_2 + g_2 + K\delta + E_2\dot{\delta}) \\ -H_{21}(f_1 + g_1 + E_1\dot{q}) - H_{22}(f_2 + g_2 + K\delta + E_2\dot{\delta}) \end{bmatrix},$$

$$g(x) = \begin{bmatrix} O_{(m+n)\times n} \\ H_{11}(q,\delta) \\ H_{21}(q,\delta) \end{bmatrix}.$$

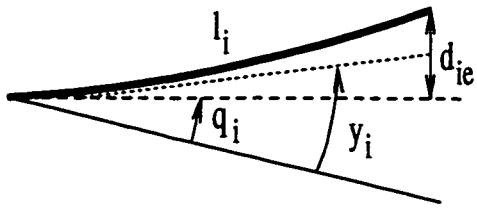

Figure 3.1: The output of link i (y_i).

Following [38], since the beam deflection is usually small with respect to link length, we have from Figure 3.1,

$$y_i = q_i + \alpha_i d_{ie}/l_i,\ i = 1, 2, \cdots, n \tag{3.3}$$

In (3.3), α_i is a variable which takes values between -1 and $+1$, with $\alpha_i = 1, 0, -1$ corresponding to tip, joint angle, and reflected tip positions respectively.

The tip deflection d_{ie} can be written as

$$d_{ie} = \sum_{j=1}^{n_i} \Phi_{ij}(l_i)\delta_{ij} \tag{3.4}$$

where Φ_{ij} is the j-th mode shape function of the i-th link and δ_{ij} is the j-th mode of the i-th link. Thus, for the output vector, we have (see also Appendix B)

$$y = q + \Psi_{n\times m}\delta \tag{3.5}$$

where

$$\begin{aligned}
\Psi_{n\times m} &= \begin{bmatrix} v_1^T & 0^T & \cdots \\ 0^T & \ddots & 0^T \\ \vdots & \vdots & \vdots \\ 0^T & 0^T & v_n^T \end{bmatrix} \\
(v_i^T &= \frac{\alpha_i}{l_i}\begin{bmatrix} \Phi_{i1}(l_i) & \cdots & \Phi_{in_i}(l_i) \end{bmatrix}, i = 1, \cdots, n) \\
y^T &= \begin{bmatrix} y_1 & \cdots & y_n \end{bmatrix} \\
\delta^T &= \begin{bmatrix} \Delta_{n_1}^T & \Delta_{n_2}^T & \cdots & \Delta_{n_n}^T \end{bmatrix}
\end{aligned} \tag{3.6}$$

with Δ_{n_i} being the vector of the deflection variables of link i, defined as

$$\Delta_{n_i}^T = \begin{bmatrix} \delta_{i1} & \cdots & \delta_{in_i} \end{bmatrix} \tag{3.7}$$

Now consider system (3.2), with the output defined by (3.5). To perform input–output linearization on this system we take time derivatives until the inputs appear. In our case, two differentiations are required, after which all inputs appear simultaneously. After some manipulations we have,

$$\ddot{y} = a(\alpha, x) + B(\alpha, q, \delta)u \tag{3.8}$$

where

$$\alpha^T = \begin{bmatrix} \alpha_1 & \cdots & \alpha_n \end{bmatrix},$$

$$B(\alpha, q, \delta) = H_{11} + \Psi_{n\times m} H_{21},$$

$$a(\alpha, x) = -(H_{11} + \Psi H_{21})(f_1 + g_1 + E_1\dot{q}) - (H_{12} + \Psi H_{22}) \times (f_2 + g_2 + K\delta + E_2\dot{\delta}). \tag{3.9}$$

Now suppose that α and q_r have been selected such that $B(\alpha, q_r, 0)$ is nonsingular (q_r denotes the desired reference trajectory to be tracked by y). Then continuity implies that, on a finite domain around $x_r^T = [q_r^T\ 0\ \dot{q}_r^T\ 0]$, taking u as

$$u = B^{-1}(\alpha, q, \delta)(v - a(\alpha, x)) \tag{3.10}$$

results in

$$\ddot{y} = v \tag{3.11}$$

which is an input–output linearized system with a new input vector v. Note that the dimension of the unobservable dynamics is $2m$. Now consider the state transformation

$$z = T(x) = D_T x \tag{3.12}$$

where $z := [z_o^T \; z_u^T]$, and

$$z_o^T = [z_{o1}^T \; z_{o2}^T]$$

$$z_u^T = [z_{u1}^T \; z_{u2}^T]$$

$$D_T = \begin{bmatrix} I_{n\times n} & \Psi_{n\times m} & O_{n\times n} & O_{n\times m} \\ O_{n\times n} & O_{n\times m} & I_{n\times n} & \Psi_{n\times m} \\ O_{m\times n} & I_{m\times m} & O_{m\times n} & O_{m\times m} \\ O_{m\times n} & O_{m\times m} & O_{m\times n} & I_{m\times m} \end{bmatrix}$$

Because of the nonsingularity of D_T, (3.12) is a global diffeomorphism, and will transform (3.2) with output given by (3.5) into

$$\begin{aligned} \dot{z}_{o1} &= z_{o2} \\ \dot{z}_{o2} &= a(\alpha, x) + B(\alpha, q, \delta)u \\ \dot{z}_u &= C(x) + D(x)u \\ y &= z_{o1} \end{aligned} \tag{3.13}$$

where $C(x)$ and $D(x)$ are matrices corresponding to $f(x)$ and $g(x)$. To find the zero dynamics, z_{o1} and z_{o2} are set identically to zero, which after some manipulations leads to an explicit relationship for the zero dynamics, i.e.

$$\begin{aligned} \dot{z}_{u1} &= z_{u2} \\ \dot{z}_{u2} &= [-H_{22} + H_{21}(H_{11} + \Psi H_{21})^{-1}(H_{12} + \Psi H_{22})] \mid_{(w_1, w_3)} \\ &\times [f_2(w_1, w_2) + g_2(w_1, w_2, w_3, w_4) + K z_{u1} + E_2 z_{u2}] \end{aligned} \tag{3.14}$$

where

$$w_1 = -\Psi z_{u1}, \; w_2 = -\Psi z_{u2}, \; w_3 = z_{u1}, \; w_4 = z_{u2} \tag{3.15}$$

Linearizing (3.14) about the equilibrium point $z_{u1}, z_{u2} = 0$ gives

$$\begin{aligned} \dot{z}_{u1} &= z_{u2} \\ \dot{z}_{u2} &= [-H_{22} + H_{21}(H_{11} + \Psi H_{21})^{-1}(H_{12} + \Psi H_{22})] \mid_{z_{u1}, z_{u2}=0} \\ &\times (K z_{u1} + E_2 z_{u2}) \end{aligned} \tag{3.16}$$

The following result is now concluded from the above discussion:

Condition for Minimum–Phase Behavior: Let the vector α, and the matrices $H(0,0), K$, and E_2 be such that the matrix

$$A(\alpha) = \begin{bmatrix} O & I \\ -P_0 K & -P_0 E_2 \end{bmatrix} \tag{3.17}$$

with P_0 given by

$$P_0 = [H_{22} - H_{21}(H_{11} + \Psi H_{21})^{-1}(H_{12} + \Psi H_{22})]_{(0,0)} \tag{3.18}$$

is a Hurwitz matrix. Then the origin of (3.16), and hence (3.14), is locally asymptotically stable, and the original nonlinear system is locally minimum phase. This result follows by noting that the eigenvalues of A are the modes of the linearized zero dynamics of the system. It is interesting to note that $\alpha = 0$ (joint position output) guarantees P_0 to be a positive definite matrix, which makes A a Hurwitz matrix. This can be shown by using the Lyapunov function candidate $V = z_{u1}^T K z_{u1} + z_{u2}^T P_0^{-1} z_{u2}$ for (3.16) and applying LaSalle's theorem.

Now suppose that, due to modeling errors and truncation of modes, we cannot exactly get u given by (3.10). Furthermore, since the damping terms E_1 and E_2 are not commonly modeled exactly, we include them in the uncertainties. Thus in the previous relations, it suffices to put $E_1 = E_2 = 0$ and account for them in the uncertainties. Let us define

$$u = \hat{B}^{-1}(\alpha, q, \delta)(v - \hat{a}(\alpha, x)) + K_\delta(q)\delta + K_{\dot{\delta}}(q)\dot{\delta} \tag{3.19}$$

where $B = \hat{B} - \Delta B$ and $a = \hat{a} - \Delta a$, with ΔB and Δa representing the uncertainties in B and a respectively [1]. Then, from (3.8) we have

$$\ddot{y} = B\hat{B}^{-1}v + (I - B\hat{B}^{-1})a - B\hat{B}^{-1}\Delta a + BK_\delta(q)\delta + BK_{\dot{\delta}}(q)\dot{\delta} \tag{3.20}$$

[1]Note that $\hat{B}$ is at our disposal. For example, it may be obtained from a model with two flexible modes while the actual plant may be described by three flexible modes.

In view of (3.13) with u given by (3.19) and choosing

$$v = \ddot{y} + K_p e + K_d \dot{e} \tag{3.21}$$

where $e = y_r - y$ (y_r is the desired trajectory for the output), yields

$$\dot{E} = A_E E + d_E(\alpha, x, , t) \tag{3.22}$$

with

$$\begin{aligned} d_E(\alpha, x, t) &= (I - B\hat{B}^{-1})(K_p e + K_d \dot{e} + \ddot{y}_r - a) + B\hat{B}\Delta a - BK_\delta(q)\delta + K_{\dot{\delta}}(q)\dot{\delta} \\ E^T &= \begin{bmatrix} e^T & \dot{e}^T \end{bmatrix} \\ A_E &= \begin{bmatrix} 0 & I \\ -K_p & -K_d \end{bmatrix} \end{aligned} \tag{3.23}$$

Similarly (3.13) can be written in terms of the new u, that is

$$\dot{\Delta} = A_\Delta(q)\Delta + \begin{bmatrix} 0 \\ G_\Delta(x,t) \end{bmatrix} \tag{3.24}$$

where

$$\begin{aligned} G_\Delta(x,t) &= H_{210}\hat{B}_0^{-1}(\ddot{y}_r + K_p e + K_d \dot{e}) + H_{210}(-\hat{B}_0^{-1}\hat{a}_0 + B_0^{-1}a_0) + O(\delta^2, q, \dot{q}) \\ A_\Delta(q) &= \begin{bmatrix} 0 & I \\ -P(q)K - H_{210}K_\delta(q) & -H_{210}K_{\dot{\delta}}(q) \end{bmatrix} \\ \Delta^T &= [\delta^T \ \dot{\delta}^T] \end{aligned} \tag{3.25}$$

and $O(\delta^2, q, \dot{q})$ indicates that the remaining terms are of order δ^2, and $H_{210} = H_{21}(q, 0)$ (the same notation is adopted for the other H_{ij} $(i, j = 1, 2)$ submatrices in the sequel). Furthermore, matrices $K_\delta(q)$ and $K_{\dot{\delta}}(q)$ are selected such that $A_\Delta(q)$ is a Hurwitz matrix for the range in which q is varied and

$$P(q) = [H_{220} - H_{210}(H_{110} + \Psi H_{210})^{-1}(H_{120} + \Psi H_{220})] \tag{3.26}$$

Noting that A_E and A_Δ are Hurwitz matrices, it may then be shown (using a Lyapunov analysis) that the trajectories of the closed–loop system given by (3.22) and (3.24) converge to a residual set with small tracking errors e and $\dot{e}$ and bounded δ and $\dot{\delta}$ provided that certain conditions are satisfied. The following theorem summarizing the above results may then be stated.

Theorem 3.1 *Let the control law (3.19) be applied to the original nonlinear system (3.1) with $\hat{B}$ nonsingular on the domain of interest, then assuming that the desired trajectories and their time derivatives (at least up to order 2) are continuous and bounded, it follows that the trajectories of E, $\epsilon_1\Delta$ (ϵ_1 is a positive number typically less than one), starting from a specific set, converge to a small residual set provided that certain norm conditions in a bounded region of the state space of E and Δ, containing the origin are satisfied.*

Proof: The above result is proved in Appendix A.2.

Remark 1: Singular B Matrix

Here we have assumed that $B(\alpha, q, \delta)$ is nonsingular. In case B is singular the decoupling method described above cannot be achieved by static state feedback. However it may still be possible to find a dynamic compensator of the form

$$\begin{aligned} \dot{z} &= d_c(x,z) + E_c(x,z)U \\ u &= f_c(x,z) + G_c(x,z)U \end{aligned} \tag{3.27}$$

with $z \in R^{n_c}$, $U \in R^n$, such that the extended system described by (3.8) and (3.27) with output given by (3.5) is decoupled from U to y. The theoretical developments for general affine nonlinear systems are given in [68]. From a practical point of view in our application, employing this method may have the drawback of requiring acceleration (or higher derivative) measurements.

Remark 2: Tip–Position Tracking Errors

In Theorem 3.1, we mention redefined output tracking errors which have been denoted by e_1 and e_2. The redefined outputs are near the tip positions. The controller

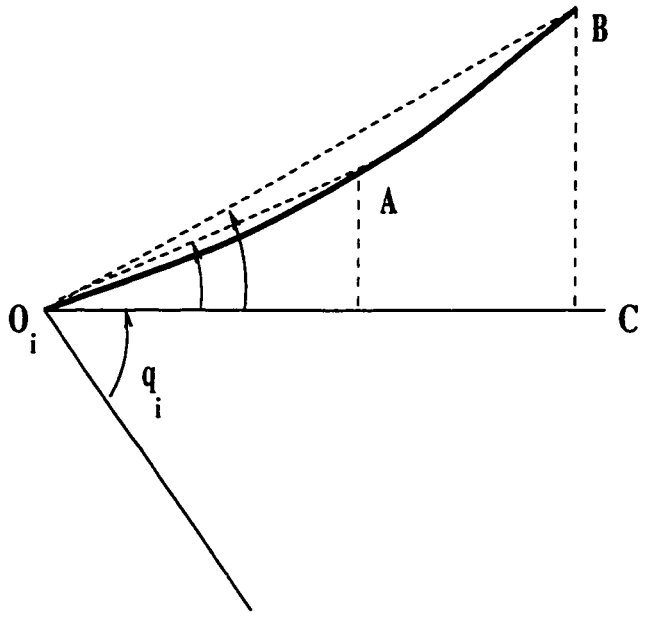

Figure 3.2: Tip position and redefined outputs of link i.

tries to achieve small tracking errors at these points. The additional tracking errors at the tip positions are therefore a result of the effect of moving the nearby redefined outputs along the desired trajectories. An approximate relationship for the additional tracking error between the redefined output of link i and its tip position can be found as follows. Refer to Figure 3.2 where point A corresponds to the redefined output and B corresponds to the tip–position of link i. Thus the additional error corresponds to the angle $\angle BO_iA$ in this figure which can be obtained from

$$\angle BO_iA = tan^{-1}\frac{\sum_k \phi_{ikt}\delta_k}{l_i} - tan^{-1}\frac{\sum_k \phi_{ik\alpha_i}\delta_k}{\alpha l_i} \tag{3.28}$$

where ϕ_{ikt} and $\phi_{ik\alpha_i}$ denote the kth shape function of link i evaluated at the tip position and the redefined output of link i, respectively. Assuming that the deflections are small compared to the length of the link, (3.28) can be written as

$$\angle BO_iA = \sum_k \frac{\alpha_i\phi_{ikt} - \phi_{ik\alpha_i}}{\alpha_i l_i}\delta_k \tag{3.29}$$

Now if (3.29) is normalized to the deflection of the link at the redefined output

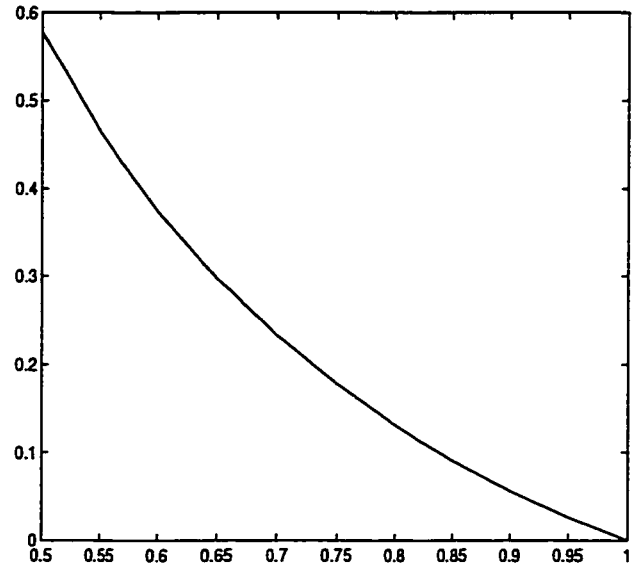

Figure 3.3: Variation of the approximate relative error $\frac{\angle BO_iA}{\angle AO_iC}$ (vertical axis) with the α_i of the redefined output.

(measured from the rigid body angle q_i) we have

$$\frac{\angle BO_iA}{\angle AO_iC} = \frac{\sum_k(\alpha_i\phi_{ikt} - \phi_{ik\alpha_i})\delta_k}{\sum_k \phi_{k\alpha_i}\delta_k} \tag{3.30}$$

Since the desired trajectories are usually smooth, the first flexural modes are excited more than the rest, i.e., $\delta_1 \gg \delta_2 \gg \cdots$. Therefore an approximation to (3.30) can be found as

$$\frac{\angle BO_iA}{\angle AO_iC} \approx \frac{\alpha_i\phi_{i1t} - \phi_{1\alpha_i}}{\phi_{1\alpha_i}} \tag{3.31}$$

3.2.1 Derivation of H(0,0)

It is noted that in order to use (3.17)–(3.18), $H(0,0)$ (or $M(0,0)$) should be known. Fortunately, since only M at $q = 0$ and $\delta = 0$ is required, the calculation of M is greatly simplified and a general method can be established for deriving $M(0,0)$ with any number of modes. This was done for a planar two–link manipulator used in our case study. To do so, it is sufficient to find the kinetic energy $\mathcal{K}_e$ of the system when it

passes through $q = 0$ and $\delta = 0$ and then use $\mathcal{K}_e(0,0) = \frac{1}{2}\begin{bmatrix} \dot{q}^T & \dot{\delta}^T \end{bmatrix} M(0,0) \begin{bmatrix} \dot{q} \\ \dot{\delta} \end{bmatrix}$ to find $M(0,0)$.

3.2.2 A Model for the Damping Term E_2

In this section we establish a model for the term E_2 introduced in (3.1) and used in (3.17). Considering (3.1) and eliminating $\ddot{q}$ from the equations, we get

$$N\ddot{\delta} + E_2\dot{\delta} + K\delta - M_{21}M_{11}^{-1}(V_1 + E_1\dot{q}) + V_2 = -M_{21}M_{11}^{-1}u \tag{3.32}$$

where V_1 and V_2 are the terms due to Coriolis and centripetal forces, and

$$N(q,\delta) = M_{22}(q,\delta) - M_{21}(q,\delta)M_{11}^{-1}(q,\delta)M_{12}(q,\delta) \tag{3.33}$$

Considering the dynamics of flexible modes ((3.32)) at $q, \dot{q} = 0$, and linearizing this equation about $\delta, \dot{\delta} = 0$ gives

$$N_o\ddot{\delta} + E_2\dot{\delta} + K\delta = f := -M_{21}M_{11}^{-1}u \tag{3.34}$$

where f is the total resulting forcing function and $N_o = N(0,0)$. Physically, (3.34) describes the dynamics of the flexible modes of the system when all the joints are locked at $q = 0$. Note that the matrices in (3.17)–(3.18) were evaluated at $q = 0$ and $\delta = 0$. The damping term can now be postulated as $E_2 = \alpha_N N_o + \beta_K K$ where α_N and β_K are constant positive scalars. This model is known as *Rayleigh Damping* in vibration theory (see e.g. [33]). Thus the damping factor of each mode is given [33] by $\xi_i = \frac{\alpha_N + \beta_K \omega_i^2}{2\omega_i}$, $i = 1, 2, \cdots, m$, where ω_i^2 is the i-th eigenvalue of $N_o^{-1}K$.

3.3 Case Studies

3.3.1 Regions having the Minimum–Phase Property for a Two–Link Manipulator

A planar two–link manipulator is studied in this section and the regions of output locations for achieving the minimum–phase property are obtained. The manipulator consists of two uniform bars with rectangular cross sections and considerable flexibility with the following numerical data

$$l_1 = l_2 = 0.7m,\ A_1(x_1) = A_2(x_2) = 7.44cm \times 0.46cm,$$

$$\rho = 2700kg/m^3\ (6061 Aluminum),\ M_1 = M_2 = 0.52kg,$$

$$E = 69.3 \times 10^9 N/m^2, J_1 = J_2 = 0.17kgm^2$$

where l_1 and l_2 are link lengths, A_1 and A_2 are cross sectional areas, E and ρ are modulus of elasticity and mass density, and M_1 , M_2, J_1 and J_2 are masses and mass moments of inertia at the end points of each link.

The damping model was chosen as discussed in the previous section. It was assumed that the damping ratio of the first mode, ξ_1, is given, and α_N , β_K contribute equally to this damping ratio. The extreme cases where either α_N or β_K are zero were also considered. The results were similar. Here, results are presented only for equal contribution of α_N and β_K. The vector α in (3.9) has the form $\alpha^T = [\alpha_1\ \alpha_2]$. The terms α_1 and α_2 were varied from -1 to $+1$ and the matrix A in (3.17) was tested for eigenvalues in the left half plane. Figure (3.4) shows the results for the region near the tip positions from $\alpha = 0.9$ to $\alpha = 1$. Three flexible modes were used in Figures 3.4a–3.4c, but for the rest, four flexible modes were used. The damping ratio was chosen as 10^{-14}, 10^{-7}, and 10^{-2}. When the damping ratio is very small, i.e. 10^{-14}, the regions of minimum–phase behavior are not reliable. A change in load configuration (Figure 3.4e–3.4i), or the number of flexible modes will change

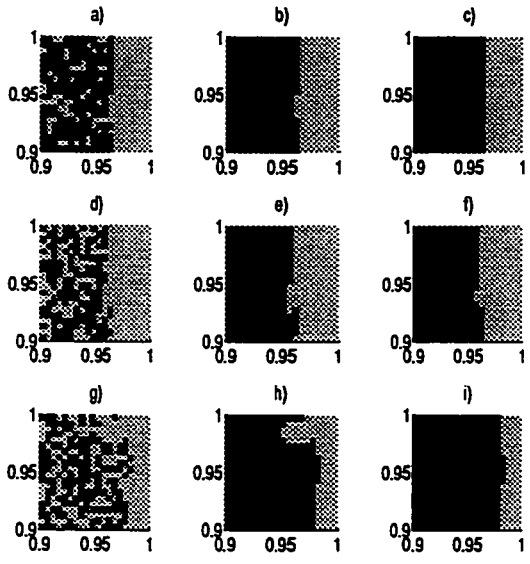

Figure 3.4: Regions of outputs for minimum–phase behavior (dark areas). Horizontal axis: α_1, Vertical axis: α_2. (a, b, c) Regions for $\xi_1 = 10^{-14}, 10^{-7}, 10^{-2}$ respectively when three flexible modes are used ($M_1 = M_2 = 0.52kg, J_1 = J_2 = 0.17kgm^2$). (d, e, f) Same as a–c when four flexible modes are used. (g, h, i) Same as d–f but with different loading, i.e., $M_1 = M_2 = 1.55kg$ and $J_1 = J_2 = 0.51kgm^2$.

this behavior. However, note that the damping ratio (ξ_1) is of the order of 0.01 for commonly used metals. It is also interesting to note that the behavior does not change much when we change ξ_1 from 10^{-7} to 10^{-2}. Moreover, there are points (e.g. $\alpha_1 = 0.9$, $\alpha_2 = 1$) which will preserve the minimum-phase property in spite of changes in load configuration (M_1, M_2, J_1, J_2), damping ratio (ξ_1), and the number of flexible modes. The discontinuities in Figure 3.4 are as the result of the resolution by which α is varied.

3.3.2 Inverse–Dynamics Control

A Single Flexible Arm

The control law developed in the previous sections was applied to a single–link flexible Aluminum arm with the following data

$$l = 1.3m,\ A = 8cm \times 1.5mm,\ M_p = 1kg,\ J_p = 0.002kgm^2,\ J_h = 3 \times 10^{-5}kgm^2$$

where l, A, M_p, J_p, J_h denote the length, payload mass, payload inertia and hub inertia respectively. The α–vector is now a scalar, and it was selected as $\alpha = 0.85$ designed based on a plant model with three modes. The control law (3.19) was then designed based on a model with two flexible modes with $K_p = 9$ and $K_d = 6$. In this way the performance of the controller is tested for higher frequency unmodeled dynamics. Figure 3.5 illustrates the simulation results. It is interesting to note that to achieve tip position tracking the hub angle has to evolve in an oscillatory fashion. In this case, the closed–loop system was stable for $K_\delta = K_{\dot{\delta}} = 0$, but this is not the case in general, as discussed in the next example.

A Two–Link Planar Manipulator

A two–link planar manipulator is considered in which the first link is rigid and the second link is flexible. In this way significant nonlinearities are introduced in the dynamic equations compared to the single–link case. The two–link data are

$$l_1 = 0.2m,\ l_2 = 1.3m,\ A_1 = 4.8387 \times 10^{-3}m^2,\ A_2 = 0.9975 \times 10^{-4}m^2$$

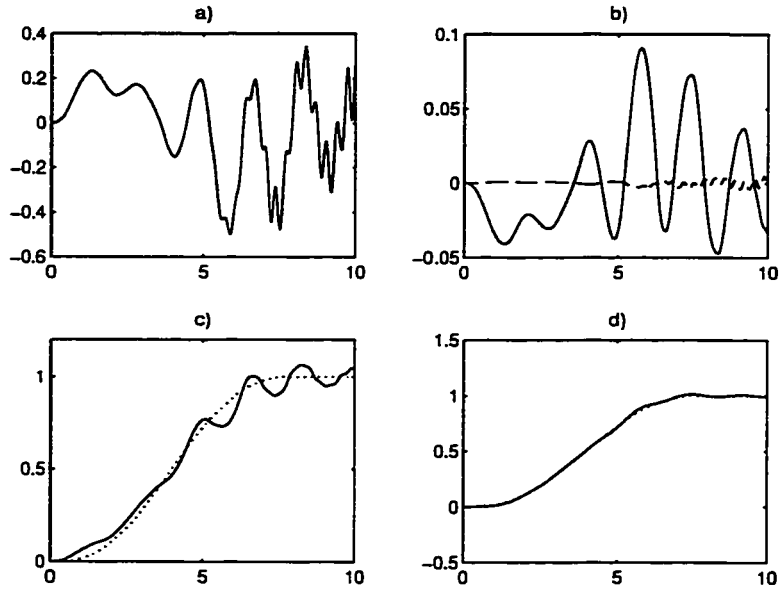

Figure 3.5: Simulation results for a single–link arm using inverse dynamics. (a) Input torque (Nm) vs. time (sec) (b) Flexible modes (m) (first mode:–, second mode:––, third mode: not shown) (c) Joint position (–) and reference trajectory (...) in radians (d) Tip position (–) and reference trajectory (...) in radians.

$$\rho = 7860kg/m^3\ (Steel),\ M_1 = M_2 = 1kg,$$

$$E = 206 \times 10^9 N/m^2, J_1 = J_2 = 0.002kgm^2, J_h = 3 \times 10^{-5}kgm^2$$

The two–link system is modeled by the assumed modes method with two flexible modes. Further E_1 and E_2 are assumed to be zero. Using (3.17), α was chosen to be close to 1 and such that the zeros are purely imaginary. This gave a critical value of $\alpha = 0.943$. Then $K_\delta(q)$ and $K_{\dot{\delta}}(q)$ were chosen such that at each point q (the second joint position variable), the matrix $A_\Delta(q)$ in (3.25) is a Hurwitz matrix. This was achieved by solving a pole placement problem at ten points and using linear interpolation to obtain $K_\delta(q)$ and $K_{\dot{\delta}}(q)$ at other points. It is important to choose the eigenvalues of $A_\Delta(q)$ close to the $j\omega$ axis so that small $K_\delta(q)$ and $K_{\dot{\delta}}(q)$ are obtained for better robustness (see Appendix A.2). Setting these gains to zero resulted in an unstable system. The maximum torque required for tracking was about 5 Nm which was reduced to less than 1 Nm when α was reduced to 0.9. The

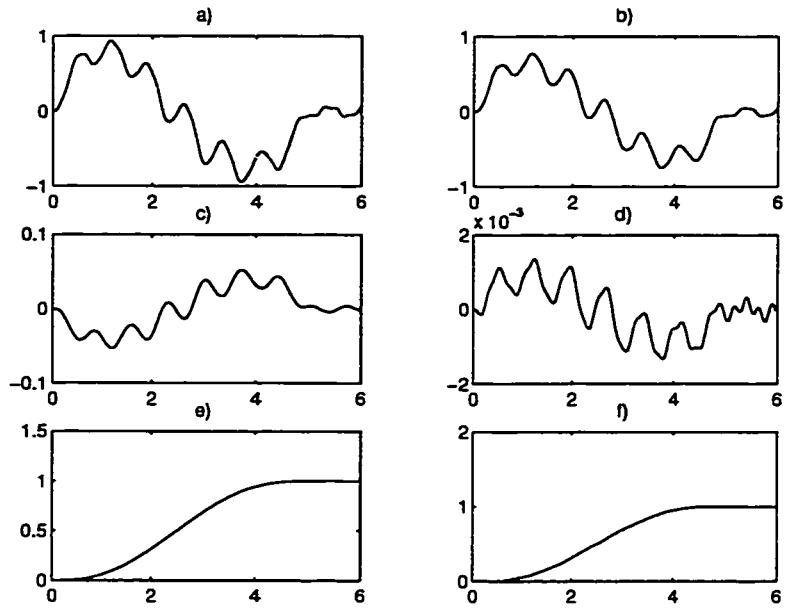

Figure 3.6: Simulation results for a two link manipulator ($x-axis$: time (sec)). (a) First actuator torque (Nm) (b) Second actuator torque (Nm) (c) First flexible mode (m) (d) Second flexible mode (m) (e) First tip position trajectory (–) and reference trajectory (...) in radians (f) Second tip position trajectory (–) and reference trajectory (...) in radians.

results for $\alpha = 0.9$ are shown in Figure 3.6.

3.4 Conclusion

The control strategy discussed in this chapter yields sufficiently small tip–position errors and good robustness properties. This may be attributed to the decoupling effect of the input–output linearization technique. The control strategy was designed for a special class of manipulators in which the major deflection coordinates are in the same direction as the joint coordinates. A possible solution to the more general case is either through proper mechanical structure design or by introducing extra control inputs to affect flexibilities in other directions. From the two–link example it was also found that controlling the flexibility effects of the second link by the input control of the first link is hardly ever achievable and stability problems may

arise. Thus the solution to the more general case may be offered by adding extra control inputs and better mechanical design. A drawback of this strategy may, however, be the requirement for full measurement of the states. Practically, joint positions and their rates as well as deflection variables (δ) are measurable but $\dot{\delta}$ is not directly measurable and should be estimated or reconstructed from deflection variable measurements (see e.g. [55]).

Chapter 4

Observer–Based Decoupling Control

In this chapter, we focus on the design of an observer–based inverse dynamics control strategy that results in sufficiently small tip–position tracking errors while maintaining robust closed–loop performance for a class of multi–link structurally flexible manipulators. The control design is essentially based on the method described in Chapter 3. As part of the control design, a nonlinear observer is introduced to estimate the rates of change of flexible modes. By a proper choice of control and observer gains, the error dynamics are guaranteed to consist of a stable linear part plus a bounded perturbation term that results in asymptotically stable observation and closed–loop system stability with small tip position tracking errors. Experimental results are given for the case of a two–link flexible manipulator that further confirm the theoretical and simulation results.

4.1 Introduction

Accurate knowledge of state variables is required by many advanced control algorithms for flexible multi–link robots, e.g. see [57], [8], [79]. It is possible to measure

joint positions, velocities, and flexible modes of manipulators using shaft encoders, tachometers, and strain gauges [64], respectively. However measuring rates of change of flexible modes cannot be easily or accurately accomplished. One method is to integrate the outputs of accelerometers installed along the arms or to use analog differentiation of the deflection variables [55]. The former approach may be restricted from economic considerations and the latter because of noise problems. Thus a nonlinear state observer is desirable in these circumstances. Several authors have studied the development of nonlinear observers in the general context of nonlinear systems or specifically intended for (mainly) rigid robot manipulators [60], [61], [62], [63]. In [58] the so called pseudo–linearization technique was used where the nonlinear robot dynamics are transformed into a linear model by a nonlinear state–space change of coordinates. Sliding techniques were introduced in [60], [61] where the attractive manifold concept was employed.

The organization of this chapter is as follows. First, the control strategy described in Chapter 3 is employed to choose points near the tip outputs such that stable zero–dynamics are achieved. As before, it is assumed that the vibrations are mainly lateral vibrations about the axis of each link. Second, an observation strategy is developed by studying certain characteristics of the dynamics of flexible modes of structurally flexible manipulators. In particular, the observer requires that joint angles and velocities as well as flexible modes are available in order to estimate the rates of change of flexible modes. It is also shown that sliding observer techniques such as those in [60], [61] can be easily incorporated in the design. The observation strategy is quite general and is applicable even if the above assumption regarding the arm shapes is relaxed.

A closed–loop stability analysis is performed and conditions for achieving stable closed–loop behavior are stated. The theoretical developments are further enhanced by experimental studies for a two–link flexible manipulator with promising

results. In particular, stable closed–loop performance with small tip position tracking errors is achieved with readily available and economic sensor equipment. Furthermore, relatively large control gains can be used, resulting in reduced closed–loop system sensitivity that would otherwise not be achieved by conventional methods.

4.2 Inverse Dynamics Control

Consider the control strategy discussed in Chapter 3. For convenience let us again re–write the dynamics of a flexible multi–link system given by (3.1) without the damping coefficients, i.e.,

$$M(q,\delta)\begin{bmatrix}\ddot{q}\\ \ddot{\delta}\end{bmatrix}+\begin{bmatrix}f_1(q,\dot{q})+g_1(q,\dot{q},\delta,\dot{\delta})\\ f_2(q,\dot{q})+g_2(q,\dot{q},\delta,\dot{\delta})+K\delta\end{bmatrix}=\begin{bmatrix}u\\ 0\end{bmatrix} \tag{4.1}$$

Now, defining the output vector (see Chapter 3), i.e.,

$$y = q + \Psi_{n\times m}(\alpha)\delta \tag{4.2}$$

where $\Psi(\alpha)$ is a matrix depending on modal shape functions and the vector $\alpha^T = [\alpha_1 \cdots \alpha_n]$ defines physical output locations on the links for achieving stable zero–dynamics [69]. The input–output description of (4.1) with the output described by (4.2) is then obtained by differentiating the output vector y with respect to time until the input vector appears, which is given by

$$\ddot{y} = a(\alpha, x) + B(\alpha, q, \delta)u \tag{4.3}$$

where $B(\alpha,q,\delta) = H_{11} + \Psi_{n\times m}H_{21}$ and

$$a(\alpha,x) = -(H_{11}+\Psi H_{21})(f_1+g_1) - (H_{12}+\Psi H_{22})(f_2+g_2+K\delta) \tag{4.4}$$

Now let us define a finite domain around the desired reference trajectory q_r, $\dot{q}_r$ given by

$$\Omega_r = \{x : \mid q-q_r \mid < \kappa_1,\ \mid \dot{q}-\dot{q}_r \mid < \kappa_2,\ \mid \delta \mid < \kappa_3,\ \mid \dot{\delta} \mid < \kappa_4\} \tag{4.5}$$

where κ_i $(i = 1, \cdots, 4)$ are some positive bounds. Also assume that $B(\alpha, q, \delta)$ is nonsingular in Ω_r. This is a controllability like assumption and is guaranteed to hold when for instance $\alpha = 0$. Now, let u take the following form

$$u = B^{-1}(\alpha, q, \delta)(v - a(\alpha, x)) + K_\delta(q)\delta + K_{\dot{\delta}}(q)\dot{\hat{\delta}} \tag{4.6}$$

where $K_\delta(q)$ and $K_{\dot{\delta}}(q)$ are gain matrices that are to be specified later and intended to make $A_\Delta(q)$ given by (4.24) a Hurwitz matrix. It then follows from (4.3) that

$$\ddot{y} = v + BK_\delta(q)\delta + BK_{\dot{\delta}}(q)\dot{\delta} \tag{4.7}$$

which is an input–output linearization of the system when $K_\delta(q)$ and $K_{\dot{\delta}}(q)$ are zero. As discussed later, these terms are added to enhance robustness and should usually be selected sufficiently small. In the above formulations, it is assumed that $\dot{\delta}$ is available. This assumption is relaxed later on by replacing $\dot{\delta}$ with its estimation from a nonlinear observer.

4.3 Observer Design

In this section our proposed observation strategy is introduced. Three cases are considered as described below.

4.3.1 Full–Order Observer

Consider the dynamics of a multi–link flexible manipulator given by (4.1). Defining $\delta_1 = \delta$ and $\delta_2 = \dot{\delta}$, the dynamics of flexible modes are written as

$$\begin{aligned}
\dot{\delta_1} &= \delta_2 \\
\dot{\delta_2} &= -H_{21}(q, \delta_1)(f_1(q, \dot{q}) + g_1(x)) - H_{22}(q, \delta_1)(f_2(q, \dot{q}) + g_2(x)) + K\delta_1) \\
&+ H_{21}(q, \delta_1)u
\end{aligned} \tag{4.8}$$

where $x^T = [q^T \ \dot{q}^T \ \delta_1^T \ \delta_2^T]$ as before. Let us choose the following structure for the observer dynamics

$$\begin{aligned}
\dot{\hat{\delta}}_1 &= \hat{\delta}_2 + L_1(\delta_1 - \hat{\delta}_1) \\
\dot{\hat{\delta}}_2 &= -H_{21}(q,\delta_1)(f_1(q,\dot{q}) + g_1(x_c)) - H_{22}(q,\delta_1)(f_2(q,\dot{q}) + g_2(x_c) + K\hat{\delta}_1) \\
&+ H_{21}(q,\delta_1)u + (-H_{22}(q,\delta_1)K + L_2)(\delta_1 - \hat{\delta}_1)
\end{aligned} \tag{4.9}$$

where $x_c^T = [q^T \ \dot{q}^T \ \delta_1^T \ \hat{\delta}_2^{\,T}]$ is the available state vector that may be used for control purposes and L_1 and L_2 are observer gain matrices to be selected. Defining the estimation errors $\tilde{\delta}_1 = \delta_1 - \hat{\delta}_1$, $\tilde{\delta}_2 = \delta_2 - \hat{\delta}_2$, the observer error dynamics can be obtained by subtracting (4.9) from (4.8), i.e.,

$$\dot{\tilde{\delta}} = A_{\tilde{\delta}}\tilde{\delta} + b_{\tilde{\delta}}(x, \hat{\delta}_2) \tag{4.10}$$

where $\tilde{\delta}^T = [\tilde{\delta}_1^{\,T} \ \tilde{\delta}_2^{\,T}]$ and

$$\begin{aligned}
A_{\tilde{\delta}} &= \begin{bmatrix} -L_1 & I \\ -L_2 & 0 \end{bmatrix} \\
b_{\tilde{\delta}}(x, \hat{\delta}_2) &= \begin{bmatrix} 0 \\ H_{21}(-\frac{\partial g_1}{\partial \delta_2}\,|_{\hat{\delta}_2}\ \tilde{\delta}_2 + O_1(\tilde{\delta}_2^{\,2})) + H_{22}(-\frac{\partial g_2}{\partial \delta_2}\,|_{\hat{\delta}_2}\ \tilde{\delta}_2 + O_2(\tilde{\delta}_2^{\,2})) \end{bmatrix}
\end{aligned} \tag{4.11}$$

The terms in (4.11) have been obtained by using the Taylor series expansions of g_1 and g_2 and noting that $\hat{\delta}_2 = \delta_2 - \tilde{\delta}_2$, i.e.,

$$\begin{aligned}
g_1(x_c) &= g_1(q,\dot{q},\delta_1,\delta_2) - \frac{\partial g_1}{\partial \delta_2}\,|_{\hat{\delta}_2}\ \tilde{\delta}_2 + O_1(\tilde{\delta}_2^{\,2}) \\
g_2(x_c) &= g_2(q,\dot{q},\delta_1,\delta_2) - \frac{\partial g_2}{\partial \delta_2}\,|_{\hat{\delta}_2}\ \tilde{\delta}_2 + O_2(\tilde{\delta}_2^{\,2})
\end{aligned} \tag{4.12}$$

It should be noted that since the components of δ_2 in g_1 and g_2 are at most of second order (centrifugal terms), the above Taylor series expansions terminate after the square terms. Moreover, considering a finite region Ω_o around the desired point $(x, \hat{\delta}_2)$, it follows that $\|b_{\tilde{\delta}}(x, \hat{\delta}_2)\| < k\|\tilde{\delta}\|$. If L_2 is of the same order of magnitude as H_{21} and H_{22}, the coefficient k is typically small. This follows by noting that $\frac{\partial g_1}{\partial \delta_2}\,|_{\hat{\delta}_2}$

and $\frac{\partial g_2}{\partial \delta_2}|_{\bar{\delta}_2}$ are $O(\delta\dot{\tilde{\delta}})$. Moreover, the matrix $A_{\bar{\delta}}$ can be made Hurwitz by a proper choice of the gains L_1 and L_2, e.g., by selecting L_1 and L_2 to be any positive definite matrices. Thus, choosing a Lyapunov function candidate $V_o = \tilde{\delta}^T P_{\bar{\delta}} \tilde{\delta}$, where $P_{\bar{\delta}}$ is the solution of the Lyapunov equation

$$A_{\bar{\delta}}^T P_{\bar{\delta}} + P_{\bar{\delta}} A_{\bar{\delta}} = -Q_{\bar{\delta}} \tag{4.13}$$

it follows that $\dot{V}_o \leq -(\lambda_{min}(Q_{\bar{\delta}}) - 2\lambda_{max}(P_{\bar{\delta}})k)\|\tilde{\delta}\|^2$. Hence, provided that $\lambda_{min}(Q_{\bar{\delta}}) > 2k\lambda_{max}(P_{\bar{\delta}})$ it follows that the error dynamics are locally asymptotically stable. Note that if parametric uncertainties are included, the error dynamics will converge to a residual set around the origin as shown in the sequel. In this case, assuming a bounded input vector u, it follows that $\|b_{\bar{\delta}}\| < k\|\tilde{\delta}\| + k_u$, where k_u is an upper bound on all the terms due to parametric uncertainties. Then assuming that $\lambda_{min}(Q_{\bar{\delta}}) > 2k\lambda_{max}(P_{\bar{\delta}})$,

$$\dot{V}_o \leq -(\lambda_{min}(Q_{\bar{\delta}}) - 2\lambda_{max}(P_{\bar{\delta}})k)\|\tilde{\delta}\|^2 + 2\lambda_{max}(P_{\bar{\delta}})k_u\|\tilde{\delta}\| \tag{4.14}$$

Furthermore, V_o can be written as

$$\lambda_{min}(P_{\bar{\delta}})\|\tilde{\delta}\|^2 \leq V_o \leq \lambda_{max}(P_{\bar{\delta}})\|\tilde{\delta}\|^2 \tag{4.15}$$

It then follows from (4.14) and (4.15) that for all $\tilde{\delta} \in \Omega_o$ we have

$$\dot{V}_o \leq -\gamma_1 V_o + \gamma_2 V_o^{1/2} \tag{4.16}$$

where $\gamma_1 = (\lambda_{max}(Q_{\bar{\delta}}) - 2\lambda_{max}(P_{\bar{\delta}}))/\lambda_{max}(P_{\bar{\delta}})$ and $\gamma_2 = 2\lambda_{max}(P_{\bar{\delta}})/\lambda_{min}(P_{\bar{\delta}})$. Considering (4.16), we can conclude that if $V_o(0) > \gamma_2^2/\gamma_1^2$, then $\dot{V}_o < 0$. Thus the smallest residual set can be defined as $T_{res} = \{\tilde{\delta} \mid V_o \leq \gamma_2^2/\gamma_1^2\} \subset \Omega_o$ for which γ_2^2/γ_1^2 is minimum.

4.3.2 Reduced–Order Observer

It is possible to obtain a reduced–order observer using a similar technique as above. To this end, consider the following observation law

$$\dot{\hat{\delta}}_2 = -H_{21}(q, \delta_1)(f_1(q, \dot{q}) + g_1(x_c)) - H_{22}(q, \delta_1)(f_2(q, \dot{q}) + g_2(x_c) + K\delta_1)$$

$$+ \quad H_{21}(q,\delta_1)u + G(\hat{\delta}_2 - \delta_2) \tag{4.17}$$

where G is a Hurwitz gain matrix and x_c is as defined previously. The above equation reflects the fact that $\delta_2 = \dot{\delta}_1$ is not measurable. However, by taking $G\delta_2$ to the left–hand side of the equation and defining the auxiliary state variable $\hat{z} = \hat{\delta}_2 + G\delta_1$, it may be shown that

$$\begin{aligned} \dot{\hat{z}} &= G\hat{z} - H_{21}(q,\delta_1)(f_1(q,\dot{q}) + g_1(x_c)) - H_{22}(q,\delta_1)(f_2(q,\dot{q}) + g_2(x_c) + K\delta_1) \\ &+ H_{21}(q,\delta_1)u - G^2\delta_1 \end{aligned} \tag{4.18}$$

Similarly, defining an auxiliary state variable for the system dynamics as $z = \delta_2 + G\delta_1$, and subtracting the second equation in the resulting dynamics from (4.18), it follows that

$$\dot{e}_z = Ge_z + b_{\bar{\delta}_2}(x, \hat{\delta}_2) \tag{4.19}$$

where $b_{\bar{\delta}_2}(x, \hat{\delta}_2)$ is the second element of $b_{\bar{\delta}}(x, \hat{\delta}_2)$ given by (4.11) and $e_z = z - \hat{z}$. Thus, if G is a Hurwitz matrix the error dynamics are stabilized locally. Note that (4.18) is now implementable. Thus, once $\hat{z}$ is obtained then $\hat{\delta}_2$ may be obtained from $\hat{\delta}_2 = \hat{z} - G\delta_1$. When parametric uncertainties are present a similar analysis as before can be developed to guarantee asymptotic stability of the error dynamics.

4.3.3 Sliding Observer

The sliding technique introduced in [61] and mentioned in the Introduction section may be incorporated in the full–order observer design established earlier. Towards this end, let L_1 and L_2 be positive definite diagonal matrices with diagonal elements l_{1i} and l_{2i}, $i = 1 \cdots m$, respectively. Then, by adding terms $K_{s1i}sgn(\tilde{\delta}_{1i})$ and $K_{s2i}sgn(\tilde{\delta}_{2i})$ ($sgn(.)$ is the signum function) to the observation laws (4.9), the resulting observer dynamics can be written as

$$\begin{aligned} \dot{\tilde{\delta}}_{1i} &= -l_{1i}\tilde{\delta}_{1i} + \tilde{\delta}_{2i} - K_{s1i}sgn(\tilde{\delta}_{1i}) \\ \dot{\tilde{\delta}}_{2i} &= -l_{2i}\tilde{\delta}_{1i} - K_{s2i}sgn(\tilde{\delta}_{1i}) + \Delta f_i, \quad i = 1, \cdots, m \end{aligned} \tag{4.20}$$

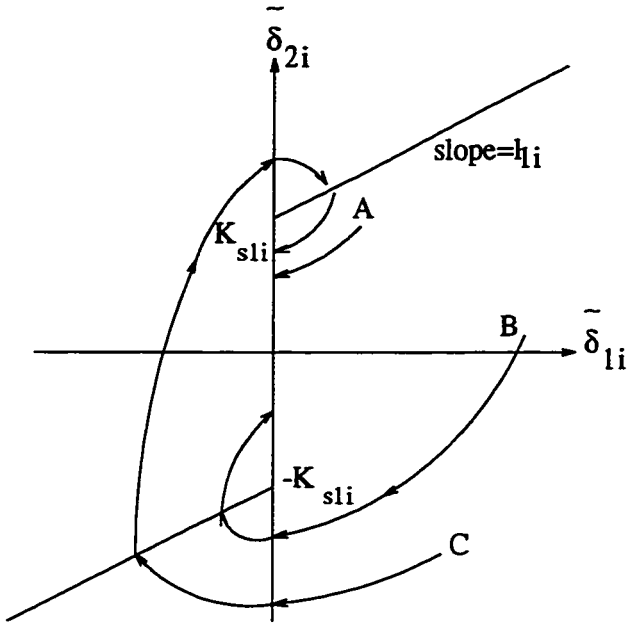

Figure 4.1: Phase–plane trajectories for the sliding observer.

where Δf_i contains perturbation terms and modeling uncertainties. Then for each $\tilde{\delta}_{1i}$–$\dot{\tilde{\delta}}_{2i}$, the sliding condition is satisfied in the region $\dot{\tilde{\delta}}_{2i} \leq K_{s1i} + l_{1i}\tilde{\delta}_{1i}$, if $\tilde{\delta}_{1i} > 0$ and $\dot{\tilde{\delta}}_{2i} \geq -K_{s1i} + l_{1i}\tilde{\delta}_{1i}$, if $\tilde{\delta}_{1i} < 0$. The dynamics on the *sliding patch* ($\mid \dot{\tilde{\delta}}_{2i} \mid < K_{s1i}$) are derived from Filippov's solution concept [66], i.e., $\dot{\tilde{\delta}}_{2i} = -(K_{s2i}/K_{s1i})\dot{\tilde{\delta}}_{2i} + \Delta f_i$. Now if K_{s2i} is selected such that $\mid \Delta f_i \mid < K_{s2i}$ the phase–plane trajectories are in the form given in Figure 4.1. Note that the slope l_{1i} affects regions of direct attraction to the sliding region.

In the rest of this chapter we will incorporate the observer strategies introduced above into the inversion based control law given by (4.6). The developments are carried out for the case of a full–order observer. However, a similar analysis can be done for the reduced–order observer.

4.4 Observer Based Inverse–Dynamics Control

In this section we use the control law introduced in section 4.2 except that $\dot{\delta}$ is replaced by $\dot{\hat{\delta}}$ given by one of the observer strategies discussed in section 4.3. Since

the redefined output velocity is not available we use its estimated value from $\dot{q} + \Psi\hat{\delta}_2$. Thus, the estimated redefined output velocity tracking error can be defined as $\dot{\hat{e}} = \dot{y}_r - (\dot{q} + \Psi\hat{\delta}_2)$ and the redefined output tracking error by $e = y_r - y$. In these relationships y_r and $\dot{y}_r$ are the reference trajectory and its velocity profile, respectively. Choosing $v = \ddot{y}_r + K_p e + K_d \dot{\hat{e}}$ with K_p, K_d determined by the output position error dynamics, yields

$$\dot{E} = A_E E + d_E(\alpha, x_c, t) \tag{4.21}$$

with

$$\begin{aligned} d_E(\alpha, x_c, t) &= -BK_\delta(q)\delta - BK_{\dot{\delta}}(q)\dot{\tilde{\delta}} + O(\|K_d\|\tilde{\delta}) + O(\delta\dot{\tilde{\delta}}\tilde{\delta}) \\ E^T &= \begin{bmatrix} e^T & \dot{e}^T \end{bmatrix} \\ A_E &= \begin{bmatrix} 0 & I \\ -K_p & -K_d \end{bmatrix} \end{aligned} \tag{4.22}$$

Moreover, (4.8) can be written in terms of u given by (4.6), that is

$$\dot{\Delta} = A_\Delta(q)\Delta + \begin{bmatrix} 0 \\ G_\Delta(x, \dot{\tilde{\delta}}, t) \end{bmatrix} \tag{4.23}$$

where

$$\begin{aligned} G_\Delta(x, \dot{\tilde{\delta}}, t) &= H_{21}B^{-1}(\ddot{y}_r + K_p e + K_d \dot{e}) - P(q)(f_2(q, \dot{q}) + g_2(x_c)) + O(\delta) + O(\delta\tilde{\delta}) \\ A_\Delta(q) &= \begin{bmatrix} 0 & I \\ -P(q)K - H_{210}K_\delta(q) & -H_{210}K_{\dot{\delta}}(q) \end{bmatrix} \\ \Delta^T &= [\delta^T \ \dot{\delta}^T] \end{aligned} \tag{4.24}$$

in which $H_{210} = H_{21}(q, 0)$ and

$$P(q) = [H_{220} - H_{210}(H_{110} + \Psi H_{210})^{-1}(H_{120} + \Psi H_{220})]. \tag{4.25}$$

Furthermore, matrices $K_\delta(q)$ and $K_{\dot{\delta}}(q)$ are selected such that $A_\Delta(q)$ is a Hurwitz matrix for the range in which q is varied. This can be guaranteed if the pair

$(B_{\Delta_0}, A_{\Delta_0})$ is locally controllable on the domain of interest with

$$A_{\Delta_0}(q) = \begin{bmatrix} 0 & I \\ -P(q)K & 0 \end{bmatrix}$$

and

$$B_{\Delta_0}(q) = \begin{bmatrix} 0 \\ H_{210} \end{bmatrix}. \tag{4.26}$$

Noting that A_E, A_Δ, and $A_{\bar{\delta}}$ are Hurwitz matrices, it can then be shown (using a Lyapunov analysis) that the trajectories of the closed–loop system converge to a residual set with small tracking errors e and $\dot{e}$ and bounded δ and $\dot{\delta}$ provided that certain conditions are satisfied. The following theorem summarizes the above results

Theorem *Let the control law (4.6) be applied to the original nonlinear system (4.1) with $B(q, \delta, \alpha)$ nonsingular in Ω_r (see (4.5)) and the pair $(B_{\Delta_0}, A_{\Delta_0})$ given by (4.26) controllable in Ω_r. Consider sets $\mathcal{R}$, $\mathcal{S}$ and $\mathcal{T}$ given by (A.37). Provided that the desired trajectories and their time derivatives (at least up to order 2) are continuous and bounded, it then follows that the trajectories of E, $\epsilon\Delta$ and $\tilde{\delta}$ (ϵ is a small scaling factor as discussed in Appendix A.3), starting from $\mathcal{S} - \mathcal{R}$ converge to a residual set $\mathcal{T}$ that can be made small by proper choice of controller parameters, if d_E and G_Δ given by (4.22) and (4.24), respectively satisfy certain norm conditions ((A.32) and (A.33)) in a bounded region Ω_i (given in Appendix A.3) of the full state space $(E, \Delta, \tilde{\delta})$.*

Proof: The proof of the above result is established in Appendix A.3.

Remark: Choice of Observer Gain Matrices

It is revealed from the analysis in section 4.3 that to ensure asymptotic stability of the observer dynamics, the ratio $r = \lambda_{max}(P_{\bar{\delta}})/\lambda_{min}(Q_{\bar{\delta}})$ has to be made sufficiently small. This will also reduce the size of the residual set. To this end, let us consider $Q_{\bar{\delta}} = I$ (see e.g. [65]) and choose $L_1 = l_1 I$ and $L_2 = l_2 I$, where l_1 and

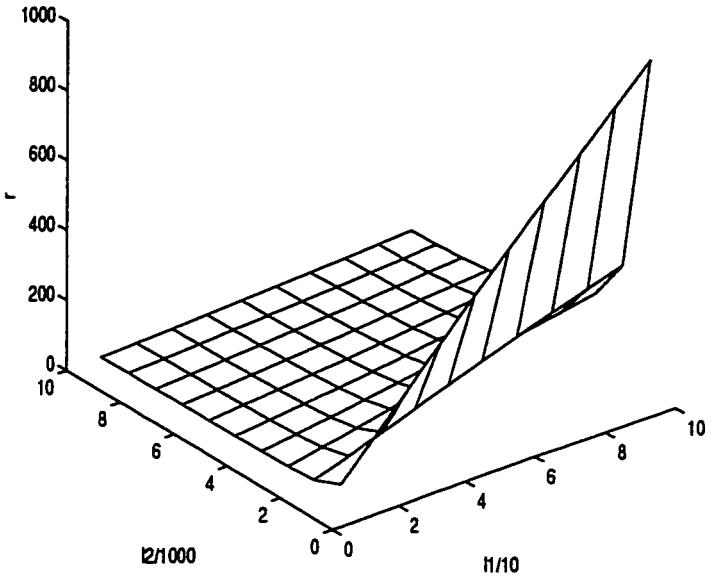

Figure 4.2: Plot of r versus observer gains.

l_2 are positive scalar parameters. A plot of r versus l_1 and l_2 is shown in Figure 4.2. It follows that observer gains have to be increased to achieve better observer robustness. For the sliding observer, these gains are infinite during sliding and are reduced outside the sliding region. Note, however that increasing the observer gains will increase sensitivity with respect to measurement noise. Thus, there is a limit as to how much the gains can be increased. Under certain noise conditions, Slotine *et al.* [61] have shown that sliding observers exhibit superior behavior when compared to Luenberger or Kalman filters.

4.5 Implementation of the Control Law

In this section the practical implementation of the control strategy discussed in this chapter is considered next. Figure 4.3 shows the schematic diagram of our experimental setup. The flexible link is a stainless-steel $60cm \times 5cm \times 0.9mm$

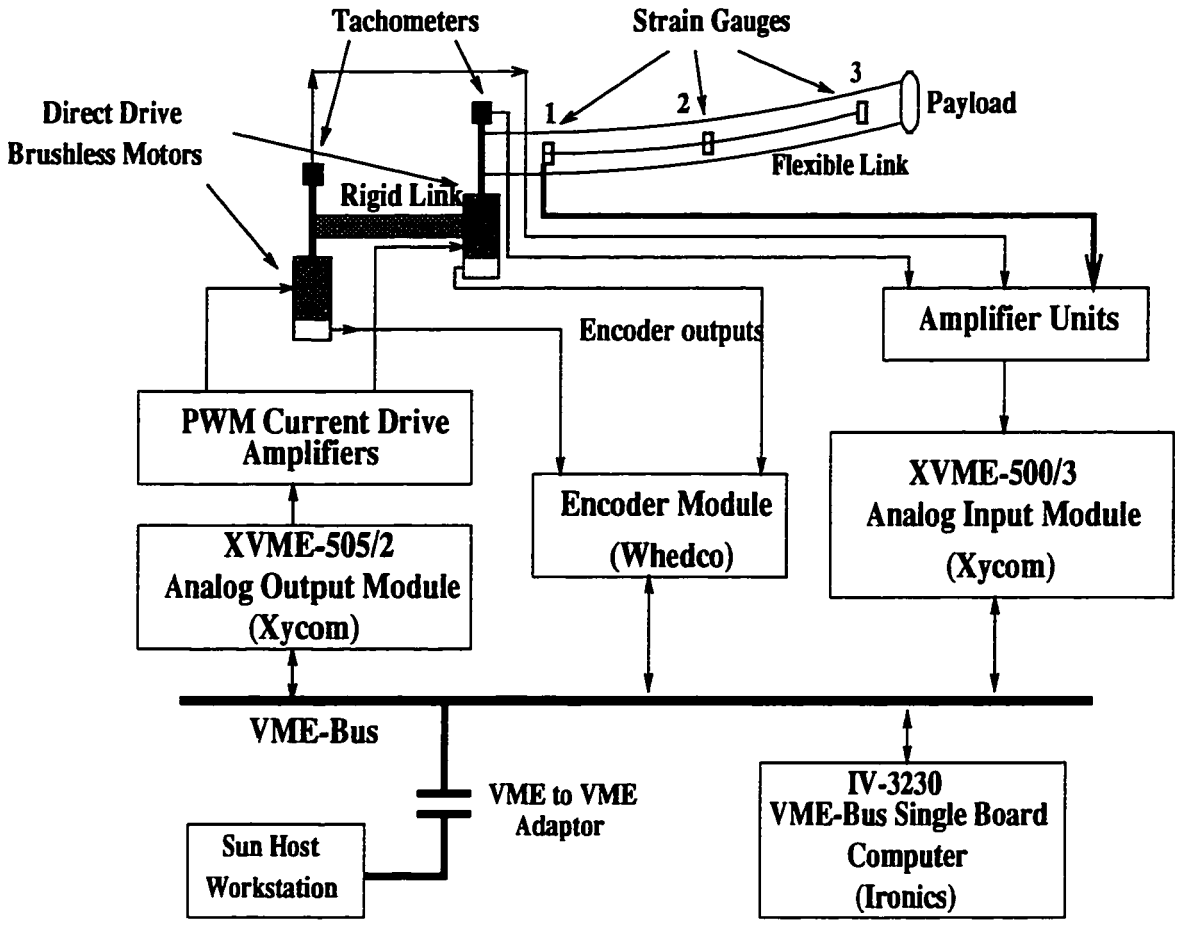

Figure 4.3: Experimental setup for the flexible–link robot.

rectangular bar with a $0.251kg$ payload attached to its end point. The mass of the bar is $0.216kg$ that is comparable to its payload. The first link is a $20cm$ rigid aluminum bar. The two–link set up has significant nonlinear and non–minimum phase characteristics and its dynamics exhibit nonlinearities that are similar to the case where both links are flexible.

The first two flexible modes of this system when linearized around zero joint angles are 5.6 and 27.6 Hz. The roots corresponding to the linearized zero dynamics (when the tip position is taken as the output) are at $\pm j76.9$ and ± 16.0. This setup is essentially the same as one described in Chapter 2 (Figure 2.6) except for the rigid first link. The sensory equipment consists of three strain gauge bridges, two

tachometers and two shaft–encoders that are used to measure the flexible modes of the link, joint rates, and joint positions, respectively. The signals from the strain gauge bridges and the tachometers are then amplified using low–drift amplifier stages and further passed through anti–aliasing filters. These signals are then fed into the *XVME-500/3* analog input module from *Xycom*. The actuators are *5113 Pittman* DC brushless servomotors which are direct driven by *503 Copley* PWM servo–drive amplifiers. The digital hardware has been selected based on the idea of a *reconfigurable* sensor–based control application as described in Chapter 2. The tip deflection is again constructed based on the measurements obtained from the strain gauges (see Chapter 2).

The differential equations corresponding to a given observation strategy have to be solved numerically for a digital implementation. The numerical algorithm has to be fast enough so that the results are computed and made available well before the end of each sampling period. The procedure adopted here is the *modified midpoint* method [74] which was also used in Chapter 2. The implemented algorithm took approximately 2 msec on the MC68030 Ironics processor board. Thus, a sampling frequency of 350 Hz was used. This rate was sufficient to allow computation of the control law as well as the data acquisition and trajectory generation tasks while maintaining closed–loop system stability.

Due to mechanical imprecisions in the physical construction of the manipulator the arm is not completely level in the horizontal plane. This can lead to considerable errors due to the fact that the magnitude of the required torque for control is small specifically at stopping points. The problem can be resolved to some extent by adding a compensating torque in the form of a Taylor series expansion of the static gravity torques up to the third power of joint angles. The Taylor series coefficients were thus estimated by measuring the balancing torques at several joint angles and using the least–squares algorithm.

4.5.1 Experimental Results

The control law for the two–link system was obtained based on the dynamic model given in Appendix C.2. The model was obtained by using the symbolic manipulation software *MAPLE* [35] but only *one* flexible mode was used in system modeling for control design. It would be reasonable to expect that the control performance based on a model with two flexible modes should result in better performance. However, it was found that the model based on a single mode gave better results. The explanation for this is that the mass matrix of the flexible–link system becomes more ill–conditioned as the number of flexible modes is increased. As a result, the inverted matrix becomes more sensitive to modeling errors and uncertainties, leading to poor or even unstable performance.

Figure 4.4 shows the condition number of the mass matrix as a function of time for a quintic trajectory tracking control of the second flexible arm shown in Figure 4.3. The problem can further be explained as follows. In practice the estimates $\hat{B}$ and $\hat{a}$ of B and a respectively in (4.6) are at our disposal. Also note that these terms are both affected by the inverse of the mass matrix. Thus taking $B^{-1} = \hat{B}^{-1} - \Delta B_I$ and $a = \hat{a} - \Delta a$, where ΔB_I and Δa are the error terms, the tracking error dynamics can be obtained from (4.7), i.e.,

$$\ddot{e} + K_d\dot{e} + K_p e = \Delta B_I(v - a + \Delta a) + B^{-1}\Delta a + B(K_\delta(q)\delta + K_{\dot{\delta}}(q)\dot{\hat{\delta}}) \qquad (4.27)$$

Now, with a more ill–conditioned mass matrix the error terms, ΔB_I and Δa are likely to increase and destabilize the system. Thus there are two conflicting requirements in this regard: The ill–conditioning due to an increased number of modes and loosing control over higher flexural modes due to neglecting them in the control law. Both these factors can lead to instability. Therefore, the question of how many modes to take for satisfactory performance is difficult to quantify and should be decided in practice.

In all experiments, the *redefined* output of the second link was chosen to correspond to the angle from hub to the point at $0.8l_2$ (l_2 is the length of the second link). This location was obtained to be as near the tip position as possible while maintaining the non–minimum phase characteristic (as described in Chapter 3). The output of the first link is the joint angle itself. However, in all of the figures, the tip output is reported instead of the re–defined output. Figure 4.5 shows the results when a reduced–order observer is used to estimate rates of change of the deflection modes and the control goal is to track a 3 second quintic polynomial trajectory with a 2 second tail of zero velocity and acceleration. The observer gain was $G = -120$ and the error dynamics gains were $K_p = 22.1I_{2\times2}$ and $K_d = 9.4I_{2\times2}$. K_δ and $K_{\dot{\delta}}$ were zero since the small damping of the flexible–link was enough to guarantee stability. Similarly, the results for the other observation schemes are given in Figures 4.6 and 4.7 with $L_1 = 100I_{2\times2}$, $L_2 = 19000I_{2\times2}$, $K_p = 30.3I_{2\times2}$, $K_d = 11.0I_{2\times2}$ for the full–order observer and $l_{11} = 1$, $l_{21} = 600$, $K_{s11} = 5$, $K_{s21} = 600$, $K_p = 22.1I_{2\times2}$, $K_d = 9.4I_{2\times2}$ for the sliding–mode observer. K_δ and $K_{\dot{\delta}}$ were 0 and $0.2B^{-1}$, respectively for the full–order observer but were chosen as 0 and $0.1B^{-1}$ for the case with the sliding–mode observer. The choice of K_δ and $K_{\dot{\delta}}$ in this way is first to ensure that $A_\Delta(q)$ given by 4.24 is Hurwitz and second to ensure that these terms are not too large in 4.6 as this will destabilize the closed–loop system.

It is observed from all the figures that even after the 3 second quintic trajectory is over there is some control activity. This is due to the gravity effects that bend the link at the stopping point and result from the compensation provided by the controller.

For the reduced–order observer, the closed–loop system became unstable when G was increased. Similar results were obtained for the other two observers. This can be attributed to the increased noise sensitivity for higher gains. In the sliding–mode observer the ratio K_{s21}/K_{s11} had to be chosen sufficiently large for system stability. This is mainly due to the fact that on the sliding patch the disturbance terms have

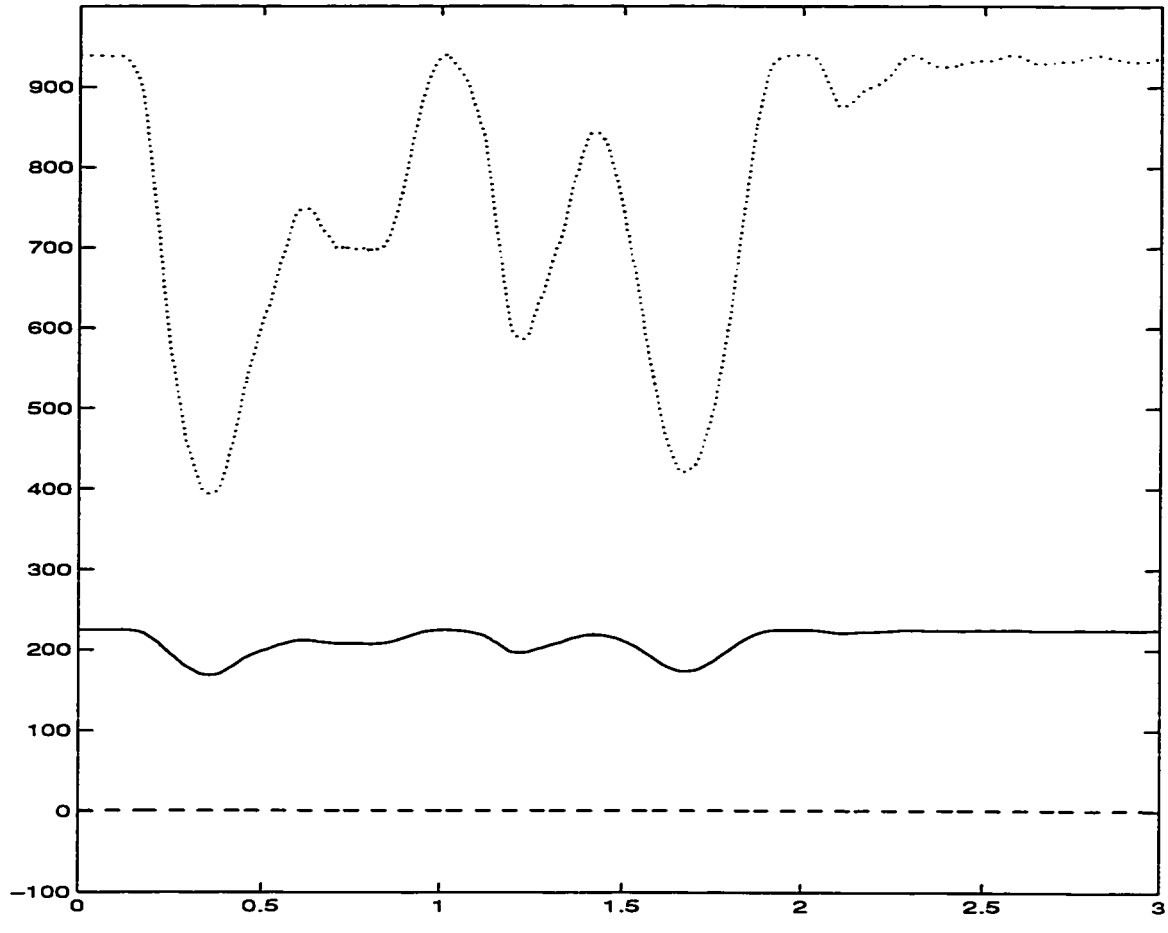

Figure 4.4: Condition number of the mass matrix vs time (s) for the flexible arm: Two mode model ($\cdots$), one mode model (—), rigid model ($- - -$).

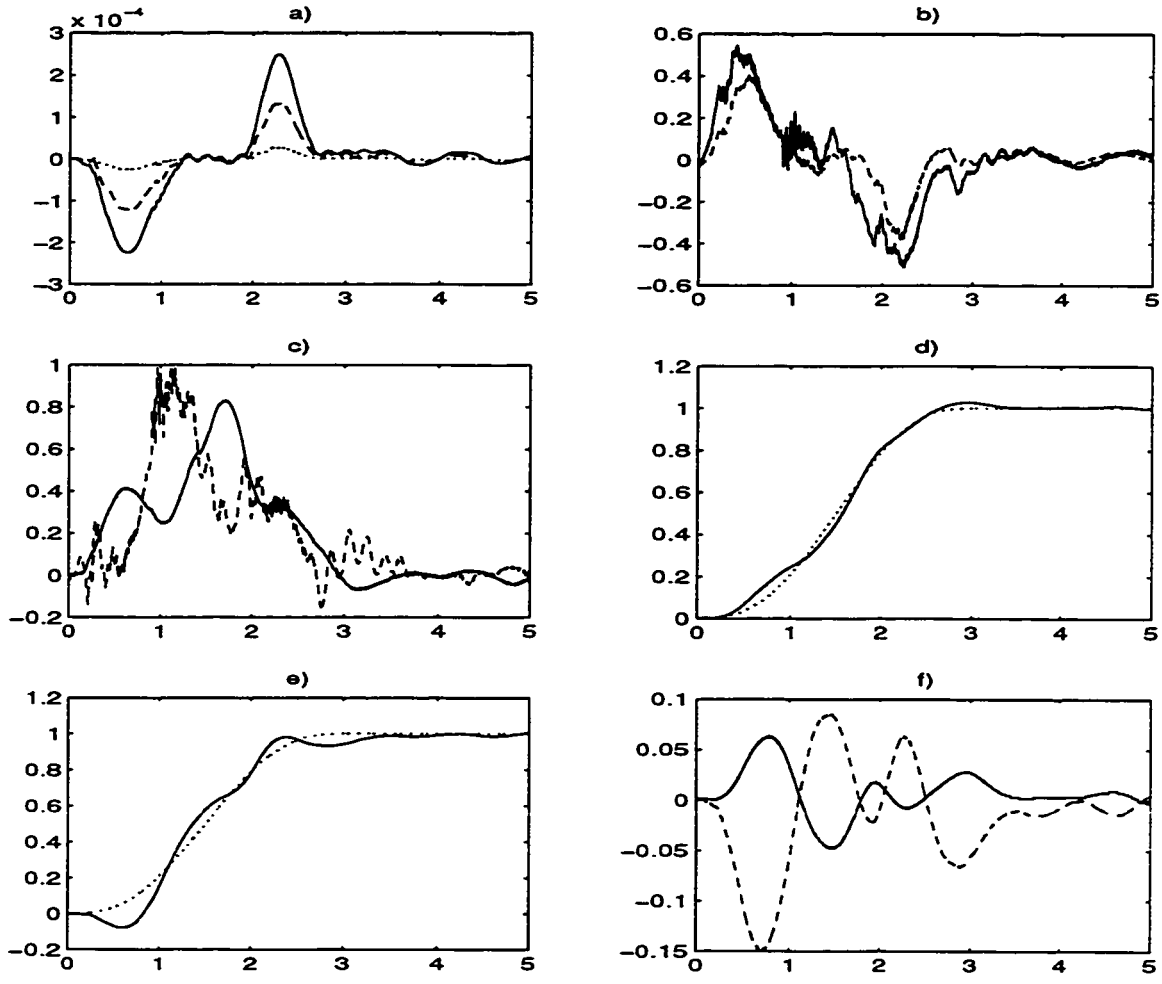

Figure 4.5: Experimental results using the reduced–order observer ($x - axis$: time (s)). a) Strain measurements at points 1 (—), 2 (– –), and 3 ($\cdots$) (m/m) b) Actuator inputs (Nm): 1 (—), 2 (– –) c) Joint velocities (rad/s): 1 (—), 2 (– –) d) First joint angle (—) and desired trajectory ($\cdots$) (rad) e) Second link tip angle (—) and desired trajectory ($\cdots$) (rad) f) Trajectory tracking errors (rad): 1 (—), 2 (– –).

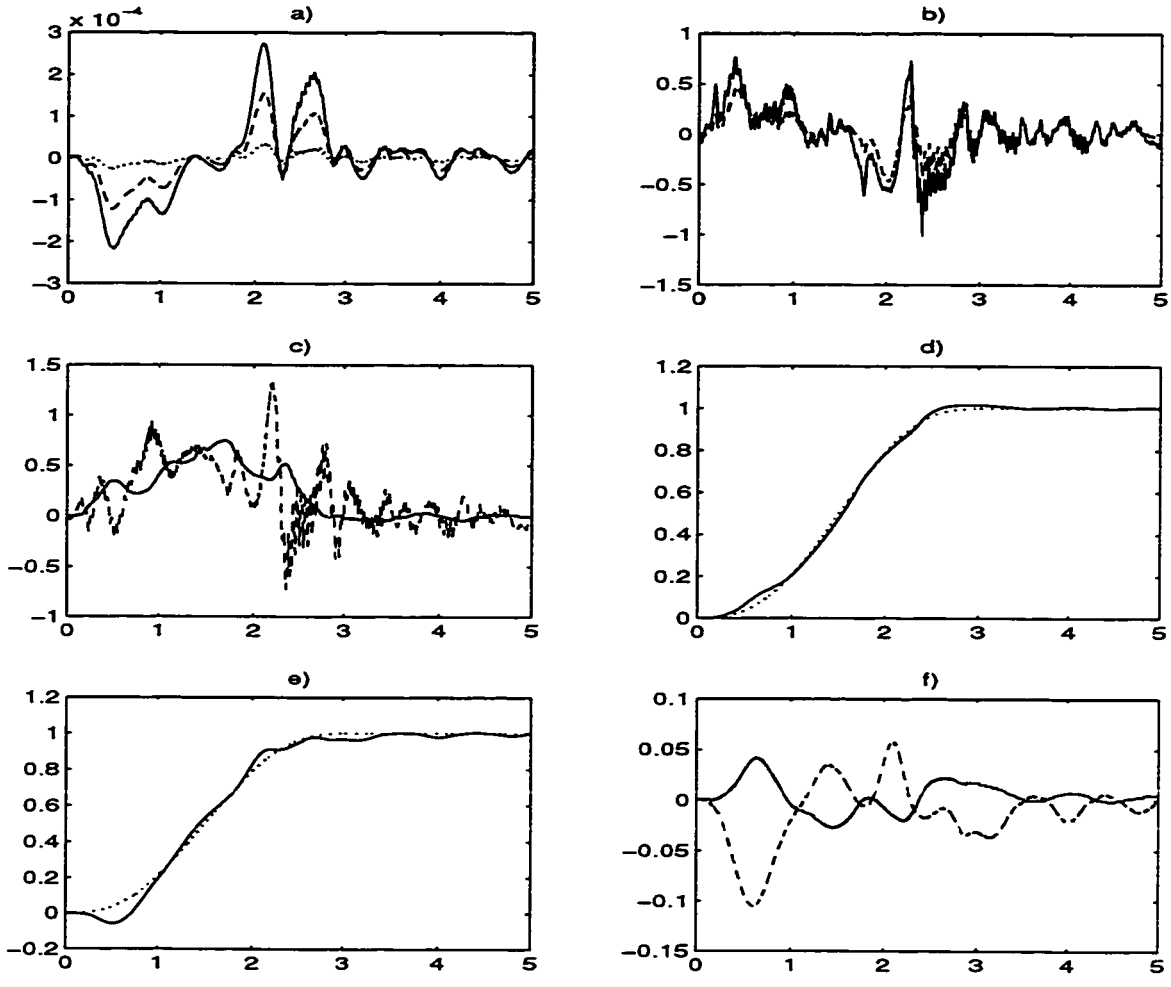

Figure 4.6: Experimental results using the full–order observer ($x - axis$: time (s)). a) Strain measurements at points 1 (—), 2 (– –), and 3 ($\cdots$) (m/m) b) Actuator inputs (Nm): 1 (—), 2 (– –) c) Joint velocities (rad/s): 1 (—), 2 (– –) d) First joint angle (—) and desired trajectory ($\cdots$) (rad) e) Second link tip angle (—) and desired trajectory ($\cdots$) (rad) f) Trajectory tracking errors (rad): 1 (—), 2 (– –).

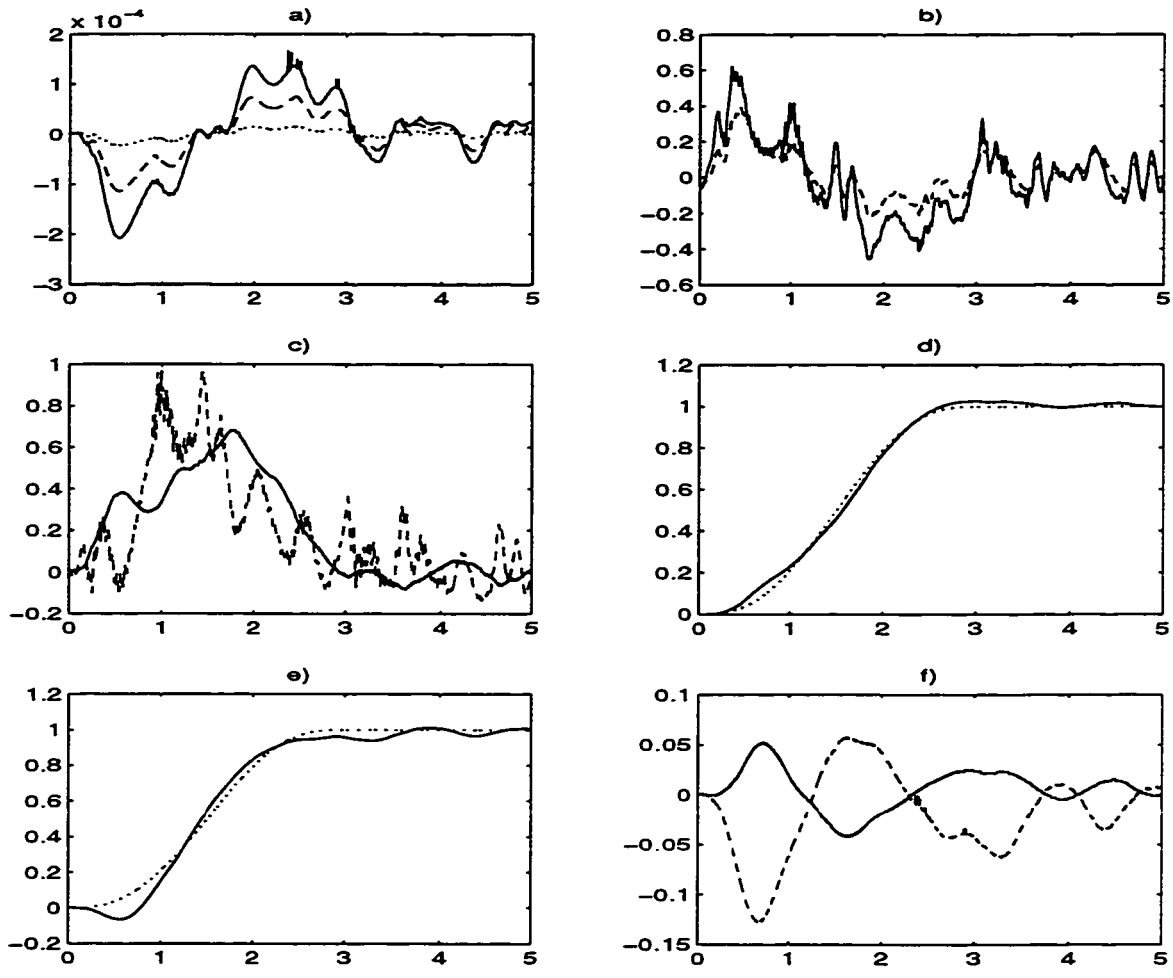

Figure 4.7: Experimental results using the sliding-mode observer ($x - axis$: time (s)). a) Strain measurements at points 1 (—), 2 (– –), and 3 ($\cdots$) (m/m) b) Actuator inputs (Nm): 1 (—), 2 (– –) c) Joint velocities (rad/s): 1 (—), 2 (– –) d) First joint angle (—) and desired trajectory ($\cdots$) (rad) e) Second link tip angle (—) and desired trajectory ($\cdots$) (rad) f) Trajectory tracking errors (rad): 1 (—), 2 (– –).

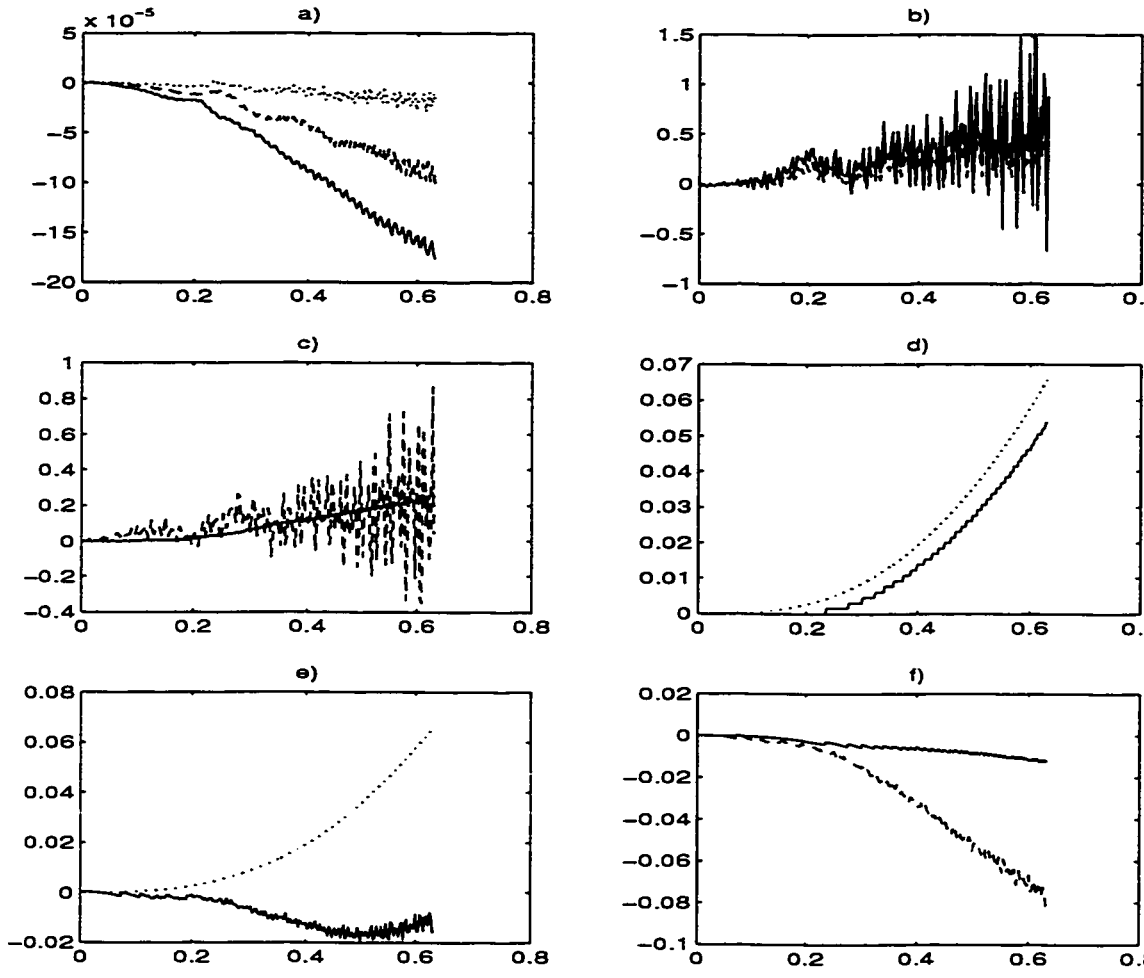

Figure 4.8: Unstable experimental results using conventional inverse dynamics PD controller ($x - axis$: time (s)). a) Strain measurements at points 1 (—), 2 (– –), and 3 ($\cdots$) (m/m) b) Actuator inputs (Nm): 1 (—), 2 (– –) c) Joint velocities (rad/s): 1 (—), 2 (– –) d) First joint angle (—) and desired trajectory ($\cdots$) (rad) e) Second link tip angle (—) and desired trajectory ($\cdots$) (rad) f) Trajectory tracking errors (rad): 1 (—), 2 (– –).

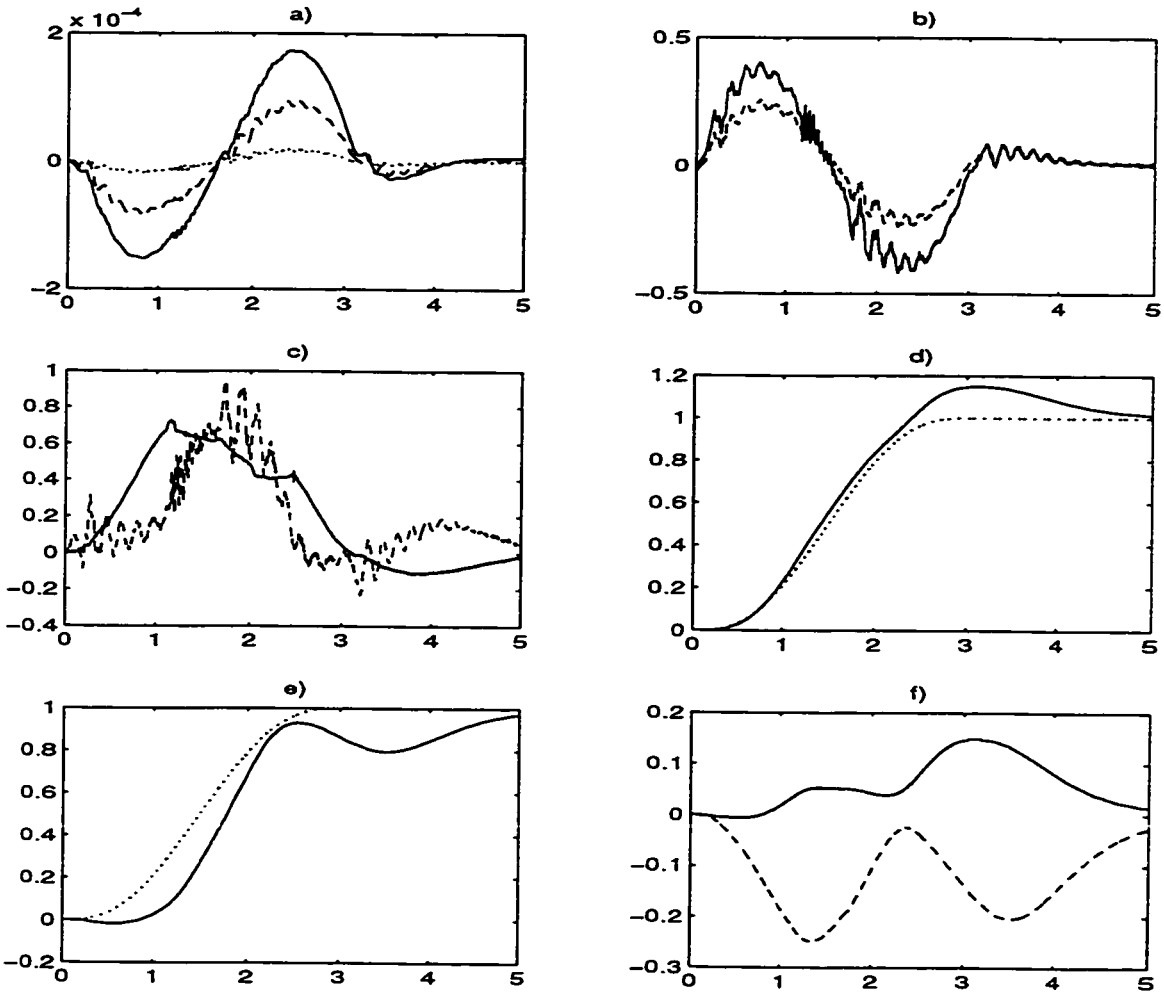

Figure 4.9: Experimental results using conventional inverse dynamics PD controller with reduced gains ($x - axis$: time (s)). a) Strain measurements at points 1 (—), 2 (– –), and 3 ($\cdots$) (m/m) b) Actuator inputs (Nm): 1 (—), 2 (– –) c) Joint velocities (rad/s): 1 (—), 2 (– –) d) First joint angle (—) and desired trajectory ($\cdots$) (rad) e) Second link tip angle (—) and desired trajectory ($\cdots$) (rad) f) Trajectory tracking errors (rad): 1 (—), 2 (– –).

to be rejected. Moreover, the operation of the controller was associated with control chattering. Although the bandwidths of the actuators were small enough not to pass the high frequency chattering signals, the operation of the closed–loop system was more oscillatory than the other observers. The problem was resolved by replacing the $sgn(.)$ with a saturation nonlinearity of the following form with $\varepsilon = .05$

$$sat(x,\varepsilon) = \begin{cases} 1 & x > \varepsilon \\ x/\varepsilon & -\varepsilon \leq x \leq \varepsilon \\ -1 & x < -\varepsilon \end{cases}$$

Overall, the full–order observer was found to result in a better closed–loop performance with little tuning of the control and observer gains.

Figures 4.8 and 4.9 show the experimental results with the conventional computed torque PD control when the effects of flexibility are neglected in the plant model. This is done to assess the performance improvement of the proposed scheme over a conventional method. Figure 4.8 corresponds to the case when the same K_p and K_p are used as before. The control input was disconnected due to instability of the closed–loop system. On the other hand, reducing the gains to $K_p = 1$ and $K_d = 2$ results in large tracking errors and increased sensitivity of the closed–loop system to uncertainties as shown in Figure 4.9.

Due to several factors the tracking errors are not as small as those predicted by simulations which were run in the absence of modeling imperfections, actuator dynamics, discretization effects, sensor noise, and computational delay of the control law.

4.6 Conclusion

A control strategy based on nonlinear inversion was proposed for a class of structurally flexible robot manipulators and experimentally tested on a two–arm flexible

setup. Three observation strategies were also introduced to estimate the rates of change of flexible modes that are not conveniently or economically accessible. The observation strategies are applicable to the general case of flexible robots and tend to cancel certain nonlinear terms that are present in the dynamic equations so that linear observation error dynamics are obtained. The flexible robot was also tested with a conventional control method based on rigid–link inverse dynamics PD control. The proposed scheme shows promising results for stable and small tip position tracking error performance.

Chapter 5

Inverse Dynamics Sliding Control

In this chapter, we modify the control strategy based on dynamic inversion discussed in the last two chapters such that a more robust performance is achieved in the presence of considerable parametric uncertainties. Motivated by the concept of a *sliding surface* in variable structure control (*VSC*) [75], a robustifying term is developed to drive the nonlinear plant's error dynamics onto a sliding surface. On this surface, the error dynamics are then independent of parametric uncertainties. In order to avoid over–excitation of higher frequency flexural modes due to control chattering, the discontinuous functions normally used in classical *VSC* are replaced by saturation nonlinearities at the outset. This also facilitates analysis by the standard Lyapunov techniques. The controller performance is demonstrated by simulation on a two–link flexible manipulator with considerable amount of parametric uncertainty.

5.1 Introduction

Because of the infinite dimensional nature of the dynamics of flexible–link manipulators and in order to obtain less complicated models for control design, approximations are usually made in the modeling phase. These approximations may be the source of parametric uncertainties which may in turn lead to poor or unstable

performance. Payload variations can also significantly change the dynamic equations hence causing similar problems. One way to deal with this issue is employing concepts from variable structure control [75], [76] which features excellent robustness properties in the face of parametric uncertainties. This has been successfully applied for trajectory tracking control of rigid robot manipulators [77]. In the case of flexible–link manipulators, one has to deal with the non–minimum characteristic of the plant and to ensure that the control law is smooth enough not to over excite higher flexural modes of the plant.

Control design based on sliding surfaces is considered in this chapter. By defining a desired sliding surface and partitioning the control input, a control law is developed to ensure attractiveness of the surface, boundedness of the flexible modes, and tracking of the re–defined outputs. For simplicity we assume that all the states are available for control. Obviously the observer structure introduced in Chapter 4 may be employed to obtain flexural rates if desired.

A similar closed–loop stability analysis is performed and conditions for achieving stable closed–loop behavior are derived. The control scheme is further tested by a numerical simulation for a two–link flexible manipulator.

5.2 Control Based on Input–Output Linearization

Let us consider the control strategy discussed in section 4.2. Assuming that the nominal vector $a_n(x)$ and matrix $B_n(\alpha, q, \delta)$, representing $a(\alpha, x)$ and $B(\alpha, q, \delta)$ respectively, are at our disposal, (4.3) can be written as

$$\ddot{y} = a_n(x) + B_n(q, \delta)u + \eta(x, u) \tag{5.1}$$

where $\eta(x, u) = \Delta a(x) + \Delta B(q, \delta)u$ and $\Delta a(x) = a(\alpha, x) - a_n(x)$, $\Delta B(q, \delta) = B(q, \delta) - B_n(q, \delta)$. Let us define a desired trajectory profile y_r, $\dot{y}_r$, and $\ddot{y}_r$, the

tracking errors $e = y_r - y$ and $\dot{e} = \dot{y}_r - \dot{y}$, and an additional state $e_I = \int_0^t e\, dt$. Then in the $3n$–dimensional space of $(e_I, e, \dot{e})$ define a *linear* n–dimensional switching surface

$$\sigma = K_p e_I + K_d e + \dot{e} \tag{5.2}$$

where K_p and K_d are positive–definite matrices that, as will be seen later, determine the error dynamics in the sliding mode. Our goal is to design a control law such that two conditions are satisfied: First, on the sliding (switching) surface the dynamics are independent of the uncertainties, and second, the surface is an attractive manifold. As discussed in [80] in order to obtain smooth action let us define a boundary layer around the switching surface σ and measure the distance of each point to this surface by

$$s_\sigma = \sigma - \Phi sat(\frac{\sigma}{\Phi}) \tag{5.3}$$

Then inside the boundary layer, s_σ and $\dot{s}_\sigma$ are zero, while outside the boundary layer we have

$$\dot{s}_\sigma = \ddot{e} + K_d \dot{e} + K_p e \tag{5.4}$$

Substituting $\ddot{y}$ from (5.1) in (5.4) yields

$$\dot{s}_\sigma = \ddot{y}_r + K_d \dot{e} + K_p e - a_n(x) - B_n(q, \delta)u - \eta(x, u) \tag{5.5}$$

Let us partition the control input as

$$u = u_n + u_u + u_\Delta \tag{5.6}$$

where u_n is the nominal control, u_u is to provide more robustness to uncertainties, and $u_\Delta = K_\delta(q)\delta + K_{\dot{\delta}}\dot{\delta}$, as will be seen later, guarantees boundedness of δ and $\dot{\delta}$.

Assuming that the nominal $B_n(q, \delta)$ is nonsingular on the domain of interest, let us take

$$u_n = B_n^{-1}(q, \delta)(-a_n(x) + \ddot{y}_r + K_d \dot{e} + K_p e) \tag{5.7}$$

Then substitution of (5.7) in (5.5) yields

$$\dot{s}_\sigma = -B_n u_u - \eta(x,u) \tag{5.8}$$

Thus to make s_σ an attractive manifold in the presence of parametric uncertainties let us choose

$$u_u = -B_n^{-1} K sat(\Gamma s_\sigma) \tag{5.9}$$

where $K = diag(k_1, \cdots, k_n)$, $\Gamma = diag(\gamma_1, \cdots, \gamma_n)$ and $sat(.)$ is the saturation vector function. Substituting (5.9) in (5.8) yields

$$\dot{s}_\sigma = K sat(\Gamma s_\sigma) - \eta(x,u) \tag{5.10}$$

Note that u is now a function of x, s_σ, t, or equivalently a function of e, $\dot{e}$, δ, $\dot{\delta}$, s_σ, t. Consider a bounded reference trajectory and e, $\dot{e}$, δ, and $\dot{\delta}$ inside a closed bounded set $\Omega^* \subset R^{2n+2m}$ then

$$\dot{s}_\sigma = K sat(\Gamma s_\sigma) + \Delta B^* K sat(\Gamma s_\sigma) + \eta^*(e,\dot{e},\delta,\dot{\delta}) \tag{5.11}$$

where $\Delta B^* = \Delta B B_n^{-1}$ and

$$\eta^*(e,\dot{e},\delta,\dot{\delta}) = -\Delta a(x) - \Delta B^*(-a_n + \ddot{y}_r + K_d\dot{e} + K_p e) - \Delta B(K_\delta(q)\delta + K_{\dot{\delta}}\dot{\delta}) \tag{5.12}$$

Representing the elements of ΔB^* by ΔB^*_{ij}, (5.11) can be written as

$$\dot{s}_{\sigma_i} = (1 + \Delta B^*_{ii}) k_i sat(\gamma_i s_{\sigma_i}) + \sum_{j=1, j\neq i}^{n} \Delta B^*_{ij} k_j sat(\gamma_j s_{\sigma_j}) + \eta^*_i, \quad i = 1, \cdots, n \tag{5.13}$$

Now for all $(e,\dot{e},\delta,\dot{\delta}) \in \Omega^*$ assume that $\mid \Delta B^*_{ij} \mid \leq b_{ij}$ and $\eta^*_i \leq c_i$. Hence for all $s_{\sigma_i} \in R$ the sliding conditions can be individually ensured [66] if

$$s_{\sigma_i}\dot{s}_{\sigma_i} \leq -\beta_i \mid s_{\sigma_i} \mid, \quad \beta_i > 0, \quad i = 1, \cdots, n \tag{5.14}$$

Noting that $s_{\sigma_i} sat(\gamma_i s_{\sigma_i}) \leq \mid s_{\sigma_i} \mid$ it follows from (5.13) that (5.14) can be ensured under worst case conditions if k_i's are such that

$$(1 - b_{ii})k_i - \sum_{j=1, j\neq i}^{n} b_{ij}k_j - c_i \geq \beta_i \tag{5.15}$$

Considering the equality sign in (5.15) we have the matrix equation $(I - B^*)k^* = d$ where B^* is the matrix with elements b_{ij} and d is the vector with elements $c_i + \beta_i > 0$. Following Frobenius–Perron theorem (see e.g. [66]) a unique solution for k^* can be guaranteed with all its elements positive if the largest real eigenvalue of B^* is less than 1. In particular, if b_{ij}'s are chosen such that B^* is symmetric, the eigenvalue condition translates into the norm condition $\|B^*\|_2 < 1$. Moreover, if such a solution exists for k^*, choosing the elements of k larger than k^* will result in larger β_i's, hence speeding up attraction when the trajectories are outside $s_{\sigma_i} = 0$.

5.2.1 Stability of the Closed–Loop System

To prepare for a stability analysis of the closed–loop system with the aforementioned control laws, let us first substitute (5.6) into (5.1) by utilizing (5.7) and (5.9). Then arranging the expressions in terms of e and $\dot{e}$ yields

$$\dot{E} = A_E E + d_E(E, \Delta, s_\sigma, t) \tag{5.16}$$

where $E^T = [e^T \;\; \dot{e}^T]$, $\Delta^T = [\delta^T \;\; \dot{\delta}^T]$, $d_E(.) = [0^T \;\; D_E^T(.)]^T$ and

$$\begin{aligned} d_E(E, \Delta, s_\sigma, t) &= -(I + \Delta B) K sat(\Gamma s_\sigma) + (B_n + \Delta B)(K_\delta(q)\delta + K_{\dot{\delta}}\dot{\delta}) \\ &+ \Delta B B_n^{-1}(-a_n + \ddot{y}_r + K_p e + K_d \dot{e}) \end{aligned} \tag{5.17}$$

and A_E is a Hurwitz matrix given by

$$A_E = \begin{bmatrix} 0 & I \\ -K_p & -K_d \end{bmatrix} \tag{5.18}$$

For the part of dynamics due to the flexible modes, starting from (4.3) and substituting u will lead after some manipulations to

$$\begin{aligned} \ddot{\delta} &= -[H_{22} - H_{21}B^{-1}(H_{21} + \Psi H_{22}](f_2 + g_2 + K\delta) + H_{21}(B^{-1}a - B_n^{-1}a_n) \\ &+ H_{21}B_n^{-1}(\ddot{y}_r + K_p e + K_d \dot{e} - K sat(\Gamma s_\sigma)) + H_{21}(K_\delta(q)\delta + K_{\dot{\delta}}(q)\dot{\delta}) \end{aligned} \tag{5.19}$$

Equation (5.19) is strongly linear in terms of δ and $\dot{\delta}$. Thus expanding the terms around $\delta = 0$ and $\dot{\delta} = 0$ results in

$$\dot{\Delta} = A_\Delta(q)\Delta + g_\Delta(E, \Delta, s_\sigma, t) \tag{5.20}$$

where $g_\Delta = [0^T \;\; G_\Delta^T]^T$ and

$$\begin{aligned} A_\Delta(q) &= \begin{bmatrix} 0 & I \\ -P(q)K - H_{210}K_\delta(q) & -H_{210}K_{\dot{\delta}}(q) \end{bmatrix} \\ P(q) &= [H_{220} - H_{210}(H_{110} + \Psi H_{210})^{-1}(H_{120} + \Psi H_{220})] \end{aligned} \tag{5.21}$$

where $H_{ij0} = H_{ij}(q, \delta = 0)$ $(i, j = 1, 2)$. Moreover G_Δ is given by

$$\begin{aligned} G_\Delta(E, \Delta, s_\sigma, t) &= H_{21}B_n^{-1}(\ddot{y}_r + K_p e + K_d \dot{e} - Ksat(\Gamma s_\sigma)) \\ &+ H_{21}(B^{-1}a - B_n{}^{-1}a_n) + O(\delta, q, \dot{q}) \end{aligned} \tag{5.22}$$

The reason for writing this portion of the dynamics in the form just described is that (5.20) can be shown to be related to the zero–dynamics of the system with re–defined outputs which is made stable by an appropriate choice of the outputs and matrices $K_\delta(q)$ and $K_{\dot{\delta}}(q)$ [69].

The stability proof can then be achieved by considering the composite Lyapunov function candidate

$$V = E^T P_E E + \epsilon_\Delta^2 \Delta^T P_\Delta(q)\Delta + 0.5 s_\sigma^T s_\sigma \tag{5.23}$$

and finding the derivative of V along the trajectories of the system. This analysis is further detailed in Appendix A.4 and results in the following theorem

Theorem 5.1 *Let the control law (5.6) be applied to the original nonlinear system (4.1) with $B_n(q, \delta)$ nonsingular and let the flexible dynamics given by (5.20) be controlled by choice of $K_\delta(q)$ and $K_{\dot{\delta}}(q)$ on the domain of interest. Consider sets $\mathcal{R}$, $\mathcal{S}$ and $\mathcal{T}$ given by (A.48). Then assuming that the desired trajectories and*

their time derivatives (at least up to order 2) are continuous and bounded, it follows that the trajectories of E, $\epsilon_\Delta \Delta$ and s_σ (ϵ_Δ is a small scaling factor as discussed in Appendix A.4), starting from $\mathcal{S} - \mathcal{R}$ converge to a residual set $\mathcal{T}$ that can be made small by proper choice of controller parameters, provided that d_E and g_Δ given in (5.16), (5.20) satisfy certain norm conditions ((A.44), (A.45)) in a bounded region Ω_i (given in Appendix A.4) of the state space of (E, Δ, s_σ) containing the origin.

Proof: The proof of the above result is established in Appendix A.4.

5.2.2 Numerical Simulation

In this section the controller performance is tested using a numerical simulation for the model of the two–link experimental setup that was discussed in section 4.5 (Figure 4.3).

The nominal model used in the numerical simulation is based on the case where no payload is attached at the end point while the plant model is based on the full payload of $251kg$. This results in a significant difference between the parameter values of these models (of order of 2–6 times). Figure 5.1 shows the simulation results for $K = 6000$, $\Gamma = 2I$, $K_p = 1$, $K_d = 2$, $\Phi = 1.7 \times 10^{-4}$, $K_\delta = 0$ and $K_{\dot{s}} = 1$. The output of the first link was the joint angle while for the second link the output was chosen as the pseudo–angle corresponding to the point at $0.80L_2$ (L_2 is the length of the second link). It is observed that the tracking errors are small. Several other simulations were also performed by changing the gain parameter values and similar results were obtained. To compare the performance of the sliding controller introduced in this chapter with the control strategy in Chapter 3 similar simulations were performed. The closed–loop system consisted of a control law based on a plant model with zero payload while the actual plant model was based on a payload of $0.251kg$. The closed–loop system was unstable despite various changes made in

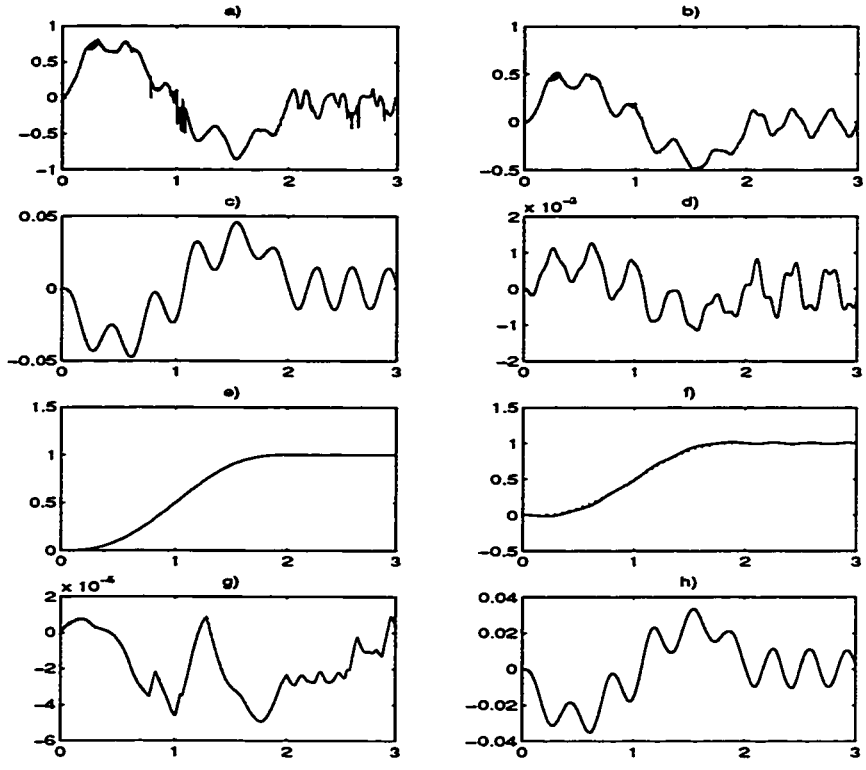

Figure 5.1: Simulation results for a flexible two–link manipulator using the proposed controller (Horizontal axis: time (s)): a) First joint torque input (Nm) b) Second joint torque input (Nm) c) First flexible mode (m) d) Second flexible mode (m) e) First joint angle (—) and reference trajectory (···) (rad) f) Tip position of second link (—) and reference trajectory (···) (rad) g) Tracking error of the first link joint position (rad) h) Tip position tracking error of the second link (rad).

controller gains. This result further demonstrates that the sliding controller is more robust than the controller introduced in Chapter 3 when parametric uncertainties are significant.

5.3 Conclusion

The decoupling control strategy discussed in chapters 3 was modified by using the concept of sliding surfaces so that more robustness to parametric uncertainties is achieved. Two main factors contribute to the robust performance of the closed–loop

system in this case: The input–output linearization that tends to approximately decouple the dynamics, and the sliding control component that causes the off–manifold trajectories to be attracted to the surface. Full state measurements were necessary in the developed scheme; however, in a practical situation $\dot{\delta}$ can be estimated by using a nonlinear observer as described in Chapter 4.

Chapter 6

Optimum Structure Design for Control

In this chapter, an optimum structure design methodology is proposed for improving the dynamic behavior of structurally flexible manipulators. The improvement in the dynamic behavior is achieved through an optimization scheme where a cost function associated with the lowest natural flexible mode and an index defined as *modal accessibility*, is optimized subject to certain constraints. The formulations are carried out by assuming a singularly perturbed model of the flexible–link system as this system possesses two–time scale properties. The methodology is then applied to design a two–link, non–uniform, planar, flexible manipulator with improved performance characteristics as compared to a uniform manipulator.

6.1 Introduction

In every control problem, the designer is concerned with devising control laws that provide appropriate operation of the closed–loop system. A basic philosophy that has been pursued by systems and control engineers for some time encourages designers to alter the plant characteristics whenever feasible so that less stringent control

actions will be required (e.g. in aircraft and other complex navigational systems). The same philosophy may be applied to the case of robotic manipulators. The design process regarding arm shape design to achieve characteristics such as low mass and moments of inertia and high natural frequencies generally requires solution of an optimization problem, such as the one introduced in [21] where the optimum torque application point and structural shape for a single flexible arm have been obtained. There are a few other published works in this area (e.g. [82], [22]) that address the design problem for a single–link flexible arm without its extension to the case of multi–body dynamics. Parallel to this line of research, the use of advanced and intelligent materials in arm construction is worth mentioning [28].

In this chapter, a design methodology is proposed for improving the dynamic behavior of structurally flexible manipulators. The improvement in the dynamic behavior is formulated as an optimization problem so that the lowest natural flexible mode and an index defined as *modal accessibility* are optimized. The term *modal accessibility* is adopted from [34] where, in certain robot configurations denoted as inaccessible robot positions, one or more of the flexibilities may not be accessed directly by the actuators. This condition may significantly deteriorate system performance and may even cause instability. This issue is not currently incorporated in structural design in the published literature. Moreover, an increase in the lowest natural frequency of the flexible system is often desirable. Undoubtedly, these improvements should be achieved without sacrificing the system's inertia characteristics.

The organization of this chapter is as follows. In section 5.2, the optimization problem is formulated in general by employing a singular perturbation model of the flexible–link system. In section 5.3, further details are discussed in the design of a flexible two–link planar manipulator. Also in section 5.3, the results of different optimization procedures are given and compared by examples of two–link structures.

6.2 Statement of the Problem

The optimization problem is formulated within the context of singular perturbation theory [81], due to the fact that the dynamics of flexible–link manipulators exhibit two–time–scale properties. To this end, consider the dynamic equations of the manipulator (see e.g. [8])

$$\begin{aligned}\ddot{q} &= -H_{11}(q,\delta)(f_1(q,\dot{q}) + g_1(q,\dot{q},\delta,\dot{\delta})) \\ &- H_{12}(q,\delta)(f_2(q,\dot{q}) + g_2(q,\dot{q},\delta,\dot{\delta})) - H_{12}(q,\delta)K\delta + H_{11}(q,\delta)u \qquad (6.1)\\ \ddot{\delta} &= -H_{21}(q,\delta)(f_1(q,\dot{q}) + g_1(q,\dot{q},\delta,\dot{\delta})) \\ &- H_{22}(q,\delta)(f_2(q,\dot{q}) + g_2(q,\dot{q},\delta,\dot{\delta})) - H_{22}(q,\delta)K\delta + H_{21}(q,\delta)u \qquad (6.2)\end{aligned}$$

where $q \in \mathbf{R^n}$ is the vector of joint position variables, $\delta \in \mathbf{R^m}$ is the vector of flexible modes, f_1, f_2, g_1, and g_2 are the terms due to gravity, Coriolis, and centripetal forces, H is the inverse of the positive–definite mass matrix M with $M_{i,j}, H_{i,j}$, $i,j = 1,2$, being the submatrices corresponding to the vectors q and δ, and K is the positive definite stiffness matrix. As is Chapter 2 let us define the variables

$$x_1 = q, \qquad x_2 = \dot{q}, \qquad z_1 = \frac{\delta}{\varepsilon^2}, \qquad z_2 = \frac{\dot{\delta}}{\varepsilon} \qquad (6.3)$$

where ε is the singular perturbation parameter defined as

$$\varepsilon^2 = \frac{1}{\underline{\lambda}_{min}(H_{220}K)} \qquad (6.4)$$

In (6.4), $\underline{\lambda}_{min}(H_{220}K)$ is the lower bound of the minimum eigenvalue of $H_{22}K$ evaluated at $\delta = 0$ (i.e. $H_{220} = H_{22}(q,0)$) over the range in which q varies. The system described by (6.2) may then be written as

$$\begin{aligned}\dot{x}_1 &= x_2 \\ \dot{x}_2 &= a(x_1,x_2,\varepsilon^2 z_1,\varepsilon z_2) - A(x_1,\varepsilon^2 z_1)z_1 + H_{11}(x_1,\varepsilon^2 z_1)u \qquad (6.5)\\ \varepsilon\dot{z}_1 &= z_2 \\ \varepsilon\dot{z}_2 &= b(x_1,x_2,\varepsilon^2 z_1,\varepsilon z_2) - B(x_1,\varepsilon^2 z_1)z_1 + H_{21}(x_1,\varepsilon^2 z_1)u \qquad (6.6)\end{aligned}$$

where $x_1, x_2 \in \mathbf{R^n}$, $z_1, z_2 \in \mathbf{R^m}$ and

$$\begin{aligned} a(x_1, x_2, \varepsilon^2 z_1, \varepsilon z_2) &= -H_{11} f_1 - H_{12} f_2 - H_{11} g_1 - H_{12} g_2 \\ b(x_1, x_2, \varepsilon^2 z_1, \varepsilon z_2) &= -H_{21} f_1 - H_{22} f_2 - H_{21} g_1 - H_{22} g_2 \\ A(x_1, \varepsilon^2 z_1) &= \frac{H_{12}(x_1, \varepsilon^2 z_1) K}{\underline{\lambda}_{min}(H_{220} K)} \\ B(x_1, \varepsilon^2 z_1) &= \frac{H_{22}(x_1, \varepsilon^2 z_1) K}{\underline{\lambda}_{min}(H_{220} K)} \end{aligned} \tag{6.7}$$

In the above formulation, let us adopt a composite control strategy [1] [44] , i.e.,

$$u = u_f + u_0 \tag{6.8}$$

In (6.8), u_0 is the rigid body or *slow* control law, and u_f is the *fast* control law that acts whenever the system behavior deviates from the rigid body dynamics. The system described by (6.5)–(6.6) may be decomposed into the *quasi–steady–state slow* subsystem

$$\begin{aligned} \dot{\bar{x}}_1 &= \bar{x}_2 \\ \dot{\bar{x}}_2 &= M_{11}^{-1}(x_1, 0)(-f_1(\bar{x}_1, \bar{x}_2) + u_0) \end{aligned} \tag{6.9}$$

and the *boundary layer fast* subsystem

$$\begin{aligned} \frac{d\tilde{z}_1}{d\tau} &= \tilde{z}_2 \\ \frac{d\tilde{z}_2}{d\tau} &= -\frac{H_{220} K}{\underline{\lambda}_{min}(H_{220} K)} \tilde{z}_1 + H_{210} u_f \end{aligned} \tag{6.10}$$

where

$$\begin{aligned} \tilde{z}_1 &= z_1 - \bar{z}_1 \\ \tilde{z}_2 &= z_2 - \bar{z}_2 \\ \bar{z}_1 &= B^{-1}(x_1, 0)(b(x_1, x_2, 0, 0) + H_{210} u_0) \\ \bar{z}_2 &= 0 \end{aligned} \tag{6.11}$$

[1] Intuitively, other control schemes may be considered as comprising two parts, that is, slow control for rigid body motion and fast control to compensate for the effects of elastic vibrations.

Now if the fast subsystem (6.10) is properly stabilized, then (6.9) describes the rigid–link manipulator dynamics, and is a *zeroth order* approximation to the original system (6.5)–(6.6) (cf. [81], [42]). Let us consider (6.10) and re–write it in the following form

$$\frac{d^2\tilde{z}_1}{d\tau^2} = -N_o\tilde{z}_1 + H_{210}u_f \tag{6.12}$$

where

$$N_o = N_o(x_1) = \frac{H_{220}K}{\underline{\lambda}_{min}(H_{220}K)} \tag{6.13}$$

Consider the eigenvalue problem

$$N_o v_i = \omega_i^2 v_i, \quad i = 1,\ 2,\ \cdots,\ m \tag{6.14}$$

where w_i^2 is the i–th eigenvalue of the positive–definite matrix N_o, and v_i is the associated eigenvector. Using the transformation $\tilde{z}_1 = V_o y$, where V_o is a matrix whose columns are v_i's, will transform (6.12) into

$$\ddot{y} = -\Lambda_o y + \Gamma_o u_f \tag{6.15}$$

where

$$\begin{aligned} \Lambda_o(x_1) &= diag(\omega_1^2, \omega_2^2, \cdots, \omega_m^2) \\ \Gamma_o(x_1) &= V_o^{-1} H_{210} \end{aligned} \tag{6.16}$$

The joint variables q (or x_1) are treated as *frozen* (fixed) parameters in the fast time scale (cf. [81], Chapter 2). For this reason the subscript "o" is used to indicate matrices which are functions of q (or x_1). Now consider Γ_o in the decoupled subsystem (6.15). Each row of the $m \times n$ matrix Γ_o characterizes the way the input u_f affects the corresponding eigenvalue associated with that row in Λ_o. Thus, if the Euclidean norm of the i–th row is very small, it implies that ω_i^2 is not affected much by u_f – this is equivalent to requiring a large u_f to affect ω_i^2. The large requirement for u_f is disadvantageous from robustness considerations, as high gains are likely to cause stability problems (cf. Chapter 2). This observation follows from the same lines

as those in [34] and should be distinguished from the controllability property that merely indicates whether system modes can be affected by control inputs without any regard to the magnitude of the control effort. In particular, it may happen that, at certain positions, a robot can maintain full controllability while its flexible modes are inaccessible by its actuators (cf. [34] for more details). This condition may significantly deteriorate system performance and may even cause system instability. Consequently, it is important to incorporate these issues in mechanical structure design of flexible links. Furthermore, to obtain a manipulator that has a Γ_o with relatively high row norms is desirable not only from a control effort minimization point of view, but also from a robustness point of view. Another desirable feature in terms of manipulator dynamics is that the first flexible natural frequency should be well above the operating speeds of the manipulator. Conventional control strategies, in general, work well when the closed–loop bandwidth is well below the first structural frequency of the manipulator. In the context of singular perturbation theory this is equivalent to decreasing ϵ in (6.4) to allow for a better time–scale separation, and a better margin of closed–loop stability when a composite controller is employed [81].

Now suppose that a mechanical design parameter vector p is at our disposal. This vector may comprise of parameters related to the geometry (lengths) of the links, or material properties such as mass density or material modulus of elasticity. Following the discussion above, let us define the following objective function

$$y(q,p) = c_1\sqrt{\lambda_{min}(H_{220}(q,p)K(p))} + c_2\sqrt{trace(\Gamma_o(q,p)W\Gamma_o^T((q,p))} \qquad (6.17)$$

where W is a diagonal positive definite weighting matrix. The first term in (6.17) accounts for the time–scale separation, and the second term accounts for the accessibility of flexible modes by the fast control component. The constraints that may be incorporated in the optimization problem include workspace requirements such as link lengths, and constraints on link masses and the mass moments of inertia experienced by the actuators. The bounds on the constraints should be selected such

that a feasible solution exists. An obvious choice for these bounds may be specified from a manipulator with uniform links. Thus, starting from a parameter vector p_0 corresponding to the case of a uniform manipulator, it is desired to find p such that the objective function

$$Y(p) = \int_q y(q,p)dq \tag{6.18}$$

is maximized subject to the constraints specified earlier. The integral term is taken over the range in which q (the vector of joint variables) is defined for two reasons: First, to obtain a smooth objective function, and second, to ensure that all the points in the workspace are considered in the objective function.

6.3 Formulation of the Optimization Problem for a Two–Link Manipulator

In this section the optimization strategy introduced in the previous section is applied to design a planar two–link manipulator as shown in Figure 6.1. This manipulator is modeled using the assumed modes method and clamped–free mode shapes by employing the symbolic manipulation software *MAPLE* [35]. The details of this derivation are outlined in Appendix C.3. It is assumed that the material type is given (aluminum) and the link shapes are to be designed appropriately. Towards this end, each link is divided into n sections with each section parameters as shown in Figure 6.2. The value of n may be decided from a signal analysis point of view. In particular, considering a specific total length for each link, a large n corresponds to more samples of the link shape which is equivalent to the possibility of *richer* (*higher frequency*) geometric link shapes. However, a *fast–changing* or *high–frequency* link profile may introduce practical manufacturing difficulties. Thus, a compromise should be made between these issues in selecting n. For now it is assumed that $n = 3$. However, the case with larger n will also be addressed later. It is worth pointing out that when n is large there is no need to consider the L_i terms

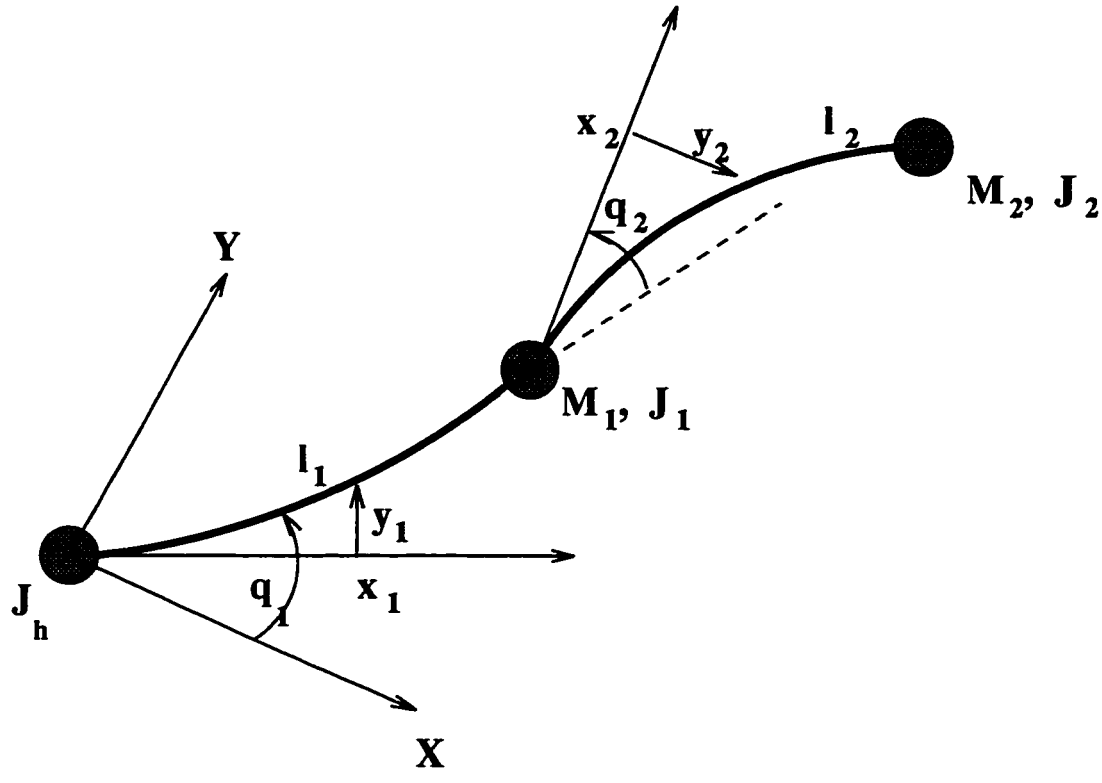

Figure 6.1: The two–link flexible manipulator.

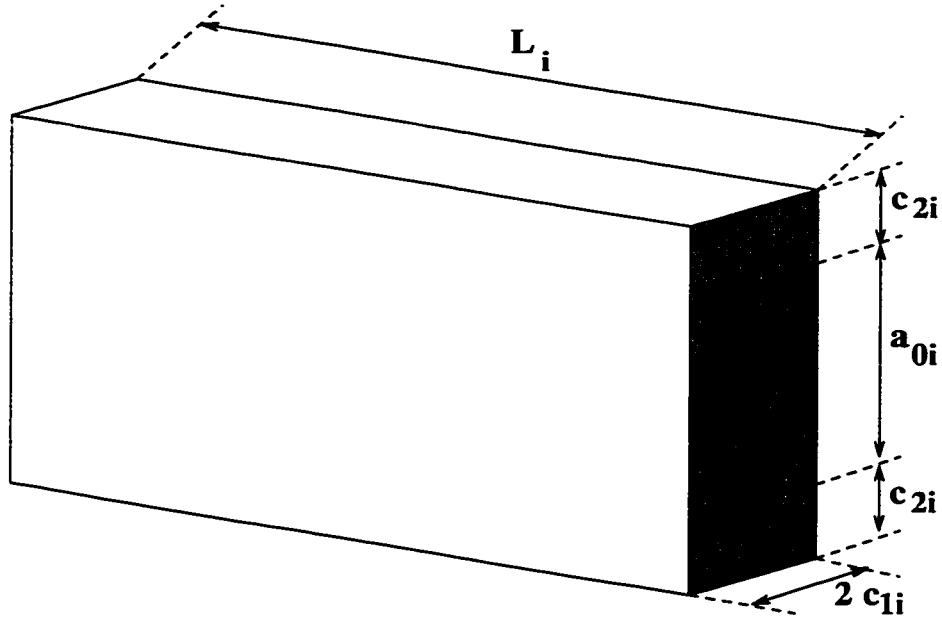

Figure 6.2: Schematic view of section i for each link ($i = 1, 2, \cdots, n$) with appropriate definitions for the parameters L_i, c_{1i} and c_{2i}.

as optimization parameters since c_{1i} and c_{2i} basically define the structural shape. As discussed in section 6.4, it may be more advantageous to employ concepts from spline theory in order to obtain *smoother* link shapes. Lengths L_i, c_{1i}, and c_{2i} of each section are the design parameters. Thus, the parameter vector p described in the previous section consists of 18 variables. To formulate the optimization problem the mass matrix $M(q, \delta)$ (δ is the vector of flexible modes) is first found for three flexible modes for each link using *MAPLE*. The mass matrix thus obtained is only a function of q_2 and δ, and q_1 does not appear in this matrix. Consider q_2 varying from $0°$ to $180°$, and choose three representative points in the workspace at $q_{21} = 30°$, $q_{22} = 90°$, and $q_{23} = 150°$. Define the following objective function (see also (6.17)),

$$Y(p) = \frac{1}{3}\{c_1 \sum_{i=1}^{n} \sqrt{\lambda_{min}(H_{220}(q_{2i}, p)K(p))} + c_2 \sum_{i=1}^{n} \sqrt{trace(\Gamma_o(q_{2i}, p)\Gamma_o^T((q_{2i}, p))}\} \tag{6.19}$$

This objective function is selected based on the guidelines used for the function given by (6.18), but (6.19) requires less computation. The optimization problem may now be summarized as follows

$$\begin{aligned}
&maximize \quad Y(p) \\
&subject\ to: \\
&(i) \qquad l_1 + l_2 = L_T \\
&(ii) \qquad M_T(p) \leq (M_T)\,|_u \\
&(iii) \qquad J_{motor-1}(p, 90°) \leq (J_{motor-1})\,|_u \\
&(iv) \qquad J_{motor-2}(p) \leq (J_{motor-2})_u \\
&(v) \qquad \sum_{i=1}^{n} \sqrt{\lambda_{min}(H_{220}(q_{2i}, p)K(p)} \geq (\sum_{i=1}^{n} \sqrt{\lambda_{min}(H_{220}(q_{2i})K)})\,|_u \\
&(vi) \qquad \sum_{i=1}^{n} \sqrt{trace(\Gamma_o(q_{2i}, p)\Gamma_o^T((q_{2i}, p))} \geq (\sum_{i=1}^{n} \sqrt{trace(\Gamma_o(q_{2i}, p)\Gamma_o^T((q_{2i}, p)))})\,|_u
\end{aligned} \tag{6.20}$$

where M_T is the total mass of the two links and the subscript u denotes that the variable is computed when a uniform manipulator is considered. The first constraint

is an equality constraint that is imposed by workspace requirements. In view of the fact that lower inertia links result in less energy consumption, three constraints are imposed on mass and mass moments of inertia of the links. Thus, constraint (ii) restricts the total mass of the links and constraints (iii) and (iv) specify bounds on the inertia experienced by the motors. The inertia experienced by the first motor $(J_{motor-1})$ is in general given by [1]

$$\begin{aligned} J_{motor-1}(p, q_2) &= J_1 + J_2 + J_h + l_1^2(M_1 + M_2) + l_2^2 M_2 + 2M_2 l_1 l_2 \cos q_2 \\ &+ \int_0^{l_2} \rho A_2(x_2)(l_1^2 + x_2^2 + 2l_1 x_2 \cos q_2) dx_2 \end{aligned} \tag{6.21}$$

Since the sign of the cosine term is indefinite, the q_2 independent terms have been considered in constraint (iii) (i.e. $q_2 = 90°$)) as a measure of the moment of inertia. The second motor experiences a constant moment of inertia. The constraints (v) and (vi) are introduced since, compared to the uniform case, we are interested in achieving improvements in at least one of the terms of (6.19), i.e., higher natural frequency and/or better modal accessibility. These constraints are imposed after experimentally observing that, in some cases (and without constraints v and vi), one of the terms in the objective function is improved whereas the other term is worsened when compared to the uniform case.

Several simulations were carried out to obtain an intuitive understanding of the characteristics of the flexible–link system. First of all, considering the mass matrix of the flexible system, it turns out that as the number of flexible modes is increased in order to have a more accurate representation of the system, the mass matrix becomes more ill–conditioned. This behavior is illustrated in Figure 6.3 by using the following data in the simulations

$$\begin{aligned} J_h &= 3 \times 10^{-5} kgm^2,\ J_1 = J_2 = 2 \times 10^{-3} kgm^2,\ M_1 = 1kg,\ M_2 = 2kg,\ L_T = 1.4m, \\ c_{2i} &= c_{1i} = 0.023m,\ i = 1,\ 2,\ 3 \quad (for\ both\ links) \end{aligned}$$

[1] For simplicity, the effects due to flexible modes are neglected and only the dominant effects due to rigid coordinates are considered in (6.21).

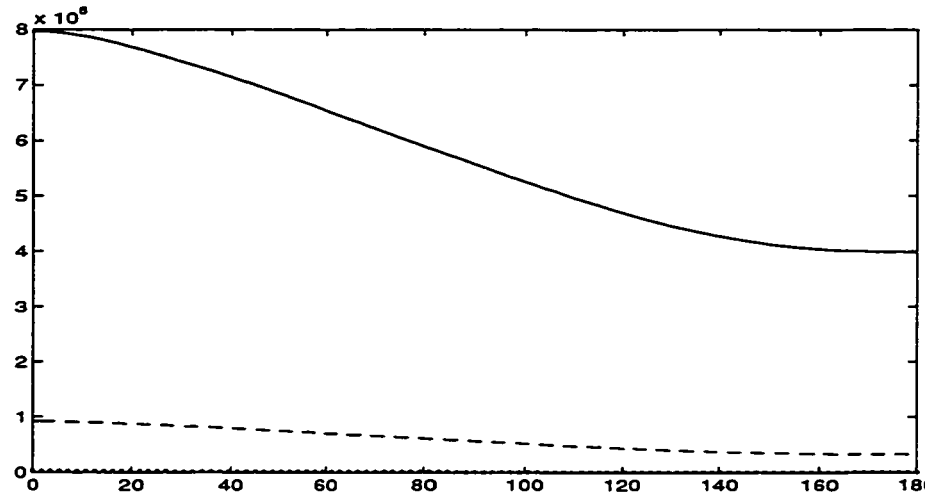

Figure 6.3: Variation of the condition number of the mass matrix $M(q_2, 0)$ (y–axis) vs q_2 (x–axis, degrees) for $l_1 = l_2 = 0.7m$. (One mode: $\cdots$, Two modes: $--$, Three modes: $——$)

$$a_{0i} = 0.06985m, \quad i = 1,\ 2,\ 3 \quad (for\ both\ links) \tag{6.22}$$

The ill–conditioned mass matrix may be problematic in the optimization problem. Specifically, note that this matrix has to be inverted to obtain the terms in the objective function (6.19). Thus the terms in the mass matrix have to be computed as accurately as possible so that computational errors are minimized. The main sources of errors in the computations of the mass matrix arise from the integral terms (cf. (6.21)). Thus efficient and accurate numerical integration routines should be employed.

Considering the terms in the objective function (6.19), let us define the following

$$\begin{aligned} W_{ave} &:= \frac{1}{3}\sum_{i=1}^{3}\sqrt{\lambda_{min}(H_{220}K)\mid_{q_{2i}}} \\ A_{ave} &:= \frac{1}{3}\sum_{i=1}^{3}\sqrt{trace(\Gamma_o\Gamma_o^T)\mid_{q_{2i}}} \end{aligned} \tag{6.23}$$

These may be interpreted as the average lowest natural frequency and the average modal accessibility index respectively. These terms are plotted in Figure 6.4 when

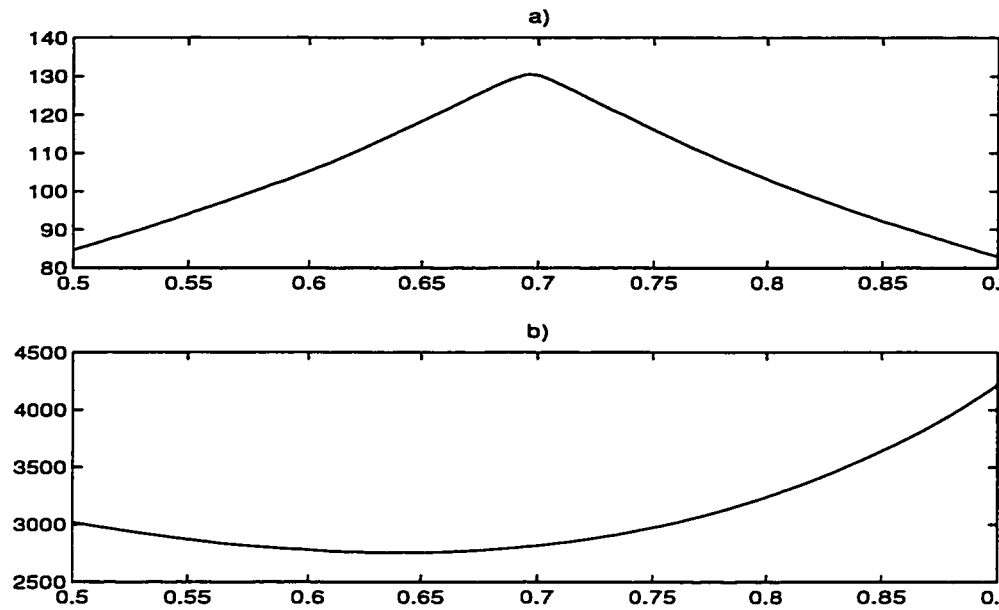

Figure 6.4: Variation of W_{ave} (rad/s) (a) and A_{ave} (b) when l_1 is varied from 0.5 to $0.9m$.

the length of the first link is varied and the total length of the links is fixed at $L_T = 1.4m$. Three flexible modes are used per link for this case. When two modes are used, the natural frequencies are slightly higher. The modal accessibility index is of course lower since there are fewer terms involved in A_{ave}.

Figure 6.5 shows the variation of W_{ave} versus the joint position q_2 for different combinations of link lengths. It is observed from Figure 6.4 that for l_1 near $0.7m$ ($l_2 = L_T - l_1$), W_{ave} is maximum, and Figure 6.5 shows that $W_{min} := \sqrt{\lambda_{min}(H_{220}K)}$ is significantly larger for the case when $l_1 = l_2 = 0.7m$. Figure 6.6 illustrates the behavior of the modal accessibility index $A_{acc} := \sqrt{trace(\Gamma_o \Gamma_o^T)}$ for the same conditions as in Figure 6.5.

Another major consideration in the design of the mechanical structure should be directed towards the torsional and lateral vibration effects (about the y–axis). In our planar two–link example there are no control inputs to affect flexibilities in these directions. Therefore, the structure should be such that these vibrational effects are minimized. Towards this goal, it can be shown from elastic potential energy

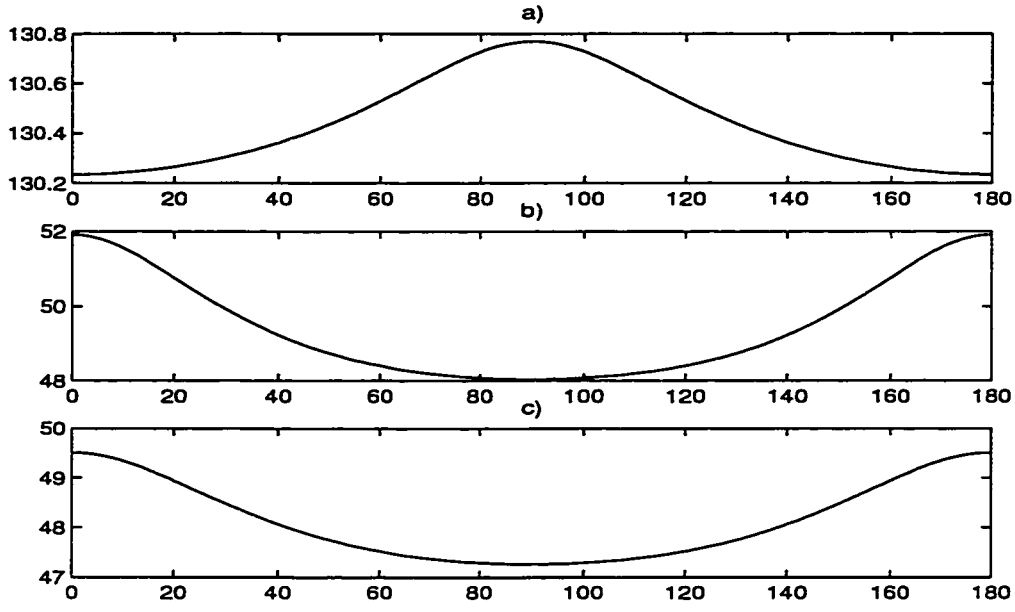

Figure 6.5: Variation of W_{min} (rad/s) (the lowest natural frequency) with links lengths vs. q_2 ($x - axis$, degrees) for uniform links, a) $l_1 = l_2 = 0.7m$ b) $l_1 = 0.2,\ l_2 = 1.2m$ and c) $l_1 = 1.2,\ l_2 = 0.2m$.

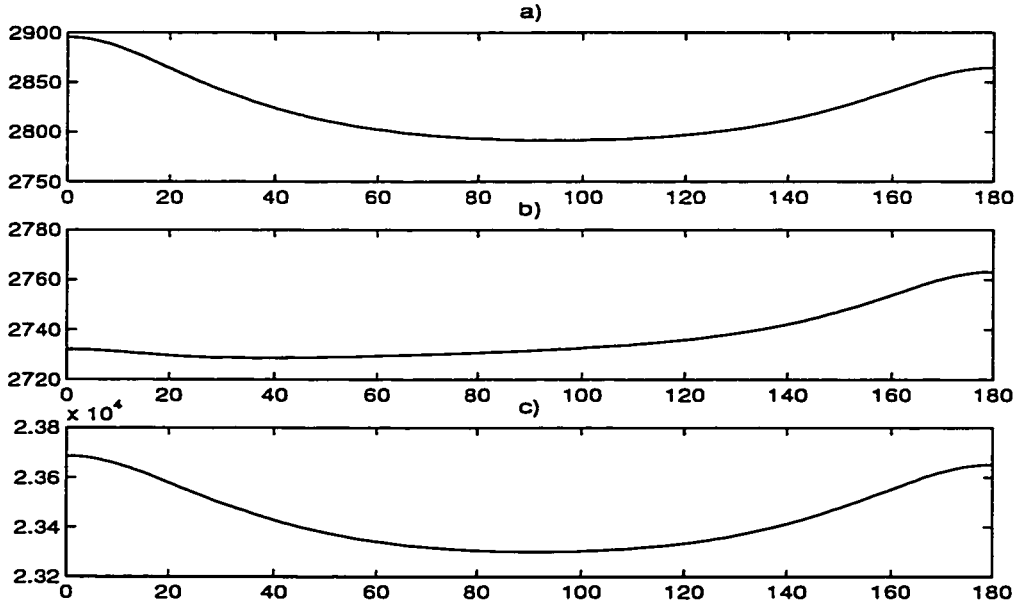

Figure 6.6: Variation of the accessibility index A_{acc} for uniform links when q_2 (horizontal axis) varies from 0 to 180°, a) $l_1 = l_2 = 0.7m$ b) $l_1 = 0.2,\ l_2 = 1.2m$ and c) $l_1 = 1.2,\ l_2 = 0.2m$.

considerations (cf. e.g. [29]) that making the ratio of the cross–sectional height to its thickness large, reduces the potential energy contribution of these deflections with a factor proportional to the inverse of the square of this ratio. A ratio of at least 10 has been used in our simulations.

6.3.1 Results of the Optimization

Case I: $n = 3$

The initial starting point for the optimization problem corresponds to two uniform bars with equal lengths $l_1 = l_2 = 0.7m$ (close to the maximum in Figure (6.4-a)). The numerical data used for the simulations are given in (6.22) with $L - i$ initialized to $0.23m$ for all sections of each link. The geometrical constraints used in the optimization are given by

$$0 \leq L_i \leq 0.92m, \quad 0.1cm \leq c_{1i} \leq 0.32cm, \quad -0.6cm \leq c_{2i} \leq 0.32cm$$

These figures are chosen to match the length specifications of a 6061 aluminum bar with $0.63 \times 7.62cm$ cross section and also meet the height to the thickness ratio requirement for the cross section as discussed earlier in Section 3. The c_1 and c_2 terms are set to normalize each term of the objective function to one at the starting point. When c_1 and c_2 are both nonzero this accounts for proportional weighting of the terms in the objective function. Moreover, the cases where $c_2 = 0$ and constraints (v) or (vi) in (6.1) are removed are also considered. The results are summarized in Table 6.1. The results in this example show that the links appear to be thicker in the middle parts, but no general conclusion may be drawn from this observation. What is happening here is that due to the constraints imposed on the mass and the mass moments of inertia, the mass matrix does not change significantly. However, the stiffness matrix, $K(p)$, changes from the diagonal matrix for the uniform case to a non–diagonal matrix for the optimized case such that better W_{min} and modal accessibility are achieved. Consider the first entry in Table

Case	Link Number	L_1 L_2 L_3 (cm)	c_{11} c_{12} c_{13} (mm)	c_{21} c_{22} c_{23} (mm)	Objective Function initial	Objective Function final	Active Constraints
$C_1, C_2 \neq 0$ Constraints: i, ii, iii, iv v, vi	1	17.0 31.2 35.2	1.0 3.2 1.0	-6.0 3.2 -6.0	2	3.65	i, iii, v
	2	25.9 2.3 28.4	1.0 3.2 1.0	-6.0 -6.0 -6.0			
$C_2=0$ Constraints: i, ii, iii, iv, vi	1	20.0 28.5 21.5	3.2 3.2 1.0	-6.0 3.2 -6.0	1	1.42	i, v
	2	11.9 33.9 24.2	1.0 3.2 1.0	-6.0 3.2 -6.0			
$C_2=0$ Constraints: i, ii, iii, iv	1	17.5 29.7 22.5	3.2 3.2 1.0	-6.0 3.2 -6.0	1	1.43	i, ii
	2	17.0 32.0 21.3	3.2 3.2 1.0	-6.0 3.2 -6.0			

Table 6.1: Results of the optimization for different cases (see equation).

6.1. Plots of the minimum natural frequency W_{min} and the modal accessibility index A_{acc} are given in Figure 6.7 when q_2 varies from 0° to 180°. Also shown are the characteristics for a uniform flexible–link manipulator. Since constraint (v) is active, the natural frequencies are approximately the same. However, the modal accessibility index for the nonuniform arm has improved to approximately 2.5 times that for the uniform arm. Figure 6.8 shows the results for the second and third entries in Table 6.1 along with the original uniform case. Note that when the constraint on control is removed W_{min} will only increase slightly as compared to the case when this constraint is present. In both cases, the major improvement occurs for W_{min}.

Case II: Large n

A two–link manipulator is considered in which the first link is rigid and the second link is flexible. The lengths of the links are fixed at $0.2m$ and $1.3m$ for the first and

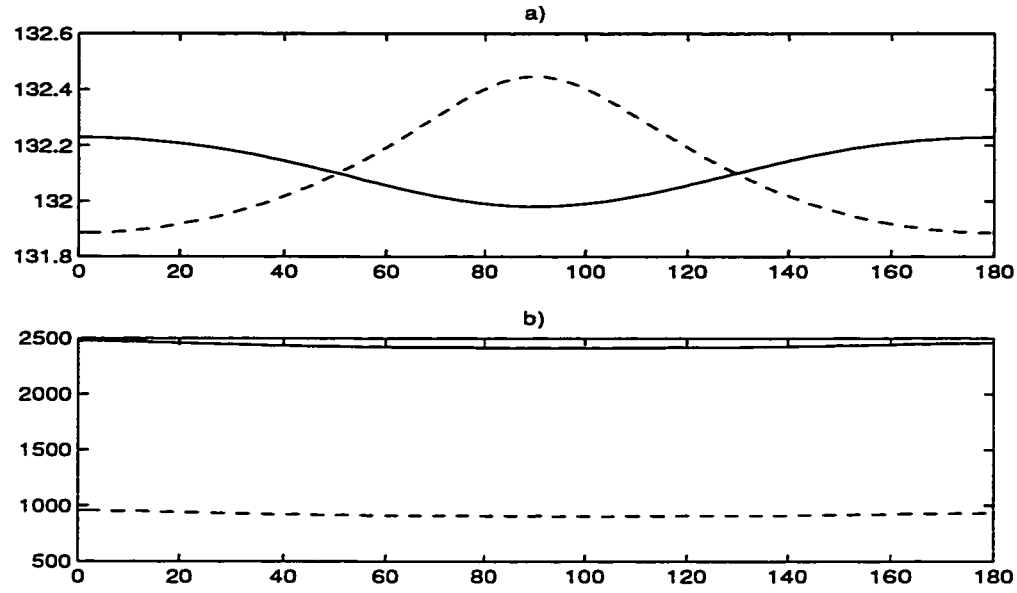

Figure 6.7: Comparison of the optimized (——) and the uniform (– –) flexible links, a) Lowest natural frequency W_{min}, rad/s vs q_2 (degrees), and b) Modal accessibility index A_{acc} vs q_2.

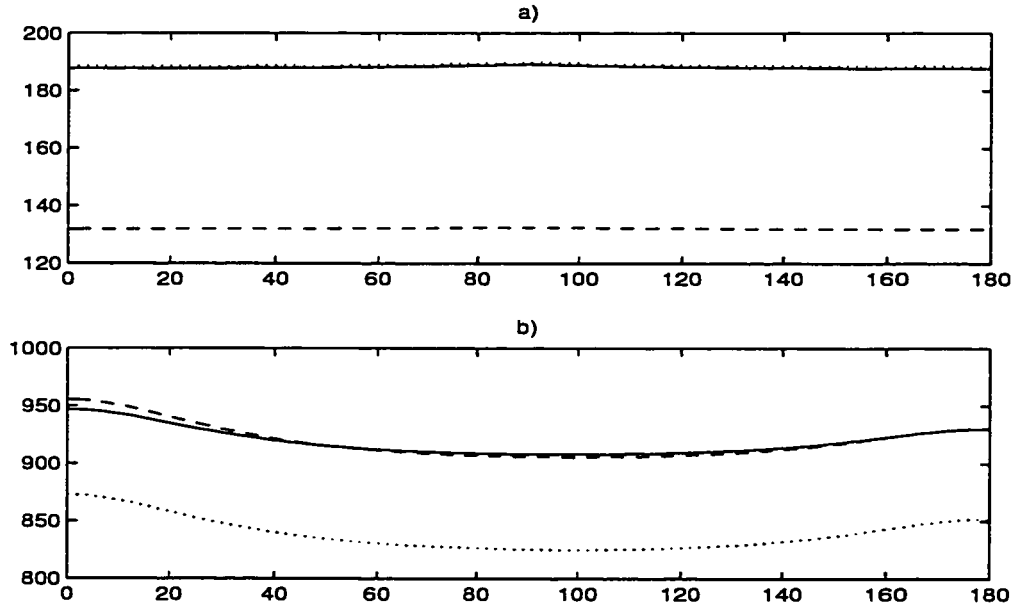

Figure 6.8: Comparison of the results of optimization for the second and third entries in Table 1 (entry 2: ——, entry 3: $\cdots$, uniform case: – –), a) Lowest natural frequency W_{min} (rad/s) vs q_2 (degrees) and b) Modal accessibility index A_{acc} vs q_2.

second links, respectively. The number of sections is selected as $n = 20$. In this case L_i is fixed at l_2/n, and a rectangular cross section is assumed for which the ratio of height to thickness is 20 at each point. The optimization problem is then solved by starting from a uniform manipulator. Figure 6.9c shows the thickness profile of the second link where the x–axis passes through the beam center. In this case the overall normalized objective function is increased from 2 to 6.91 (W_{ave} from 11.5 rad/s to 30.6 rad/s, and A_{acc} from 1.60×10^3 to 6.76×10^3).

Optimization Using B–Splines

In order to obtain smoother shapes for the link profiles, the optimization problem can be formulated in terms of certain parameters defining *B–form* splines or B–splines [83], [84]. A spline is defined by its (nondecreasing) *knot* sequence and its B–spline coefficient sequence. The elements of the knot sequence can be selected such that certain smoothness conditions are satisfied at each knot (determined by the multiplicity of each knot and the order of the B–spline). Thus, considering points within a certain interval (a certain knot sequence), the B–spline coefficients model the function they represent. For a specific knot sequence and by considering these coefficients as parameters, the geometric description of the link shapes are then at our disposal. Then the mass and stiffness matrices required in (6.19) are obtainable. Thus the optimization problem may be formulated in terms of the B–spline coefficients that now represent the parameter vector p in (6.1). Figures 6.9a, 6.9b, and 6.9d show the results of the optimization when third order B–splines are employed with the same initial parameters as in Section 4.2. A comparison of the results obtained shows that smoother shapes as well as better overall performance may be obtained compared to the case when rectangular cross sections are used (compare Figures 6.9c and 6.9d). It should be mentioned that the lower and upper limits of the thickness profiles were selected as one–third and three times the initial value of the thickness at the initialization point, respectively. In Figure 6.9 the

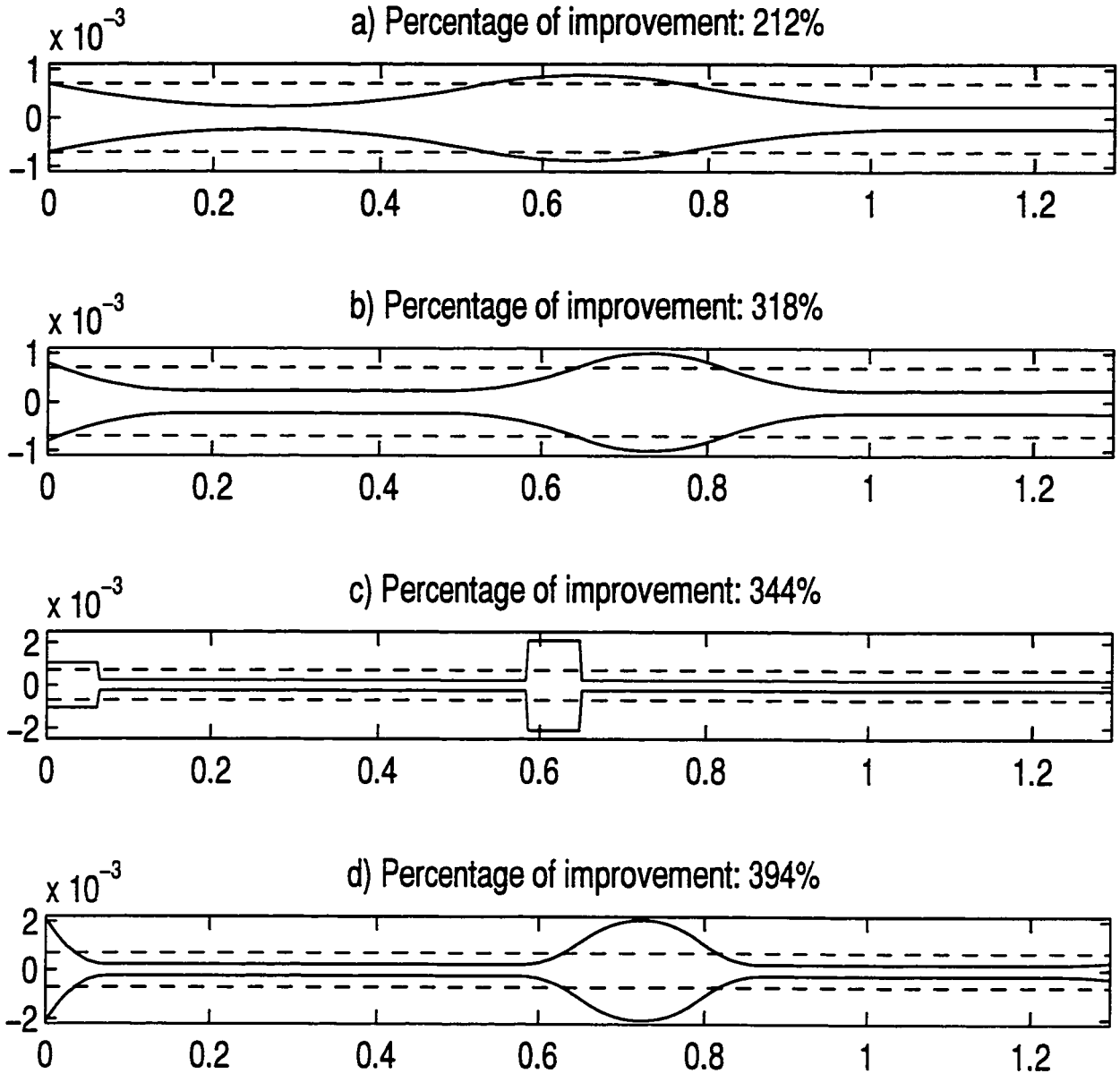

Figure 6.9: Thickness profile of the second link (x–y axis in m)(optimized case: ——, uniform and non–optimized case: – – –) (In each figure the percentage of improvement refers to the improvement in the objective function as compared to the uniform case), a) Knot sequence $\{0, 0, 0, l_2/8, 2l_2/8, ..., 7l_2/8, l_2, l_2, l_2\}$ and seven coefficients for the parameter vector, b) Knot sequence $\{0, 0, 0, l_2/5, 2l_2/5, ..., l_2, l_2, l_2\}$ and ten coefficients for the parameter vector, c) Case for $n = 20$ using rectangular sections, and d) Knot sequence $\{0, 0, 0, l_2/18, 2l_2/18, ..., l_2, l_2, l_2\}$ and twenty coefficients for the parameter vector.

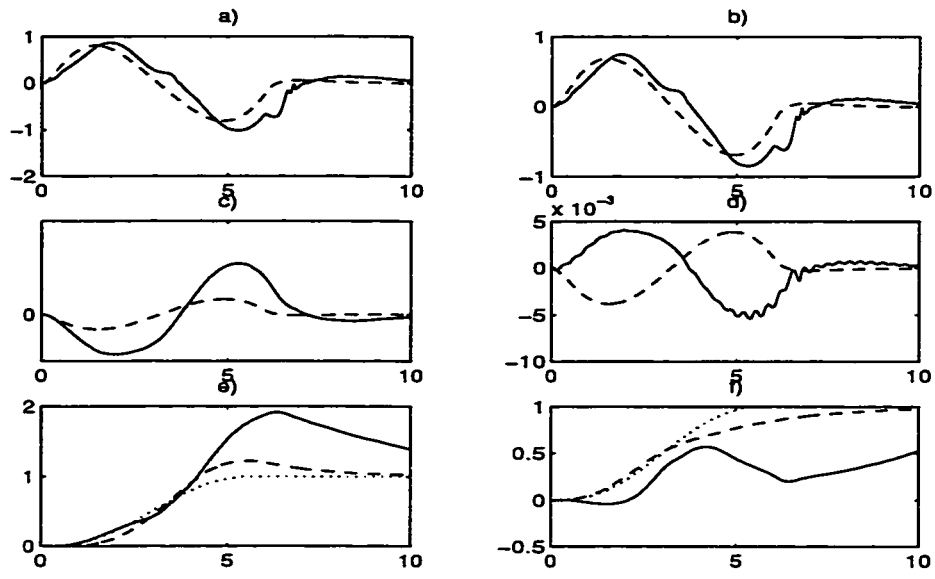

Figure 6.10: Comparison of the dynamic behavior for the optimized non–uniform manipulator (– –) and the uniform manipulator (—), (a,b) First and second actuator torques (Nm) vs time (s), respectively, (c,d) The first two flexible modes (m) vs time (s), respectively, and (e,f) Tip position outputs and reference trajectory ($\cdots$) in radians for links 1 and 2, respectively.

lower limits are all at $4.66 \times 10^{-4}m$. If this limit is reduced better performance is achieved as long as other physical constraints such as the maximum allowable stress (strength) are not violated (cf. e.g. [86]).

Comparison of the Dynamic Performance

A two–link manipulator similar to the previous case is designed with (n =)4 sections and the dynamic behavior of the optimized and uniform cases are compared for tracking the same reference trajectory by using the *computed torque* control law based on the rigid part of the dynamic equations. The complete nonlinear dynamic equations are taken into account using two flexible modes. The results are shown in Figure 6.10. The optimized manipulator shows better performance although the controller needs to be improved to obtain better tip position tracking (e.g., by more advanced control laws such as those introduced in the previous chapters).

6.4 Conclusion

The results for different software optimization scenarios show that improvements are achieved over the case of a manipulator with uniform links. The results are valid locally. The improvements are obtained based on the lowest natural frequency of the flexible modes, or the modal accessibility of these modes, or both. This is achieved without exceeding the constraints on the mass of the links or the inertias experienced by the motors. Because of the above requirements, the optimization parameters change in such a way that the mass matrix of the manipulator is not significantly different from the uniform case. However, the changes are mostly present in the stiffness matrix that is no longer diagonal for the nonuniform optimized manipulator (assuming that orthogonal shape functions are used). Finally, a comparison of the dynamic performance between uniform manipulators and optimized non–uniform manipulators shows that, subject to the same control strategy, the optimized non–uniform manipulators exhibit improved dynamic behavior. There is certainly a limit as to how much improvement may be achieved by the optimized structure. Further improvements can be accomplished by more advanced controllers such as those designed in the previous chapters.

Chapter 7

Concluding Remarks and Suggestions for Future Research

It is now for nearly more than a decade that researchers in control and robotics have been investigating the problem of controlling robotic mechanisms with considerable structural flexibilities. Nevertheless, it seems that, from a control and design perspective, this issue will remain an open research area in the years to come. As was mentioned earlier, several factors contribute to the complexity of the problem. The dynamic model complexity, uncertainties in modeling, ill–conditioned nonlinear dynamics, and nonminimum–phase characteristics are among the major factors.

In this dissertation we have focused on two nonlinear model–based design methods for trajectory tracking control, and have considered a structural shape design. The control strategies were implemented and tested on an experimental two–link flexible setup that was constructed in the laboratory. This system possesses interesting nonlinear and nonminimum–phase features that can be found in other systems such as aircrafts, underwater vehichles, large flexible satellites, and some other under–actuated mechanical systems. Although the control goals may be different, many similarities exist between these systems. Therefore the control methods can be applied to other cases once proper modifications are made. The

main advantage of the control strategies studied in this dissertation over the conventional control methods is robust closed–loop performance with sufficiently small tip–position tracking errors. These two features are not convenient to achieve with ordinary control schemes. However, the price to be paid is more control complexity and the need for faster real–time computation engines. Based on the experience gained in the course of this research the following routes may be taken for further work.

1. Control Using Integral Manifolds

One problem with this control strategy is the complexity of the controller. This is a major problem, specifically if the number of links is increased. One way to deal with this issue is to use some kind of function approximation by using neural networks or Spline functions. Splines can be used to represent functions that cannot be represented in closed-form and can be used to represent nonlinearities in plant models and nonlinear controllers [89]. Further improvement of this control strategy lies in devising or modifying the control law to deal with parametric uncertainties and parameter variations. In this regard adaptive techniques may be considered. However, these techniques may further raise complexity issues in control implementation and should be studied along with the function approximation described earlier.

2. Input–Output Decoupling Control

The control strategy based on decoupling and using observers for estimating flexural rates is generally less complicated, in terms of implementation, compared to the integral manifold method. One problem that arises here is that the ill–conditioned mass matrix and parametric uncertainties can cause instability [91]. The lines that can be followed towards resolving this issue include using dynamic decoupling [68], [72], and robust designs such as sliding techniques [75].

3. Structure Design

As discussed previously, a major goal in structural shape design is achieving better robustness in a closed–loop control system. It is possible that a better optimization index can be defined if controllability and observability properties can also be incorporated in shape design. Increasing the structural natural frequencies has to be kept as one of the optimization goals as before. In addition, as the number of optimization goals increases consideration should be given to employing appropriate schemes for multi–objective optimization.

In this research, we have only considered mechanical shape design. While this is an important aspect, one should not overlook *smart* techniques that facilitate the control problem by designing material type, actuators and sensors (see e.g., [28]).

In the author's view, a successful solution should be an integration of control and structure/material design. As far as the control design is concerned, one may follow classical techniques, intelligent methods (fuzzy logic, neural networks, neuro–fuzzy), or a combination of the two. A successful control strategy should consider robustness to parametric uncertainties as well as higher frequency flexural modes while maintaining desired performance.

Undoubtedly, more extensive benchmark comparisons have to be made before any conclusions can be drawn concerning the superiority of an approach over another.

Appendix A

Stability Proofs

The stability analysis for the various key results obtained in this research are given in this appendix.

A.1 Proof of Theorem 2.1

The stability analysis follows along the lines developed in [53]. Consider the open-loop system (2.5)–(2.6) with the control laws obtained from (2.10), (2.11), (2.25), (2.35), (2.41), and (2.42), that is

$$\begin{aligned}
u &= u_s(x,\varepsilon,t) + u_f(x,z) \\
u_s &= u_0 + \varepsilon u_1 + \varepsilon^2 u_2 \\
u_0 &= M_{110} v_0 + f_1(x_1, x_2) \\
u_1 &= M_{110} v_1 \\
u_2 &= M_{110}(v_2 + d(x_1, x_2, \dot{x}_2\,|_{\varepsilon=0}, u_0, \dot{u}_0) - \Psi \ddot{h}_{10}) \\
\dot{v} &= A_v v + b_v(\ddot{y}_r, e, \varepsilon) \\
\varepsilon \dot{w} &= F(x_1) w + G(x_1) y_f \\
u_f &= M(x_1) w
\end{aligned} \tag{A.1}$$

Substituting the above control laws into system (2.5)–(2.6) and adopting the same definitions for e and $\tilde{z}$ as before, after some algebraic manipulations, yields

$$\begin{aligned} \dot{e} &= A_e e + b_e(x, \tilde{z}, w, v, \varepsilon, t) \\ \dot{v} &= A_v v + b_v(\ddot{y}_r, e, \varepsilon) \\ \varepsilon\dot{\eta} &= A_\eta(x_1)\eta + b_\eta(x, \tilde{z}, w, v, t) \end{aligned} \tag{A.2}$$

where $\eta^T = [\tilde{z}^T \quad w^T]$, and $b_v(\ddot{y}_r, e, \varepsilon)$ is the same as before, and

$$\begin{aligned} b_e(x, \tilde{z}, w, v, \varepsilon, t) &= \begin{bmatrix} 0 \\ -\frac{H_{120}K}{\lambda_{min}}\tilde{z}_1 + H_{110}M(x_1)w - \varepsilon(H_{110}G_{11} + H_{120}G_{21})\tilde{z}_2 + O_1(\varepsilon^2) \end{bmatrix} \\ b_\eta(x, \tilde{z}, w, v, t) &= \begin{bmatrix} -\varepsilon^3\dot{h}_{12} \\ -\varepsilon(H_{210}G_{11} + H_{220}G_{21})\tilde{z}_2 + O_2(\varepsilon^2) \\ \varepsilon^3 G(x_1)\Psi(h_{11} + \varepsilon h_{12}) \end{bmatrix} \end{aligned} \tag{A.3}$$

Noting that the matrices A_e, A_v, and $A_\eta(x_1)$ are all Hurwitz, we can write the following Lyapunov equations

$$\begin{aligned} A_e^T P_e + P_e A_e &= -Q_e \\ A_v^T P_v + P_v A_v &= -Q_v \\ A_\eta^T(x_1)P_\eta(x_1) + P_\eta(x_1)A_\eta(x_1) &= -Q_\eta \end{aligned} \tag{A.4}$$

where Q_e, Q_v, and Q_η are positive definite symmetric $O(1)$ matrices. Choosing the positive definite Lyapunov function candidate

$$V = e^T P_e e + \hat{v}^T P_v \hat{v} + \varepsilon\eta^T P_\eta(x_1)\eta \tag{A.5}$$

where $\hat{v} = \varepsilon^2 v$ [42]–[43], and computing the derivative of V along the trajectories of (A.2) yields

$$\begin{aligned} \dot{V} &= -e^T Q_e e - \hat{v}^T Q_v \hat{v} - \eta^T Q_\eta \eta + 2e^T P_e b_e \\ &+ 2\varepsilon^2 \hat{v} P_v b_v + 2\eta^T P_\eta(x_1) b_\eta + \varepsilon\eta^T \dot{P}_\eta(x_1)\eta \end{aligned} \tag{A.6}$$

A detailed inspection of the terms b_e, b_v, and b_η reveals that on bounded regions $\Omega_1, \Omega_2, \Omega_3 \subset \mathbf{R}^{4n+2m+l}$ around the origin of the (e, v, η) state space, and by assuming a C^2 desired reference trajectory, we may write

$$\begin{aligned}
\|b_e\| &\leq \gamma_E\|\eta\| + \varepsilon^2(l_1 + l_{11}\|e\| + l_{12}\|\eta\|), \qquad \forall (e,v,\eta) \in \Omega_1 \\
\|b_v\| &\leq \gamma_r + \gamma_{pd}\|e\|, \qquad \forall (e,v,\eta) \in \Omega_2 \\
\|b_\eta\| &\leq \varepsilon(\gamma_\eta + \gamma_{\eta 1}\|e\|)\|\eta\| + \varepsilon^2(l_2 + l_{21}\|e\| + l_{22}\|\eta\|), \quad \forall (e,v,\eta) \in \Omega_3
\end{aligned} \tag{A.7}$$

where l_1, l_2, l_{11}, l_{12}, l_{21}, l_{22} are upper bound constants specified in the regions Ω_1 and Ω_3. Furthermore

$$\begin{aligned}
\gamma_E &= \|[-\frac{H_{120}K}{\lambda_{min}}, \quad -\varepsilon(H_{110}G_{11} + H_{120}G_{21}), \quad H_{110}M(x_1)]\|_{max \text{ on } \Omega_1} \\
\gamma_r &= \|\frac{A_1A_2^{-1}}{\varepsilon^2}\ddot{y}_r\|_{max} \\
\gamma_{pd} &= \|\frac{A_1A_2^{-1}}{\varepsilon^2}[K_p, \quad K_d]\| \\
\gamma_\eta &= \|H_{210}G_{11} + H_{220}G_{21}\|_{max \text{ on } \Omega_3,\ e=0}
\end{aligned} \tag{A.8}$$

Similarly, for all $(e, v, \eta) \in \Omega_4 \subset \mathbf{R}^{4n+2m+l}$ we have

$$\|\dot{P}_\eta(x_1)\| \leq l_3 \tag{A.9}$$

Thus defining

$$\lambda_e := \lambda_{min}\{Q_e\}, \quad \lambda_v := \lambda_{min}\{Q_v\}, \quad \lambda_\eta := \lambda_{min}\{Q_\eta\} \tag{A.10}$$

and making use of (A.7) and (A.9) in (A.6) results in

$$\dot{V} \leq -[\|e\| \ \|\hat{v}\| \ \|\eta\|]\Lambda \begin{bmatrix} \|e\| \\ \|\hat{v}\| \\ \|\eta\| \end{bmatrix} + 2\alpha^T \begin{bmatrix} \|e\| \\ \|\hat{v}\| \\ \|\eta\| \end{bmatrix}, \quad \forall (e,v,\eta) \in \Omega_I \tag{A.11}$$

where $\Omega_I = \Omega_1 \cap \Omega_2 \cap \Omega_3 \cap \Omega_4$ and

$$\alpha^T = \varepsilon^2[l_1\|P_e\| \quad \gamma_r\|P_v\| \quad l_2\|P_\eta\|]$$

$$\Lambda = \begin{bmatrix} \lambda_e - 2\varepsilon^2 l_{11}\|P_e\| & -\varepsilon^2\gamma_{pd}\|P_v\| & -\gamma_E\|P_e\| - \varepsilon\gamma_{\eta_1}\|P_\eta\| - \varepsilon^2(l_{12}\|P_e\| + l_{21}\|P_\eta\|) \\ -\varepsilon^2\gamma_{pd}\|P_v\| & \lambda_v & 0 \\ -\gamma_E\|P_e\| - \varepsilon\gamma_{\eta_1}\|P_\eta\| - \varepsilon^2(l_{12}\|P_e\| + l_{21}\|P_\eta\|) & 0 & \lambda_\eta - \varepsilon(2\lambda_\eta\|P_\eta\| + l_3) - 2\varepsilon^2 l_{22}\|P_\eta\| \end{bmatrix}$$

Noting that $\gamma_{pd}\|P_v\|$ will remain $O(1)$ as ε tends to zero, we conclude that if $\lambda_e\lambda_\eta > \gamma_E\|P_e\|^2$, then Λ will be positive–definite for all $\varepsilon \in (0, \varepsilon_{max})$, where ε_{max} is the upper bound for ε. Assuming that ε lies in this interval, let us apply the coordinate transformation

$$\mathcal{X} = \begin{bmatrix} \|e\| \\ \|\hat{v}\| \\ \|\eta\| \end{bmatrix} - \Lambda^{-1}\alpha \tag{A.12}$$

that when substituted in (A.11) yields

$$\dot{V} \leq -\mathcal{X}^T\Lambda\mathcal{X} + \alpha^T\Lambda^{-1}\alpha \qquad \forall(e, v, \eta) \in \Omega_I \tag{A.13}$$

Consider the case when $\mathcal{X}^T\Lambda\mathcal{X} = \alpha^T\Lambda^{-1}\alpha$. This is the equation of an ellipsoid in $\mathcal{X}$ coordinates. Furthermore, using the spectral theorem of linear algebra, Λ may be written as $\Lambda = Q^T\Lambda_d Q$, where Q is a matrix whose columns are the orthogonal eigenvectors of Λ, and Λ_d is a diagonal matrix of the eigenvalues of Λ. The equation of the ellipsoid may then be written as $(Q^T\mathcal{X})^T\Lambda_d(Q^T\mathcal{X}) = \alpha^T\Lambda^{-1}\alpha$. Thus the largest and smallest diagonals of the ellipsoid are given respectively by $\sqrt{\alpha^T\Lambda^{-1}\alpha/\lambda_{min}(\Lambda)}$ and $\sqrt{\alpha^T\Lambda^{-1}\alpha/\lambda_{max}(\Lambda)}$.

To show the boundedness of solutions, let us consider the following sets

$$\begin{aligned} \mathcal{R} &= \{(e, \hat{v}, \eta) \mid \mathcal{X}^T\Lambda\mathcal{X} \leq \alpha^T\Lambda^{-1}\alpha\} \cap \Omega_I \\ \mathcal{S} &= \{(e, \hat{v}, \eta) \mid V(e, \hat{v}, \eta) \leq c_1\} \subset \Omega_I \\ \mathcal{T} &= \{(e, \hat{v}, \eta) \mid V(e, \hat{v}, \eta) = c_2\} \subset \Omega_I \end{aligned} \tag{A.14}$$

where $0 < c_2 \leq c_1$ and c_2 is the smallest constant such that $\mathcal{R} \subset \mathcal{T}$. Since the trajectory defined by y_r, $\dot{y}_r$, $\ddot{y}_r$ is bounded and Λ is positive–definite, $\mathcal{R}$ is uniformly bounded. If the initial state is outside $\mathcal{S} - \mathcal{R}$, where $\dot{V} \leq 0$, it follows that there exists a finite time t_f such that any solution starting from $\mathcal{S} - \mathcal{R}$, at $t > 0$, will enter $\mathcal{T}$ at t_f, and reside in $\mathcal{T}$ thereafter for all $t \geq t_f$. The residual set $\mathcal{T}$ encompasses the ellipsoid. Thus the size of the residual set is on the order of the maximum diameter of the ellipsoid. Since Λ is $O(1)$ and α is $O(\varepsilon^2)$, the residual set is of $O(\varepsilon^2)$. Therefore e, $\hat{v}$, and η remain bounded up to $O(\varepsilon^3)$ after t_f. Thus, v will be $O(1)$ in the steady state. This completes the proof of the theorem stated in Section 3.

A.2 Proof of Theorem 3.1

Consider the dynamic equations of the closed–loop system given by (3.22) and (3.24). Since A_E and $A_\Delta(q)$ are Hurwitz matrices we have the Lyapunov equations

$$\begin{aligned} A_E^T P_E + P_E A_E &= -Q_E \\ A_\Delta^T(q) P_\Delta(q) + P_\Delta(q) A_\Delta(q) &= -Q_\Delta \end{aligned} \tag{A.15}$$

where P_E, Q_E, $P_\Delta(q)$, Q_Δ are positive–definite matrices. Let us choose the positive–definite Lyapunov function candidate

$$V = E^T P_E E + \hat{\Delta}^T P_\Delta(q) \hat{\Delta} \tag{A.16}$$

where $\hat{\Delta} = \epsilon_1 \Delta$ with ϵ_1 being a positive constant (typically less than one). Then $\dot{V}$ is given by

$$\dot{V} = -E^T Q_E E - \hat{\Delta}^T Q_\Delta \hat{\Delta} + 2 d_E^T P_E E + 2\epsilon_1 \hat{\Delta} P_\Delta G_\Delta + \hat{\Delta} \dot{P}_\Delta \hat{\Delta} \tag{A.17}$$

Consider a continuous bounded reference trajectory (at least C^2) and a bounded region Ω_1 containing the origin of E and Δ. Then for all $(E, \Delta) \in \Omega_1 \subset \mathbf{R}^{m+n}$ we can write

$$\|a\| \leq l_1 + l_2 \|E\| + l_3 \|\Delta\|, \quad \|I - B\hat{B}^{-1}\| \leq \epsilon_2, \quad \|B\hat{B}^{-1}\| \|\Delta a\| \leq \epsilon_3 \tag{A.18}$$

where l_i's and ϵ_i's are certain bounds with ϵ_i's being typically small quantities. Further, let

$$\|[K_p \;\; K_d]\| = l_4, \quad \|[BK_\delta \;\; BK_{\dot{\delta}}]\| \leq l_5, \quad \|\ddot{y}_r\| \leq l_6 \tag{A.19}$$

to get

$$\|d_E\| \leq \epsilon_3 + \epsilon_2(l_1 + l_6) + \epsilon_2(l_2 + l_4)\|E\| + (l_5 + \epsilon_2 l_3)\frac{\|\hat{\Delta}\|}{\epsilon_1} \tag{A.20}$$

Similarly, for all $(E, \Delta) \in \Omega_2 \subset \mathbf{R}^{m+n}$, where Ω_2 is a finite region containing the origin of $(E,\ \delta)$, we have

$$\|H_{210}\hat{B}_0^{-1}\| \approx 1, \;\; \|H_{210}(-\hat{B}_0^{-1}\hat{a}_0 + B_0^{-1}a_0\| \leq \epsilon_4(l_6 + l_7\|E\|), \;\; \|O(\delta^2, q, \dot{q})\| \leq l_8 \tag{A.21}$$

Thus

$$\|G_\Delta\| \leq l_6 + l_4\|E\| + \epsilon_4(l_6 + l_7\|E\|) + l_8, \qquad \forall (E, \Delta) \in \Omega_2 \tag{A.22}$$

A detailed analysis also reveals that for all $(E, \Delta) \in \Omega_3 \subset \mathbf{R}^{m+n}$, where Ω_3 is a finite region containing the origin of $(E,\ \delta)$, we have $\|\dot{P}_\delta(q)\| \leq l_9$. Hence, letting $\Omega_i = \Omega_1 \cap \Omega_2 \cap \Omega_3$ and substituting the previous inequalities in $\dot{V}$ given by (A.17) and rearranging the right-hand side of the resulting inequality in terms of $\|E\|$ and $\|\Delta\|$ will, after some algebraic manipulations, yield

$$\dot{V} \leq -[\|E\| \;\; \|\hat{\Delta}\|]\Lambda \begin{bmatrix} \|E\| \\ \|\hat{\Delta}\| \end{bmatrix} + 2\gamma^T \begin{bmatrix} \|E\| \\ \|\hat{\Delta}\| \end{bmatrix} \qquad \forall (E, \Delta) \in \Omega_i \tag{A.23}$$

where

$$\Lambda = \begin{bmatrix} \lambda_e - 2\epsilon_2(l_2 + l_4)\|P_E\| & \frac{(l_5+\epsilon_2 l_3)\|P_E\|}{\epsilon_1} + \epsilon_1\|P_\Delta\|(l_4 + \epsilon_4 l_7) \\ \frac{(l_5+\epsilon_2 l_3)\|P_E\|}{\epsilon_1} + \epsilon_1\|P_\Delta\|(l_4 + \epsilon_4 l_7) & \lambda_\Delta - l_9 \end{bmatrix},$$

$$\gamma^T = [(\epsilon_3 + \epsilon_2(l_1 + l_6))\|P_E\| \;\; \epsilon_1\|P_\Delta\|(l_6 + l_8 + \epsilon_4 l_6)], \;\; \lambda_e = \lambda_{min}(Q_E), \;\; \lambda_\Delta = \lambda_{min}(Q_\Delta$$

(A.24

Now consider the case where there are no parameter errors. Provided that $\lambda_\Delta > l_9$, and $\lambda_e(\lambda_\Delta - l_9) > l_5\|P_E\|/\epsilon_1 + \epsilon_1 l_4\|P_\Delta\|$, the matrix Λ is positive definite. It then

follows that for a certain range of parameter variations in this neighborhood, Λ remains positive definite. Assuming that this condition holds, let us define the sets

$$\begin{aligned}
\mathcal{R} &= \{(E,\hat{\Delta}) \mid [\|E\| \; \|\hat{\Delta}\|]\Lambda[\|E\| \; \|\hat{\Delta}\|]^T \leq 2\gamma^T[\|E\| \; \|\hat{\Delta}\|]^T\} \cap \Omega_i \\
\mathcal{S} &= \{(E,\hat{\Delta}) \mid V(E,\hat{\Delta}) \leq c_1\} \subset \Omega_i \\
\mathcal{T} &= \{(E,\hat{\Delta}) \mid V(E,\hat{\Delta}) = c_2\} \subset \Omega_i
\end{aligned} \tag{A.25}$$

where $0 < c_2 \leq c_1$ and c_2 is the smallest constant such that $\mathcal{R} \subset \mathcal{T}$. Since the trajectory defined by y_r, $\dot{y}_r$, $\ddot{y}_r$ is bounded and Λ is positive–definite, $\mathcal{R}$ is uniformly bounded. If the initial state is outside $\mathcal{S} - \mathcal{R}$, where $\dot{V} \leq 0$, it follows that there exists a finite time t_f such that any solution starting from $\mathcal{S} - \mathcal{R}$, at $t > 0$, will enter $\mathcal{T}$ at t_f, and remain in $\mathcal{T}$ thereafter for all $t \geq t_f$. The residual set $\mathcal{T}$ encompasses an ellipse in $[\|E\| \; \|\hat{\Delta}\|]$ coordinates with its diameters being $\sqrt{\gamma^T\Lambda^{-1}\gamma/\lambda_{min}(\Lambda)}$ and $\sqrt{\gamma^T\Lambda^{-1}\gamma/\lambda_{max}(\Lambda)}$. Since $\hat{\Delta} = \epsilon_1\Delta$, it follows that Δ is of the order of $\frac{1}{\epsilon_1}$ on this residual set. It is possible to obtain an optimum value of ϵ_1 by setting the parameter errors to zero in Λ, which gives $\epsilon_1 = \sqrt{l_5\|P_E\|/(l_4\|P_\Delta\|)}$. Some qualitative robustness measures may be obtained from this analysis. In particular, making the norms of P_E, $K_\delta(q)$, $K_{\dot{\delta}}(q)$ small and reducing the parameter errors yield a better margin of robustness. Note however that the lower limit of $K_\delta(q)$, $K_{\dot{\delta}}(q)$ is not zero since A_Δ should be a Hurwitz matrix.

A.3 Proof of Theorem 4.1

In what follows a closed–loop stability analysis is established for the case of a full–order observer. A similar analysis can be given for the case where a reduced–order observer is used. Consider the dynamic equations of the closed–loop system given by (4.10)–(4.11), (4.21)–(4.22) and (4.23)–(4.24) which are repeated here for convenience

$$\dot{\tilde{\delta}} = A_{\tilde{\delta}}\tilde{\delta} + b_{\tilde{\delta}}(x, \hat{\delta}_2) \tag{A.26}$$

$$\dot{E} = A_E E + d_E(\alpha, x_c, t) \tag{A.27}$$

$$\dot{\Delta} = A_\Delta(q)\Delta + \begin{bmatrix} 0 \\ \\ G_\Delta(x, \dot{\tilde{\delta}}, t) \end{bmatrix} \tag{A.28}$$

Since $A_{\tilde{\delta}}$, A_E and $A_\Delta(q)$ are Hurwitz matrices, the following Lyapunov equations are satisfied

$$\begin{aligned} A_{\tilde{\delta}}^T P_{\tilde{\delta}} + P_{\tilde{\delta}} A_{\tilde{\delta}} &= -Q_{\tilde{\delta}} \\ A_E^T P_E + P_E A_E &= -Q_E \\ A_\Delta^T(q) P_\Delta(q) + P_\Delta(q) A_\Delta(q) &= -Q_\Delta \end{aligned} \tag{A.29}$$

where $P_{\tilde{\delta}}$, $Q_{\tilde{\delta}}$, P_E, Q_E, $P_\Delta(q)$, Q_Δ are symmetric positive–definite matrices. Let us choose the positive–definite Lyapunov function candidate

$$V = E^T P_E E + \hat{\Delta}^T P_\Delta(q) \hat{\Delta} + \tilde{\delta}^T P_{\tilde{\delta}} \tilde{\delta} \tag{A.30}$$

where $\hat{\Delta} = \epsilon\Delta$ with ϵ being a small positive scaling constant (typically less than one). The scaling factor is introduced as a result of from the stability requirement that E and $\tilde{\delta}$ converge to small values near zero while Δ remains bounded. Thus, the scaling factor allows us to show that E, $\tilde{\delta}$ and $\hat{\Delta}$ converge to small values, hence Δ converges to $\hat{\Delta}/\epsilon$.

Taking the time derivative of V yields

$$\dot{V} = -E^T Q_E E - \hat{\Delta}^T Q_\Delta \hat{\Delta} - \tilde{\delta}^T Q_{\tilde{\delta}} + 2 d_E^T P_E E + 2 b_{\tilde{\delta}}^T P_{\tilde{\delta}} \tilde{\delta} + 2\epsilon \hat{\Delta} P_\Delta G_\Delta + \hat{\Delta} \dot{P}_\Delta \hat{\Delta} \tag{A.31}$$

Consider a continuous bounded reference trajectory (at least C^2) and a bounded region Ω_1 containing the origin of $(E, \Delta, \tilde{\delta})$. Then for all $(E, \Delta, \tilde{\delta}) \in \Omega_1 \subset \mathbf{R}^{\mathbf{m+4n}}$, from (4.22) we have

$$\|d_E\| \leq \frac{\epsilon_0}{\epsilon} \|\hat{\Delta}\| + \epsilon_1 \|\tilde{\delta}\| \tag{A.32}$$

where ϵ_0 depends on $K_\delta(q)$ and $K_{\dot{\delta}}(q)$ and should be sufficiently small by proper choice of these matrices as we shall see shortly. The ϵ_1 term is affected by $\|K_d\|$ and

the higher order terms in (4.22). Similarly, for all $(E, \Delta, \tilde{\delta}) \in \Omega_2 \subset \mathbf{R^{m+4n}}$, where Ω_2 is a finite region containing the origin of $(E, \Delta, \tilde{\delta})$, from (4.24) we have

$$\|G_\Delta\| \leq l_{\Delta_1} + l_E\|E\| + \frac{\epsilon_2}{\epsilon}\|\hat{\Delta}\| + \epsilon_3\|\tilde{\delta}\|, \quad \forall (E, \Delta, \tilde{\delta}) \in \Omega_2 \tag{A.33}$$

where l_{Δ_1} is mainly affected by the reference trajectory and l_E is affected by K_p and K_d. Constants ϵ_2 and ϵ_3 correspond to $O(\delta)$ and $O(\delta\hat{\delta})$ terms in (4.24), respectively. A detailed analysis also reveals that for all $(E, \Delta, \tilde{\delta}) \in \Omega_3 \subset \mathbf{R^{m+4n}}$, where Ω_3 is a finite region containing the origin of $(E,\ \Delta, \tilde{\delta})$, we have $\|\dot{P}_\Delta(q)\| \leq l_{\Delta_2}$. This can be shown by noting that $P_\Delta(q)$ has a finite growth rate with respect to q (see e.g. [67], Problem 5.21) and the reference trajectory is bounded. Hence, letting $\Omega_i = \Omega_1 \cap \Omega_2 \cap \Omega_3$ and substituting the previous inequalities in $\dot{V}$ and rearranging the right–hand side of the resulting inequality in terms of $\|E\|$, $\|\Delta\|$ and $\|\tilde{\delta}\|$ after some algebraic manipulations, yields

$$\dot{V} \leq -[\|E\|\ \|\hat{\Delta}\|\ \|\tilde{\delta}\|]\Lambda \begin{bmatrix} \|E\| \\ \|\hat{\Delta}\| \\ \|\tilde{\delta}\| \end{bmatrix} + 2\gamma^T \begin{bmatrix} \|E\| \\ \|\hat{\Delta}\| \\ \|\tilde{\delta}\| \end{bmatrix} \qquad \forall (E, \Delta, \tilde{\delta}) \in \Omega_i \tag{A.34}$$

where

$$\begin{aligned} \Lambda &= \begin{bmatrix} \lambda_e & \frac{\epsilon_0}{\epsilon} + l_E\epsilon\|P_\Delta\| & \epsilon_1\|P_E\| \\ \frac{\epsilon_0}{\epsilon} + l_E\epsilon\|P_\Delta\| & \lambda_\Delta - l_{\Delta_2} - 2\|P_\Delta\|\epsilon_2 & \epsilon\epsilon_3\|P_\Delta\| \\ \epsilon_1\|P_E\| & \epsilon\epsilon_3\|P_\Delta\| & \lambda_o - 2\epsilon_3\|P_{\tilde{\Delta}}\| \end{bmatrix}, \\ \gamma^T &= [0 \quad \epsilon l_{\Delta_1}\|P_\Delta\| \quad 0], \end{aligned} \tag{A.35}$$

and $\lambda_e = \lambda_{min}(Q_E)$, $\lambda_\Delta = \lambda_{min}(Q_\Delta)$, $\lambda_o = \lambda_{min}(A_{\tilde{\delta}})$.

Now consider the matrix Λ. This matrix will be positive–definite if $\lambda_\Delta > l_{\Delta_2}$, $\lambda_o > 2\epsilon_3\|P_{\tilde{\delta}}\|$ and the ϵ_i's are sufficiently small (which may be achieved by proper choice of the gain matrices). Note however that ϵ appears only in the off–diagonal terms of this matrix. A very small ϵ will increase the $\Lambda(2,1)$ element while a very large ϵ increases $\Lambda(2,3)$ and $\Lambda(2,1)$ elements. The element $\Lambda(2,1)$ is minimum for

$\epsilon = \sqrt{\epsilon_0/(l_E\|P_\Delta\|)}$ which should typically be made small by design. As explained earlier, ϵ_0 depends on $K_\delta(q)$ and $K_{\dot{\delta}}(q)$. On the other hand, the element $\Lambda(2,1)$ is directly affected by ϵ_0. Thus a reduction of ϵ_0 will be desirable since it will result in a smaller off diagonal term.

For $\epsilon = \sqrt{\epsilon_0/(l_E\|P_\Delta\|)}$, it is easy to obtain a condition on the elements of Λ so that it is positive–definite, i.e.,

$$\lambda_e(\lambda_\Delta - l_{\Delta_2} - 2\|P_\Delta\|\epsilon_2)(\lambda_o - 2\epsilon_3\|P_{\tilde{\Delta}}\|) + 4\|P_E\|\|P_\Delta\|\epsilon_0\epsilon_3 >$$
$$4(\lambda_o - 2\epsilon_3\|P_{\tilde{\Delta}}\|)\epsilon_0 l_E\|P_\Delta\| + \epsilon_0(\lambda_e\epsilon_3^2\|P_\Delta\|^2 + (\lambda_\Delta - l_{\Delta_2} - 2\|P_\Delta\|\epsilon_2)\|P_E\|^2)/(l_E\|P_\Delta\|) \tag{A.36}$$

It should also be noted that the effect of $\|K_d\|$ appears in the form of a product term with $\|P_E\|$ (in (A.35)), and since $\|Q_E\|$ is constant the variation of $\|K_d\|$ will not much affect the corresponding $\Lambda(1,3)$ term.

Now, suppose that for a given system and controller parameters, Λ is positive definite. Let us define the sets

$$\begin{aligned}
\mathcal{R} &= \{(E,\hat{\Delta},\tilde{\delta}) \mid [\|E\| \ \|\hat{\Delta}\| \ \|\tilde{\delta}\|]\Lambda[\|E\| \ \|\hat{\Delta}\| \ \|\tilde{\delta}\|]^T \leq 2\gamma^T[\|E\| \ \|\hat{\Delta}\| \ \|\tilde{\delta}\|]^T\} \cap \Omega_i \\
\mathcal{S} &= \{(E,\hat{\Delta},\tilde{\delta}) \mid V(E,\hat{\Delta},\tilde{\delta}) \leq c_1\} \subset \Omega_i \\
\mathcal{T} &= \{(E,\hat{\Delta},\tilde{\delta}) \mid V(E,\hat{\Delta},\tilde{\delta}) = c_2\} \subset \Omega_i
\end{aligned} \tag{A.37}$$

where $0 < c_2 \leq c_1$ and c_2 is the smallest constant such that $\mathcal{R} \subset \mathcal{T}$. Since the trajectory defined by y_r, $\dot{y}_r$, $\ddot{y}_r$ is bounded, and Λ is positive–definite, $\mathcal{R}$ is uniformly bounded . If the initial state is outside $\mathcal{S} - \mathcal{R}$, where $\dot{V} \leq 0$, it follows that there exists a finite time t_f such that any solution starting from $\mathcal{S} - \mathcal{R}$, at $t > 0$, will enter $\mathcal{T}$ at t_f, and remain in $\mathcal{T}$ thereafter for all $t \geq t_f$. The residual set $\mathcal{T}$ encompasses an ellipsoid in $[\|E\| \ \|\hat{\Delta}\| \ \|\tilde{\delta}\|]$ coordinates with its bounds being $\sqrt{\gamma^T\Lambda^{-1}\gamma/\lambda_{min}(\Lambda)}$ and $\sqrt{\gamma^T\Lambda^{-1}\gamma/\lambda_{max}(\Lambda)}$ which are both of order ϵ. Since $\hat{\Delta} = \epsilon\Delta$, it follows that Δ is of the order of $\frac{1}{\epsilon}$ on this residual set. As discussed earlier, controller parameters should be chosen such that Λ is positive–definite. To this end,

some qualitative robustness measures may be obtained. In particular, making the norms of P_E, $K_\delta(q)$, $K_{\dot{\delta}}(q), P_{\tilde{\delta}}, P_\Delta$ small yields a better margin of robustness.

A.4 Proof of Theorem 5.1

Consider the dynamic equations of the closed–loop system given by (5.13), (5.16) and (5.20) which are repeated here for convenience

$$\dot{s}_{\sigma_i} = (1 + \Delta B^*_{ii}) k_i sat(\gamma_i s_{\sigma_i}) + \sum_{j=1, j\neq i}^{n} \Delta B^*_{ij} k_j sat(\gamma_j s_{\sigma_j}) + \eta^*_i, \quad i = 1, \cdots, n \tag{A.38}$$

$$\dot{E} = A_E E + d_E(E, \Delta, s_\sigma, t) \tag{A.39}$$

$$\dot{\Delta} = A_\Delta(q)\Delta + g_\Delta(E, \Delta, s_\sigma, t) \tag{A.40}$$

Since A_E and $A_\Delta(q)$ are Hurwitz matrices the following Lyapunov equations are satisfied

$$\begin{aligned} A_E^T P_E + P_E A_E &= -Q_E \\ A_\Delta^T(q) P_\Delta(q) + P_\Delta(q) A_\Delta(q) &= -Q_\Delta \end{aligned} \tag{A.41}$$

where P_E, Q_E, $P_\Delta(q)$ and Q_Δ are symmetric positive–definite matrices. Let us choose the positive–definite Lyapunov function candidate

$$V = E^T P_E E + \hat{\Delta}^2 P_\Delta(q)\hat{\Delta} + 0.5 s_\sigma^T s_\sigma \tag{A.42}$$

where $\hat{\Delta} = \epsilon_\Delta \Delta$ with ϵ_Δ being a small positive scaling constant (typically less than one). The need for this scaling factor arises from the stability requirement that E and s_σ converge to small values near zero while Δ remains bounded. Thus, the scaling factor allows us to show that E, s_σ and $\hat{\Delta}$ converge to small values, hence Δ converges to $\hat{\Delta}/\epsilon_\Delta$.

Taking the time derivative of V yields

$$\dot{V} = -E^T Q_E E - \hat{\Delta}^T Q_\Delta \hat{\Delta} + 2d_E^T P_E E + 2\epsilon_\Delta \hat{\Delta} P_\Delta g_\Delta + \hat{\Delta}\dot{P}_\Delta \hat{\Delta} + \dot{s}_\sigma s_\sigma \qquad (A.43)$$

Consider a continuous bounded reference trajectory (at least C^2) and a bounded region Ω_1 containing the origin of (E, Δ, s_σ). Then for all $(E, \Delta, s_\sigma) \in \Omega_1 \subset \mathbf{R^{2m+3n}}$ (with $\|s_\sigma\|_1 < 1$ as described later)

$$\|d_E\| \leq l_1 + l_2\|\Delta\| + l_3\|E\| \qquad (A.44)$$

where, as far as the design parameters are concerned, l_1 is affected by K and the reference trajectory, l_2 is affected by K_δ and $K_{\dot{\delta}}$, and l_3 by K_p and K_d. Note that all the norms in the previous inequality and subsequent discussion are 1–norms. Similarly for all $(E, \Delta, s_\sigma) \in \Omega_2 \subset \mathbf{R^{2m+3n}}$

$$\|g_\Delta\| \leq l_4 + l_5\|\Delta\| + l_6\|E\| \qquad (A.45)$$

with l_4 affected by K and the reference trajectory, and l_6 by K_p and K_d.

A detailed analysis also reveals that for all $(E, \Delta, s_\sigma) \in \Omega_3 \subset R^{2m+3n}$, where Ω_3 is a finite region containing the origin of (E, Δ, s_σ), we have $\|\dot{P}_\Delta(q)\| \leq l_{\Delta_2}$. This can be shown by noting that $P_\Delta(q)$ has a finite growth rate with respect to q (see e.g. [67], Problem 5.21) and the reference trajectory is bounded.

As discussed previously the surface $s_\sigma = 0$ is attractive for $s_\sigma \in R$ and other state variables in a closed set Ω^* defined earlier. Thus for any $s_\sigma \in R$, there is a finite time after which s_σ will be small enough such that $\|s_\sigma\| < 1$ (or $\|s_\sigma\| > \|s_\sigma\|^2$). This time can be made short by increasing β_i's in section 2.

Hence, letting $\Omega_i = \Omega_1 \cap \Omega_2 \cap \Omega_3$ and substituting the previous inequalities in $\dot{V}$ and rearranging the right–hand side of the resulting inequality in terms of $\|E\|$, $\|\Delta\|$ and $\|s_\sigma\|$ will, after some algebraic manipulations, yield

$$\dot{V} \leq -[\|E\| \ \|\hat{\Delta}\| \ \|s_\sigma\|]\Lambda \begin{bmatrix} \|E\| \\ \|\hat{\Delta}\| \\ \|s_\sigma\| \end{bmatrix} + 2\gamma^T \begin{bmatrix} \|E\| \\ \|\hat{\Delta}\| \\ \|s_\sigma\| \end{bmatrix} \qquad \forall (E, \Delta, s_\sigma) \in \Omega_i \qquad (A.46)$$

where

$$\Lambda = \begin{bmatrix} \lambda_e - 2l_3\|P_E\| & \frac{l_2\|P_E\|}{\epsilon_\Delta} + l_6\epsilon_\Delta\|P_\Delta\| & 0 \\ \frac{l_2\|P_E\|}{\epsilon_\Delta} + \epsilon_\Delta l_6\|P_\Delta\| & \lambda_\Delta - l_7 - 2\|P_\Delta\|l_5 & 0 \\ 0 & 0 & \beta_{min} \end{bmatrix},$$

$$\gamma^T = [l_1\|P_E\| \;\; \epsilon_\Delta l_4\|P_\Delta\| \;\; 0], \tag{A.47}$$

where $\beta_{min} = min(\beta_1, \cdots, \beta_n)$ and $\lambda_e = \lambda_{min}(Q_E)$, $\lambda_\Delta = \lambda_{min}(Q_\Delta)$, $\lambda_o = \lambda_{min}(A_{\tilde{\delta}})$.

Now consider the matrix Λ when no uncertainty is present. In such a case it is positive–definite if $\lambda_\Delta > l_7 + 2l_5\|P_\Delta\|$ and $\lambda_e(\lambda_\Delta - l_7 - 2l_5\|P_\Delta\|) > (\frac{l_2\|P_E\|}{\epsilon_\Delta} + l_6\epsilon_\Delta\|P_\Delta\|)^2$. Thus a neighborhood of the case with no uncertainty can be found such that Λ is positive–definite. Let us define the sets

$$\begin{aligned} \mathcal{R} &= \{(E, \hat{\Delta}, s_\sigma) \mid [\|E\| \;\; \|\hat{\Delta}\| \;\; \|s_\sigma\|]\Lambda[\|E\| \;\; \|\hat{\Delta}\| \;\; \|s_\sigma\|]^T \leq 2\gamma^T[\|E\| \;\; \|\hat{\Delta}\| \;\; \|s_\sigma\|]^T\} \cap \Omega_i \\ \mathcal{S} &= \{(E, \hat{\Delta}, s_\sigma \mid \; V(E, \hat{\Delta}, s_\sigma) \leq c_1\} \subset \Omega_i \\ \mathcal{T} &= \{(E, \hat{\Delta}, s_\sigma) \mid \; V(E, \hat{\Delta}, s_\sigma) = c_2\} \subset \Omega_i \end{aligned} \tag{A.48}$$

where $0 < c_2 \leq c_1$ and c_2 is the smallest constant such that $\mathcal{R} \subset \mathcal{T}$. Since the trajectory defined by y_r, $\dot{y}_r$, $\ddot{y}_r$ is bounded, and Λ is positive–definite, $\mathcal{R}$ is uniformly bounded. If the initial state is outside $\mathcal{S} - \mathcal{R}$, where $\dot{V} \leq 0$, it follows that there exists a finite time t_f such that any solution starting from $\mathcal{S} - \mathcal{R}$, at $t > 0$, will enter $\mathcal{T}$ at t_f, and remain in $\mathcal{T}$ thereafter for all $t \geq t_f$. The residual set $\mathcal{T}$ encompasses an ellipsoid in $[\|E\| \;\; \|\hat{\Delta}\| \;\; \|\tilde{\delta}\|]$ coordinates with its bounds being $\sqrt{\gamma^T\Lambda^{-1}\gamma/\lambda_{min}(\Lambda)}$ and $\sqrt{\gamma^T\Lambda^{-1}\gamma/\lambda_{max}(\Lambda)}$ which are both of order ϵ. Since $\hat{\Delta} = \epsilon_\Delta\Delta$, it follows that Δ is of the order of $\frac{1}{\epsilon_\Delta}$ on this residual set. As discussed earlier, controller parameters should be chosen such that Λ is positive–definite. By considering the terms affected by these gains some qualitative robustness measures may be obtained. In particular, making the norms of P_E, $K_\delta(q)$, $K_{\tilde{\delta}}(q)$, $P_{\tilde{\delta}}$, P_Δ small yields a better margin of robustness.

Appendix B

Kinematic Description

The various terms used in the manipulators considered in this paper are illustrated here for a two–link planar manipulator as shown in Figure B.1. Assuming that the deformation of each link is small compared to its length, the length of each deformed link is approximately equal to the length of the line–segment joining the two ends of the link. Axis X_2 is defined to be the tangent line drawn from the tip of the first link. Thus, angles y_1 and y_2 are defined as $y_1 = q_1 + \sum_i \phi_{1i}(l_1)\delta_{1i}/l_1$ and $y_2 = q_2 + \sum_j \phi_{2j}(l_2)\delta_{2j}/l_2$. where ϕ_{1i} and ϕ_{2j} represent the modal shape functions of the links (clamped shape functions have been assumed). The control laws derived in this paper result in small tracking errors for y_1 and y_2 defined above. However, if a Cartesian trajectory is specified, it is convenient to define another output for y_2 as follows: Extending the line AB, let us define y_{2n} as the angle between lines BD and BC. Thus, the *new* y_2 can be written as $y_{2n} = y_2 - y_1 + q_1 + \Psi_1$. The angle Ψ_1 is the slope of the tangent at B and is given by $\Psi_1 = \sum_i \phi'_{1ie}\delta_{1i}$, where ϕ'_{1ie} is the spatial derivative of the i–th shape function at l_1. Thus we have $y_{2n} = q_2 + \sum_j \phi_{2j}(l_2)\delta_{2j}/l_2 + \sum_i (\phi'_{1ie} - \phi_{1i}(l_1)/l_1)\delta_{1i}$ which together with y_1 may be represented in the form given by (2.8).

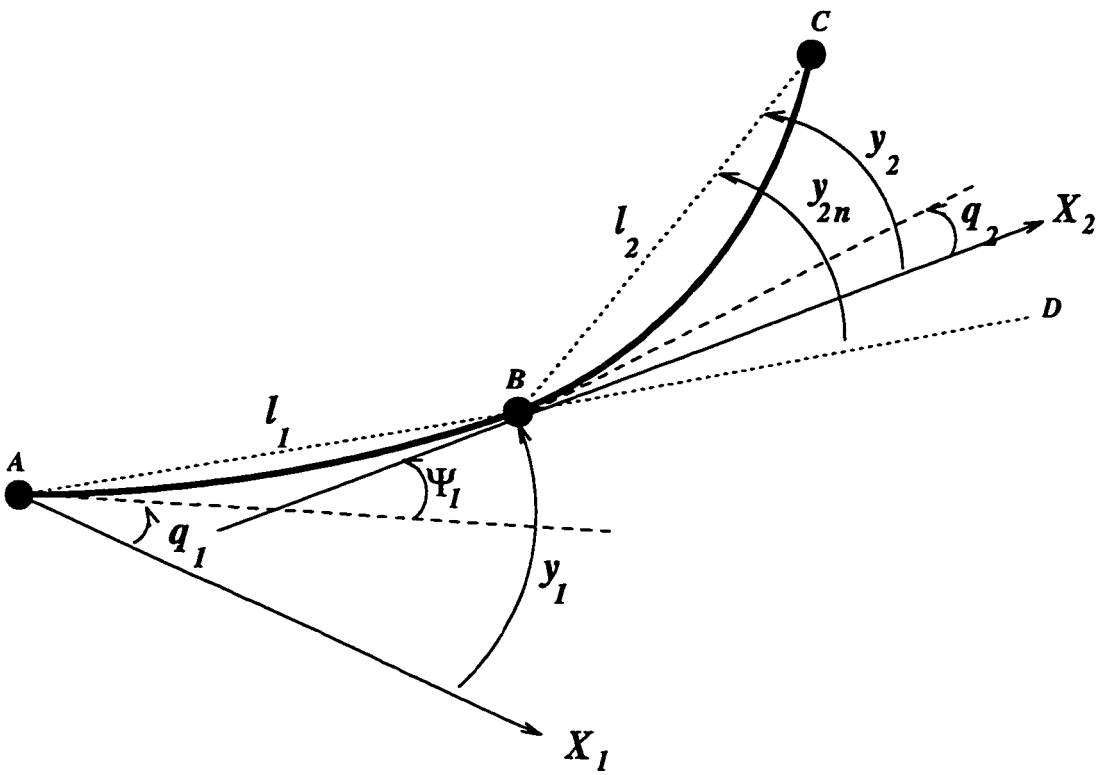

Figure B.1: Kinematic description for a flexible two–link manipulator.

Appendix C

Dynamic Models

C.1 Dynamic Model of the Single–Link Arm

The dynamic model used in designing the controller for the experimental setup is derived based on the assumed modes method with clamped–mass shape functions given by

$$\phi_i(x) = cosh(\lambda_i x/l) - cos(\lambda_i x/l) - \gamma_i(sinh(\lambda_i x/l) - sin(\lambda_i x/l)) \qquad (C.1)$$

where l is the length of the link, x is the position variable along the link and λ_i's are obtained from

$$1 + cosh(\lambda_i)cos(\lambda_i) + \frac{M_p}{m}\lambda_i(sinh(\lambda_i)cos(\lambda_i) - cosh(\lambda_i)sin(\lambda_i)) = 0 \qquad (C.2)$$

where $m = 0.210kg$ is the mass of the link, and $M_p = 0.251kg$ is the payload mass. The first three λ_i's are: 1.2030, 4.0159, and 7.1243.

The mass and stiffness matrices and Coriolis and centrifugal terms obtained by using $MAPLE$ [35] are as follows (see Section 2 for the definition of the terms)

$$M(q,\delta) = \begin{bmatrix} m(\delta) & 0.1863 & 0.0208 \\ 0.1863 & 0.2655 & -7.1518 \times 10^{-5} \\ 0.0208 & -7.1518 \times 10^{-5} & 0.2162 \end{bmatrix}$$

$$K = \begin{bmatrix} 7.5340 & -0.0004 \\ -0.0004 & 755.5287 \end{bmatrix}$$

$$g(q,\dot{q},\delta,\dot{\delta}) = \begin{bmatrix} \dot{q}\dot{\delta}_1(0.2667\delta_1 + 4.2261 \times 10^{-4}\delta_2) + \dot{q}\dot{\delta}_2(0.5308\delta_2 + 4.2261 \times 10^{-4}\delta_1) \\ -0.5\dot{q}^2(0.2667\delta_1 + 4.2261 \times 10^{-4}\delta_2) \\ -0.5\dot{q}^2(0.5308\delta_2 + 4.2261 \times 10^{-4}\delta_1) \end{bmatrix} \tag{C.3}$$

where $m(\delta) = 0.1334 + 0.2654\delta_1^2 + 0.2149\delta_2^2 + 4.2261 \times 10^{-4}\delta_1\delta_2$ and $g(q,\dot{q},\delta,\dot{\delta}) = [g_1^T \; g_2^T]^T$. The natural frequencies obtained from this model can be derived as $\frac{1}{2\pi}\sqrt{eig(H_{220}K)} = 5.2059,\ 21.7267Hz$, which are close to the experimental values 5.5 and 20 Hz.

C.2 Dynamic Model of the Two–Link Manipulator

The dynamic model used in designing the controller for the experimental setup is derived based on the assumed modes method with clamped–mass shape functions given by

$$\phi_i(\sigma) = cosh(\lambda_i\sigma/l_2) - cos(\lambda_i\sigma/l_2) - \gamma_i(sinh(\lambda_i\sigma/l_2) - sin(\lambda_i\sigma/l_2)) \tag{C.4}$$

where l_2 is the length of the flexible link, σ is the position variable along the link, and the λ_i's are obtained from

$$1 + cosh(\lambda_i)cos(\lambda_i) + \frac{M_p}{m}\lambda_i(sinh(\lambda_i)cos(\lambda_i) - cosh(\lambda_i)sin(\lambda_i)) = 0 \tag{C.5}$$

where $m = 0.210kg$ is the mass of the second link , and $M_p = 0.251kg$ is the payload mass. The first three λ_i's are: 1.2030, 4.0159, and 7.1243.

The elements of the mass and stiffness matrices and Coriolis and centrifugal terms obtained using $MAPLE$ [35] for one flexible mode are as follows

$$M(1,1) = m_1 + m_2cos(q_2) + m_3\delta^2$$

$$
\begin{aligned}
M(1,2) &= M(2,1) = m_4 + m_5 cos(q_2) + m_6\delta^2 \\
M(1,3) &= M(3,1) = m_7 + m_8 cos(q_2) \\
M(2,2) &= m_9 + m_{10}\delta^2 \\
M(2,3) &= M(3,2) = m_{11} \\
M(3,3) &= m_{12} \\
f_1(1) + g_1(1) &= \dot{\delta} sin(q_2)[(m_{14} - m_8)\dot{q}_2 + m_{13}\dot{q}_1 - (m_5\dot{q}_2^2 + m_2\dot{q}_2\dot{q}_1)] \\
f_1(2) + g_1(2) &= sin(q_2)[\dot{\delta}(m_8 + m_{14})\dot{q}_1 - (m_5\dot{q}_2^2 + m_2\dot{q}_2\dot{q}_1)] \\
f_2(1) + g_2(1) &= -sin(q_2)[m_8\dot{q}_1 + 0.5m_{13}\dot{q}_1^2 + m_{14}\dot{q}_2\dot{q}_1]
\end{aligned} \tag{C.6}
$$

where $M(i,j)$ represents the (i,j)th element of the mass matrix and $f_i(j) + g_i(j)$ represents element j of the i-th Coriolis and centrifugal terms.

The numerical values of the parameters in (C.6) are given below in appropriate SI units, i.e.,

$$
\begin{gathered}
m_1 = 0.2255, \quad m_2 = 0.1090, \quad m_3 = 0.2654, \quad m_4 = 0.1332, \quad m_5 = 0.5453 \\
m_6 = 0.2654, \quad m_7 = 0.1862, \quad m_8 = 0.0727, \quad m_9 = 0.1332, \quad m_{10} = 0.2654 \\
m_{11} = 0.1862, \quad m_{12} = 0.2654, \quad m_{13} = -0.14542, \quad m_{14} = -0.7271, \quad K = 7.5340.
\end{gathered} \tag{C.7}
$$

C.3 Derivation of the Dynamic Equations

Consider the manipulator sketched in Figure 6.1. Assume that link 1 has cross sectional area $A_1(x_1)$, length l_1, with flexible modes represented by δ_{11}, δ_{12}, $\cdots$, δ_{1m_1}. Similarly, link 2 has cross sectional area $A_2(x_2)$, length l_2, and flexible modes δ_{21}, δ_{22}, $\cdots$, δ_{2m_2}, where $m_1 + m_2 = m$ is the total number of flexible modes. The $X - Y$ frame is the stationary *world* frame, q_1 is the angle of the tangent at $x_1 = 0$ with respect to the X–axis, and q_2 is the angle that x_2–axis makes relative to the slope of the end point of link 1. The modal shape functions are assumed to

be *clamped* at the actuation end (clamped–mass or clamped–free).

Using the above kinematic description the dynamic equations can then be obtained by utilizing the Lagrangian formulation. Towards this end, first the kinetic energy of the system is obtained. Let us denote the description of a point on link 1, written in the $X-Y$ plane, by $r_1(x_1,t)$. Then

$$r_1(x_1,t) = T_1(q_1)\begin{bmatrix} x_1 \\ \sum_{i=1}^{m_1}\phi_{1i}(x_1)\delta_{1i} \end{bmatrix} \tag{C.8}$$

where $T_1(q_1)$ is the rotation matrix of the x_1–y_1 frame, i.e.,

$$T_1(q_1) = \begin{bmatrix} cosq_1 & -sinq_1 \\ sinq_1 & cosq_1 \end{bmatrix} \tag{C.9}$$

Therefore the kinetic energy due to link 1 is given by

$$T_{k_1} = \frac{1}{2}\int_0^{l_1} \rho A_1(x_1)\dot{r}_1^T\dot{r}_1 dx_1 \tag{C.10}$$

Similarly the description of a point corresponding to x_2 on the second link is given in the X–Y frame by

$$r_1(x_1,t) = T_1(q_1)\left(\begin{bmatrix} l_1 \\ y_1(l_1) \end{bmatrix} + T_2\begin{bmatrix} x_2 \\ y_2 \end{bmatrix}\right) \tag{C.11}$$

where

$$\begin{aligned} y(l_1) &= \sum_{i=1}^{m_1}\phi_{1i}(l_1)\delta_{1i} \\ T_2 &= \begin{bmatrix} cos(q_2+\sum_{i=1}^{m_1}\phi'_{1ie}\delta_{1i}) & -sin(q_2+\sum_{i=1}^{m_1}\phi'_{1ie}\delta_{1i}) \\ sin(q_2+\sum_{i=1}^{m_1}\phi'_{1ie}\delta_{1i}) & cos(q_2+\sum_{i=1}^{m_1}\phi'_{1ie}\delta_{1i}) \end{bmatrix} \\ \phi'_{1ie} &:= \frac{d}{dx_1}(\phi_{1i}(x_1))\mid_{x_1=l_1} \end{aligned} \tag{C.12}$$

Hence the kinetic energy due to the second link is

$$T_{k_2} = \frac{1}{2}\int_0^{l_2} \rho A_2(x_2)\dot{r}_2^T\dot{r}_2 dx_2 \tag{C.13}$$

The hub kinetic energy is given by

$$T_h = \frac{1}{2} J_h \dot{q}_h^2 \tag{C.14}$$

where

$$q_h = q_1 + \sum_{i=1}^{m_1} \phi'_{1i}(0)\delta_{1i} \tag{C.15}$$

Since $\phi'_{1i}(0) = 0$ for clamped mode shapes, we have

$$T_h = \frac{1}{2} J_h \dot{q}_1^2 \tag{C.16}$$

The kinetic energy due to M_1 and J_1, which denote the mass and mass moment of inertia of the case and stator of the second motor, is given by

$$T_{k_{mot}} = \frac{1}{2} M_1 \dot{r}_1^T \dot{r}_1 \mid_{x_1 = l_1} + \frac{1}{2} J_1 (\dot{q}_1 + \sum_{i=1}^{m_1} \phi'_{1ie} \dot{\delta}_{1i})^2 \tag{C.17}$$

And finally the payload kinetic energy is

$$T_{k_p} = \frac{1}{2} M_2 \dot{r}_2^T r_2 \mid_{l_2} + \frac{1}{2} J_2 (\dot{q}_1 + \dot{q}_2 + \sum_{i=1}^{m_1} \phi'_{1ie} \dot{\delta}_{1i} + \sum_{i=1}^{m_2} \phi'_{2ie} \dot{\delta}_{2i})^2 \tag{C.18}$$

This the total kinetic energy is obtained as

$$T_k = T_{k_1} + T_{k_2} + T_h + T_{k_{mot}} + T_{k_p} \tag{C.19}$$

The elastic potential energy is obtained from

$$V_e = \frac{1}{2} \sum_{i=1}^{m_1} \sum_{l=1}^{m_1} \delta_{1k} \delta_{1l} k_{1kl} + \frac{1}{2} \sum_{k=1}^{m_2} \sum_{l=1}^{m_2} \delta_{2k} \delta_{2l} k_{2kl} \tag{C.20}$$

which can be written in the matrix form $V_e = \frac{1}{2} \delta^T K \delta$ and

$$\begin{aligned} k_{1kl} &= \int_0^{l_1} EI_{z1}(x_1) \frac{d^2\phi_{1k}(x_1)}{dx_1^2} \frac{d^2\phi_{1l}(x_1)}{dx_1^2} dx_1 \\ k_{2kl} &= \int_0^{l_2} EI_{z2}(x_2) \frac{d^2\phi_{2k}(x_2)}{dx_2^2} \frac{d^2\phi_{2l}(x_2)}{dx_2^2} dx_2 \end{aligned} \tag{C.21}$$

where E is the modulus of elasticity of the material and $I_{z1}(x_1)$, $I_{z2}(x_2)$ are the area moments of inertia about the axis of rotation z_1, z_2 at x_1 and x_2. Note that for a

uniform manipulator the cross product terms in (C.21) are zero if orthogonal shape functions (e.g., clamped–free) are used. If gravity is present, the potential energy due to gravity can also be added to V_e. However, we derive the dynamic equations in the absence of gravity. Denoting the degrees of freedom by

$$z^T = [q_1\ q_2\ \delta_{11}\ \delta_{12}\ \cdots\ \delta_{1m_1}\ \delta_{21}\ \delta_{22}\ \cdots\ \delta_{2m_2}] := [q^T\ \delta^T] \tag{C.22}$$

the Lagrangian equation for the system is given by

$$L = T_k - V_e = \frac{1}{2}(\dot{z}^T M \dot{z} - z^T K z) \tag{C.23}$$

from which the system dynamics can be obtained using

$$\frac{d}{dt}\frac{\partial L}{\partial \dot{z}} - \frac{\partial L}{\partial z} = \tau_g \tag{C.24}$$

where τ_g is the generalized vector of torques which, for the case of clamped mode shapes is given by

$$\tau_g = \begin{bmatrix} I_{2\times 2} \\ 0_{2\times 2} \end{bmatrix} \tau := Q\tau \tag{C.25}$$

where τ is the actual torques at the joints.

The mass matrix of the manipulator can thus be obtained by writing the kinetic energy given by (C.20) and putting it in the form $\frac{1}{2}\dot{z}^T M(q,\delta)\dot{z}$. Then, using the Lagrangian (C.24), it follows that

$$M(q,\delta)\ddot{z} + f(z,\dot{z}) + K_a z = Q\tau \tag{C.26}$$

where the i–th element of $f(z,\dot{z})$ is

$$f_i(z,\dot{z}) = e_i^T \sum_{j=1}^{m+2} \dot{z}_j \frac{\partial M}{\partial z_j}\dot{z} - \frac{1}{2}\dot{z}^T \frac{\partial M}{\partial z_i}\dot{z},\quad i = 1,\ \cdots,\ m+2 \tag{C.27}$$

with e_i the unity vector [1], $f(z,\dot{z})$ containing the centrifugal and Coriolis terms, and K_a is given by

$$K_a = \begin{bmatrix} 0_{2\times 2} & 0_{2\times m} \\ 0_{m\times 2} & K_{m\times m} \end{bmatrix} \tag{C.28}$$

[1] A unity vector e_i is a vector with all its elements zero except for the i–th element; which is 1.

The above steps were coded to obtain the dynamic equations using the symbolic manipulation software *MAPLE* [35].

Bibliography

[1] G. Hastings and W. J. Book, "Experiments in the Optimal Control of a Flexible Link Manipulator," *American Control Conference*, pp. 728–729, Boston, 1985.

[2] R. H. Cannon and E. Schmitz, "Initial Experiments on the End–Point control of a Flexible One–Link Robot," *The International Journal of Robotics Research*, Vol. 3, No. 3, pp. 62–75, 1984.

[3] G. Hastings and W. J. Book, "A Linear Dynamic Model for Flexible Robotic Manipulators," *IEEE Control Systems Magazine*," pp. 61–64, 1987.

[4] F. Bellezza, L. Lanari and G. Ulivi, "Exact Modeling of the Flexible Slewing Link," *IEEE International Conference on Robotics and Automation*, pp. 734–739, 1990.

[5] S. Cetinkunt and W. L. Yu, "Closed Loop Behavior of a Feedback–Controlled Flexible Arm: A Comparative Study," *International Journal of Robotics Research*, Vol. 10, No. 3, pp. 263–275, 1991.

[6] E. Bayo, "A Finite–Element Approach to Control the End–Point Motion of a Single–Link Flexible Robot," *Journal of Robotic Systems*, Vol. 4, No. 1, pp. 63–75, 1987.

[7] P. B. Usoro, R. Nadira and S. S. Mahil, "A Finite Element / Lagrange Approach to Modeling Lightweight Flexible Manipulators," *The International Journal of Robotics Research*, Vol. 3, No. 3, pp. 87–101, 1984.

[8] B. Siciliano and W. J. Book, "A Singular Perturbation Approach to Control of Lightweight Flexible Manipulators," *International Journal of Robotics Research*, Vol. 7, No. 4, pp. 79–90, 1989.

[9] A. De Luca A. and B. Siciliano, "Explicit Dynamic Modeling of a Planar Two–Link Flexible Manipulator," *29th IEEE Conference on Decision and Control*, Honolulu, Hawaii, December 1990.

[10] M. Benati and A. Morro, "Dynamics of Chain of Flexible Links," *ASME Journal of Dynamic Systems, Measurement, and Control*, Vol. 110, pp. 410–415, 1988.

[11] H. P. Pota and M. Vidyasagar, "Passivity of Flexible Beam Transfer Functions with Modified Outputs," *IEEE International Conference on Robotics and Automation*, Sacramento, pp. 2826–2831, April 1991.

[12] D. Wang and M. Vidyasagar, "Passive Control of a Flexible Link," *International Journal of Robotics Research*,Vol. 11, No. 6, pp. 572–578, Dec. 1992.

[13] T. Yoshikawa, H. Murakami and K. Hosoda, "Modeling and Control of a 3 D.O.F. Manipulator with two Flexible Links," *29th IEEE Conference on Decision and Control*, Honolulu, Hawaii, pp. 2532–2537, December 1990.

[14] A. Deluca, L. Lanari, P. Lucibello, S. Panzieri and G. Ulivi, "Control Experiments on a Two Link Robot with a Flexible Forearm," *29th IEEE Conference on Decision and Control*, Honolulu, Hawaii, pp. 520–527 December 1990.

[15] L. Meirovitch, "Elements of Vibration Analysis," *McGraw–Hill*, New– York, 1975.

[16] Y. Aoustin and C. Chevallereau, "The Singular Perturbation Control of a Two–Flexible–Link Robot," *IEEE International Conference on Robotics and Automation*, Atlanta, Georgia, pp. 737–742, May 1993.

[17] B. Siciliano, V. R. J. Prasad and A. J. Calise, "Design of a Composite Controller for a Two–Link Flexible Manipulator," *International Symposium on Intelligent Robotics*, Bangalore, India, pp. 126–137, 1991.

[18] R. M. Hirschorn, "Invertibility of Nonlinear Control Systems," *SIAM Journal of Control and Optimization*, Vol. 17, No. 2, pp. 282–297, 1979.

[19] C. I. Byrnes and A. Isidori, "Global Feedback Stabilization of Nonlinear Systems," *24th IEEE Conference on Decision and Control*, pp. 1031–1037, 1985.

[20] L. Russel and F. W. Wang, "Minimum–Weight Robot Arm for a Specified Fundamental Frequency," *IEEE International Conference on Robotics and Automation*, pp. 490-495, Atlanta GA, 1993.

[21] H. Asada, J. H. Park and S. Rai, "A Control–Configured Flexible Arm: Integrated Structure–Control Design," *IEEE International Conference on Robotics and Automation*, Sacramento CA, 1991.

[22] J. H. Park and H. Asada, "Integrated Structure / Control Design of a Two–Link Nonrigid Robot Arm for High Speed Positioning," *IEEE International Conference on Robotics and Automation*, Nice, France, 1992.

[23] A. De Luca and L. Lanari, "Achieving Minimum Phase Behavior in a One–Link Flexible Arm," *International Symposium on Intelligent Robotics*, Bangalore, India, 1991.

[24] D. S. Kwon and W. J. Book, "An Inverse Dynamic Method Yielding Flexible Manipulator State Trajectories," *American Control Conference*, pp. 186–193, 1990.

[25] K. L. Hillsley and S. Yurkovich, "Vibration Control of a Two–Link Flexible Robot Arm," *International Conference on Robotics and Automation*, Sacramento Ca, pp. 2121–2126, 1991.

[26] A. Tzes and S. Yurkovich, "An Adaptive Input Shaping Control Scheme for Vibration Suppression in Slewing Flexible Structures," *IEEE Transactions on Control Systems Technology*, Vol.1, No. 2, pp. 114–121, June 1993.

[27] F. Khorrami, S. Jain and A. Tzes, "Experiments on Rigid Body Based Controllers with Input Preshaping for a Two Link flexible Manipulator," *American Control Conference*, pp. 2957–2961, 1992.

[28] S. E. Burke and E. Hubbard, "Distributed Actuator Control Design for Flexible Beams," *Automatica*, Vol. 24, No. 5, pp. 619–627, 1988.

[29] W. J. Book, "Recursive Lagrangian Dynamics of Flexible Manipulator Arms," *The International Journal of Robotics Research*, Vol. 3, No. 3, pp. 87–101, Fall 1984.

[30] K. Khorasani, " A Robust Adaptive Control Design for a Class of Dynamical Systems using Corrected Models," *IEEE Transactions on Automatic Control*, Vol.39, No. 6, pp. 1726–1732, 1994.

[31] A. Isidori, "Nonlinear Control Systems," *Springer–Verlag*, New York, 1995.

[32] M. Spong and M. Vidyasagar, "Robot Dynamics and Control," *McGraw–Hill*, 1989.

[33] W. T. Thomson, "Theory of Vibrations with Applications," *Prentice–Hall*, Englewood Cliffs, N. J., 1988.

[34] S. Tosunoglu, S. H. Lin and D. Tesar, "Accessibility and Controllability of Flexible Robotic Manipulators," *ASME Journal of Dynamic Systems, Measurement, and Control*, Vol. 114, pp. 50–58, 1992.

[35] D. Redfern, "The Maple Handbook," *Springer-Verlag*, New York, 1993.

[36] D. Wang and M. Vidyasagar, "Transfer Functions for a Single Flexible Link," *IEEE International Conference on Robotics and Automation*, pp. 1042–1047, 1989.

[37] A. De Luca and L. Lanari, "Achieving Minimum–Phase Behavior in a One–Link Flexible Arm," *International Symposium on Intelligent Robotics*, Bangalore, India, pp. 224–235, 1991.

[38] S. K. Madhavan and S. N. Singh, "Inverse Trajectory Control and Zero–Dynamics Sensitivity of an Elastic Manipulator," *International Journal of Robotics and Automation*, Vol. 6, No. 4, pp. 179–191, 1991.

[39] V.G. Moudgal, K. Passino and S. Yurkovich, "Rule–Based Control for a Flexible–Link Robot," *IEEE Transactions on Control Systems Technology*, Vol. 2, No. 4, pp. 392–405, Dec. 1994.

[40] E. Bayo and H. Moulin, "An Efficient Computation of the Inverse Dynamics of Flexible Manipulators in the Time Domain," *IEEE International Conference on Robotics and Automation*, pp. 710–715, 1989.

[41] R.V. Patel and P. Misra, "Transmission Zero Assignment in Linear Multivariable Systems, Part II: The General Case," *American Control Conference*, pp. 644–648, Chicago, IL, 1992.

[42] K. Hashtrudi–Zaad and K. Khorasani, "Control of Nonminimum Phase Singularly Perturbed Systems with Applications to Flexible–Link Manipulators," *Workshop on Advances in Control and its Applications*, eds. H.K. Khalil, J.H. Chow and P.A. Ioannou, Lecture Notes in Control and Information Sciences 208, Springer–Verlag, New York, pp. 234–265, 1995.

[43] K. Hashtrudi–Zaad and K. Khorasani, "Control of Nonminimum Phase Singularly Perturbed Systems with Applications to Flexible Link Manipulators," *International Journal of Control*, Vol. 63, No. 4, pp. 679–701, March 1996.

[44] J. H. Chow and P. V. Kokotović, "Two Time Scale Feedback Design of a Class of Nonlinear Systems," *IEEE Transactions on Automatic Control*, Vol. AC–23, pp. 438–443, 1978.

[45] M. W. Spong, K. Khorasani and P. V. Kokotović, "An Integral Manifold Approach to the Feedback Control of Flexible Joint Robots," *IEEE Journal of Robotics and Automation*, Vol. 3, pp. 291–300, 1987.

[46] K. Khorasani and M. W. Spong, "Invariant Manifolds and their Application to Robot Manipulators with Flexible Joints," *IEEE International Conference on Robotics and Automation*, pp. 978–983, 1985.

[47] H. K. Khalil, "On the Robustness of Output Feedback Control Methods to Modeling Errors," *IEEE Transactions on Automatic Control*, Vol. AC–26, pp. 524–526, 1981.

[48] F. L. Lewis and M. Vandegrift, "Flexible Robot Arm Control by a Feedback Linearization Singular Perturbation Approach," *IEEE International Conference on Robotics and Automation*, pp. 729–736, 1993.

[49] B. Sicilliano, J. V. R. Prasad and A. J. Calise, "Output Feedback Two–Time Scale Control of Multi–Link Flexible Arms," *ASME J. Dyn. Sys., Meas., Contr.*, Vol. 114, pp. 70–77, 1992.

[50] Y. Aoustin, C. Chevallereau, A. Glumineau, and C. H. Moog, "Experimental Results for the End–Effector Control of a Single Flexible Robotic Arm," *IEEE Transactions on Control Systems Technology*, Vol. 2, pp. 371–381, 1994.

[51] F. Khorrami, "A Two–Stage Controller for Vibration Suppression of Flexible–Link Manipulators," *29th IEEE Conference on Decision and Control*, pp. 2560–2565, 1990.

[52] B. Siciliano, W. J. Book and G. De Maria, "An Integral Manifold Approach to Control of a One–Link Flexible arm," *25th IEEE Conference on Decision and Control*, pp. 1131–1134, 1986.

[53] K. Khorasani," Adaptive Control of Flexible–Joint Robots," *IEEE Transactions on Robotics and Automation*, Vol. 8, No. 2, pp. 250–267, 1992.

[54] H. Geniele, R. V. Patel and K. Khorasani, "Control of a Flexible–Link Manipulator," *IEEE International Conference on Robotics and Automation*, Nagoya, Japan, pp. 1217–1222, 1995; to appear in IEEE Transactions on Control Systems Technology, 1997.

[55] J. Caruson, S. B. Keir and D'Eleuterio, "Experiments in End–Effector Tracking Control for Structurally Flexible Space Manipulators," *IEEE Transactions on Robotics and Automation*, Vol. 9, No. 5, pp. 553–560, October 1993.

[56] D. Wang and M. Vidyasagar, "Feedback Linearizability of Multi–Link Manipulators with One Flexible Link," *28th IEEE Conference on Decision and Control*, Tampa, Florida, 1989.

[57] D. N. Schoenwald and and Ü. Özgüner, "On combining Slewing and Vibration Control in Flexible Manipulators via Singular Perturbations," *29th IEEE Conference on Decision and Control*, Honolulu, Hawaii, 1990.

[58] S. P. Nicosia, P. Tomei and A. Tornambe, "Approximate Asymptotic Observers for a Class of Nonlinear Systems," *Systems and Control Letters*, Vol. 12, pp. 43–51, 1989.

[59] S. P. Nicosia and P. Tomei, "Observer–Based Control Laws for Robotic Manipulators," *International Symposium on Intelligent Robotics*, Bangalore, India, pp. 313–321, 1991.

[60] C. Canudas de Wit and J-J. E. Slotine, "Sliding Observers for Robot Manipulators," *Automatica*, Vol. 27, pp. 859–864, 1991.

[61] J-J. E. Slotine, J. K. Hedrick and E. A. Misawa, "On Sliding Observers for Nonlinear Systems," *ASME J. Dyn. Syst., Meas. and Contr.*, Vol 109, pp. 245–252, 1987.

[62] E. A. Misawa and J. K. Hedrick, "Nonlinear Observers: A State–of–the–Art Survey," *ASME J. of Dynamic Systems, Meas. and Contr.*, Vol. 111, pp. 344–352, 1989.

[63] S. Panzieri and G. Ulivi, "Design and Implementation of a State Observer for a Flexible Robot," *IEEE International Conference on Robotics and Automation*, Atlanta, GA, pp. 204–209, 1993.

[64] D. C. Nemir, A.J. Koivo and R.L. Kashyap, "Pseudo–Links and Self–Tuning Control of a Nonrigid Link Mechanism," *IEEE Transactions on Systems, Man, Cybernetics*, Vol. 18, No. 1, pp. 40–48, Feb. 1988.

[65] R. V. Patel and M. Toda, "Qualitative Measures of Robustness for Multi-variable Systems," *Joint Automatic Control Conference*, San Francisco, CA, No. TP8-A, 1980.

[66] J-J.E. Slotine and W. Li, "Applied Nonlinear Control," *Prentice Hall*, Englewood Cliffs, NJ, 1991.

[67] H. K. Khalil, "Nonlinear Systems," Macmillan, New York, 1992.

[68] J. Descusse and C. Moog, "Decoupling with Dynamic Compensation for Strong Invertibel Affine Nonlinear Systems," *International Journal of Control*, Vol. 42, No. 6, pp. 1387–1398, 1985.

[69] M. Moallem, R. V. Patel and K. Khorasani, "An Inverse Dynamics Control Strategy for Tip Position Tracking of Flexible Multi–Link Manipulators," *International Federation of Automatic Control 13th World Congress*, San Francisco, CA, Vol. A, pp. 85–90, 1996.

[70] M. Moallem, K. Khorasani and R. V. Patel, "Tip Position Tracking of Flexible Multi–Link Manipulators: An Integral Manifold Approach," *IEEE International Conference on Robotics and Automation*, Minneapolis, MN, pp. 2432–2437, 1996; to appear in IEEE Transactions on Robotics and Automation, 1997.

[71] M. Moallem, K. Khorasani and R. V. Patel, "Optimum Structure Design for Flexible–Link Manipulators," *IEEE International Conference on Robotics and Automation*, Minneapolis, MN, pp. 798–803, 1996.

[72] D. N. Godbole and S. S. Sastry, "Approximate Decoupling and Asymptotic tracking for MIMO Systems," *IEEE Transactions on Automatic Control*, Vol. 40, No. 3, pp. 441-450, March 1995.

[73] D. B. Stewart, D. E. Schmitz and P. K. Khosla, *Chimera 3.2: The Real–Time Operating System for Reconfigurable Sensor–Based Control Systems.* The Robotics Institute, Dept of Electrical and Computer Engineering, Carnegie Mellon University, 1993.

[74] W. H. Press, B. P. Flannery, S. A. Teukolsky and W. T. Vetterling, *Numerical Recipes in C: The Art of Scientific Computing.* Cambridge University Press, New York, 1995.

[75] V. I. Utkin, "Variable Structure Systems with Sliding Modes," *IEEE Transactions on Automatic Control*, Vol. AC–22, No. 2, pp. 212–222, 1977.

[76] R. A. DeCarlo, S. H. Zak and G. P. Mathews, "Variable Structure Control of Nonlinear Multivariable Systems: A Tutorial," *Proceedings of the IEEE*, Vol. 76, No. 3, 1988.

[77] J. J. Slotine and S. S. Sastry, "Tracking Control of Non–Linear Systems Using Sliding Surfaces, with Application to Robot Manipulators," *International Journal of Control*, Vol. 38, No. 2, pp. 465–492, 1983.

[78] M. Moallem, R. V. Patel and K. Khorasani, "An Observer–Based Inverse Dynamics Control Strategy for Flexible Multi–Link Manipulators," *35th IEEE Conference on Decision and Control, Kobe, Japan*, 1996.

[79] A. De Luca, P. Lucibello and G. Ulivi, "Inversion Techniques for Trajectory Control of Flexible Robot Arms," *Journal of Robotic Systems*, Vol. 6, No. 4, pp. 325–344, 1989.

[80] J.–J. E. Slotine and J. A. Coetsee, "Adaptive Sliding Controller Synthesis for Non–Linear Systems," *International Journal of Control*, Vol. 43, No. 6, pp. 1631–1651, 1986.

[81] P. V. Kokotović, H. K. Khalil, and J. O'Reilly, "Singular Perturbation Methods in Control: Analysis and Design," *Academic Press*, 1986.

[82] F-Y. W. Wang and J. L. Russell, "Optimum Shape Construction of Flexible Manipulators with Total Weight Constraint," *IEEE Transactions on Systems, Man, and Cybernetics*, Vol. 25, No. 4, 1995.

[83] C. de Boor, "Spline Toolbox for use with MATLAB," *The Math Works, Inc., Natick, MA*, 1990.

[84] C. de Boor, "A Practical Guide to Splines," *Applied Mathematical Sciences*, Vol. 27, Springer–Verlag, New York, 1978.

[85] A. Grace, "Optimization Toolbox User's Guide," *The Math Works, Inc.*, Natick, MA, 1990.

[86] W. J. Book and M. Majette, "Controller Design for Flexible, Distributed Parameter Mechanical Arms via State Space and Frequency Domain Techniques," *Journal of Dynamic Systems, Measurement, and Control*, Vol. 105, pp. 245–254, 1983.

[87] J. Hauser and R. M. Murray, "Nonlinear Controllers for Non–Integrable Systems: The Acrobot Example," *American Control Conference*, pp. 669–671, 1990.

[88] J. Hauser, S. Sastry and G. Meyer, "Nonlinear Control Design for Slightly Nonminimum–Phase Systems: Application to V/STOL Aircraft," *Automatica*, 28(4), pp. 665–679, 1992.

[89] S. A. Bortoff and M. W. Spong, "Pseudolinearization of the Acrobot using Spline Functions," *31st IEEE Conference on Decision and Control*, Tucson, AZ, pp. 593-598, 1992, pp. 593-598.

[90] K. Hashtrudi–Zaad and K. Khorasani, "An Integral Manifold Approach to Tracking Control for a Class of Non–minimum Phase Linear Systems by Using Output Feedback," in press, *Automatica*, 1996.

[91] M. Moallem, R. V. Patel and K. Khorasani, " Experimental Results for Nonlinear Decoupling Control of Flexible Multi–Link Manipulators," *IEEE International Conference on Robotics and Automation*, Albuquerqe, NM, 1997.

[92] M. Moallem, K. Khorasani and R.V. Patel, "Inverse Dynamics Sliding Control of Flexible Multi–Link Manipulators," *American Control Conference*, Albuquerqe, NM, 1997.

IMAGE EVALUATION
TEST TARGET (QA-3)

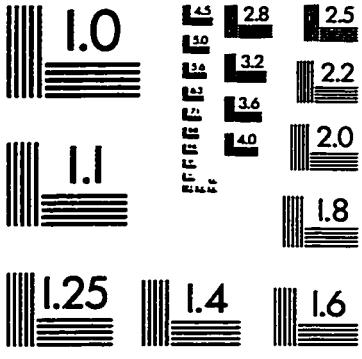

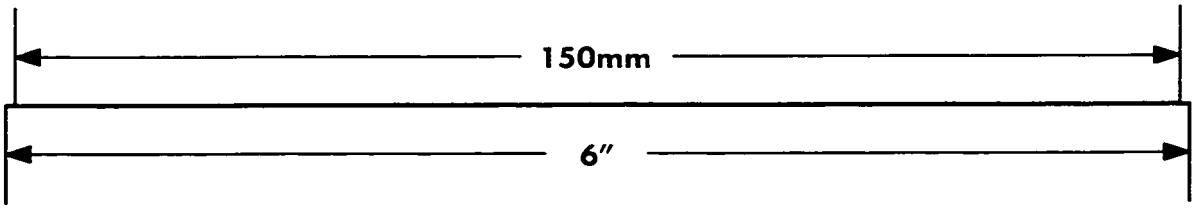

APPLIED IMAGE, Inc
1653 East Main Street
Rochester, NY 14609 USA
Phone: 716/482-0300
Fax: 716/288-5989